The General Circulation of the Tropical Atmosphere and Climate Changes

Thesis by

Timothy Moore Merlis

In Partial Fulfillment of the Requirements

for the Degree of

Doctor of Philosophy

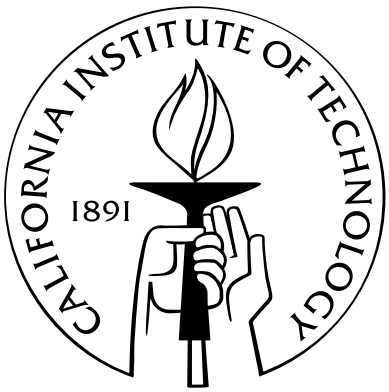

California Institute of Technology

Pasadena, California

2012

(Defended July 7, 2011)

Acknowledgments

I thank everyone who has helped! First, Shanon has been wonderful throughout our time together—you made graduate school a fun journey to take. My family provided the foundation for this endeavor: many talented people have not made it as far as I have because they lacked this support. Thank you Mom, Dad, Alex, Ben, Polly, Hugh, and everyone else, including the southern New Jersey contingent.

Working with Tapio Schneider and the members of his group has been an incredible (and efficient) educational experience. It is hard to overstate Tapio's influence on my scientific development, for which I am deeply appreciative. The members of Tapio's group who have helped in many ways include Paul O'Gorman, Xavier Levine, Simona Bordoni, Yohai Kaspi, Ian Eisenman, Gretchen Keppel-Aleks, Sonja Graves, Rob Korty, and Junjun Liu. There are many other officemates and ESE students who enhanced my Caltech experience.

My thesis committee members have given me their time and careful consideration of my work. Thank you Andy Ingersoll, Andy Thompson, Jess Adkins, Simona Bordoni, and Tapio Schneider. The Caltech administrators who have helped make the sailing smooth include Nora Oshima, Dian Buchness, and Liz Miura Boyd.

I thank Isaac Held for scientific discussions over the course of my time as a graduate student.

I received excellent mentoring as an undergraduate: Alexey Kaplan, Samar Khatiwala, David Keyes, Lorenzo Polvani, and Adam Sobel made sure that I was well-prepared to pursue a PhD.

I could not have worked as rapidly were it not for public software and code shared by other researchers. In particular, the Geophysical Fluid Dynamics Laboratory

spectral dyanmical core and the modifications to it made by Tapio Schneider, Chris Walker, Dargan Frierson, and Paul O'Gorman were essential to this thesis.

I gratefully acknowledge the financial support provided by a National Defense Science and Engineering Graduate Fellowship and a National Science Foundation Graduate Research Fellowship.

Chapter 2,Appendix A, and Appendix B are joint work with Tapio Schneider. Chapters 3 and 4 are joint work with Tapio Schneider, Simona Bordoni, and Ian Eisenman.

Abstract

I examine the general circulation of the tropical atmosphere and climate changes. First, the response of the zonal surface temperature gradients and zonally asymmetric tropical overturning circulations (Walker circulations) to substantial changes in the longwave optical depth of the atmosphere in an idealized general circulation model (GCM) is compared with scaling theories. Second, the response of the hydrological cycle and monsoonal Hadley circulations to changes in top-of-atmosphere insolation associated with orbital precession is examined in an idealized GCM.

Zonal surface temperature gradients and Walker circulations are examined over a wide range of climates simulated by varying the optical thickness in an idealized atmospheric GCM with a climate-invariant zonally asymmetric ocean energy flux. The tropical zonal surface temperature gradient and Walker circulation generally decrease as the climate warms in the GCM simulations. A scaling relationship based on a two-term balance in the surface energy budget accounts for the changes in the zonally asymmetric component of the GCM-simulated surface temperature gradients. A scaling estimate for the Walker circulation based on differential changes (precipitation rates and saturation specific humidity) in the hydrological cycle accounts for the GCM simulations provided locally averaged quantities are used in the estimate.

The results of atmospheric GCM simulations with varied top-of-atmosphere insolation are analyzed to constrain orbitally forced changes in the tropical atmospheric circulations and precipitation. When the perihelion is varied between solstices, there is more annual-mean precipitation in the hemisphere in which perihelion occurs during the summer solstice. In aquaplanet simulations, this is primarily associated with thermodynamic changes: there is a correlation between the seasonal cycle of the per-

turbed water vapor and the seasonal cycle of the Hadley circulation convergence. The monsoonal Hadley circulation does not respond to insolation gradients in a simple manner, as the atmosphere's energy stratification changes. An idealized continent that has a simple treatment of land surface hydrology and inhomogeneous heat capacity allows an assessment of how land–sea contrasts can mediate the response to orbital precession. In these simulations, the response of precipitation to orbital precession depends on changes in the atmospheric circulation, which strengthens when perihelion occurs in the summer of the hemisphere with the land region. The changes in atmospheric circulation are related to changes in both the top-of-atmosphere energy balance and the thermodynamic properties of the surface.

Contents

List of Figures

List of Tables

Chapter 1

Introduction

1.1 Motivation

Earth's climate is the turbulent equilibrium that emerges from the fluid flows of the atmosphere and ocean. While the equations of motion for these fluids are known, computational limitations necessitate the parameterization of unresolved processes when the equations are integrated in discrete form. A difficulty in making climate predictions with these general circulation models (GCMs) is that they cannot be tested on the timescale of interest ($\gtrsim 100$ years). As such, it is of paramount importance to develop physical understanding of the processes that constrain climate changes. The approach pursued here is to build mechanistic theories by examining the response of GCMs to a systematic range of climate forcings.

The utility of developing a physically based understanding of climate change can be illustrated by considering the situation when there is uncertainty in climate observations. For example, the sign of the changes in the east–west surface temperature contrast across the tropical Pacific in the twentieth century is unclear (Vecchi et al. 2008). In this case, observations cannot be used to distinguish between arguments that propose increasing or decreasing temperature contrast in response to increasing greenhouse gases (Clement et al. 1996; Knutson and Manabe 1995, respectively). An adequate mechanistic theory could resolve competing arguments, and aspects of this example are addressed in more detail in Chapter 2. Even when observations are less ambiguous, independent estimates of climate changes can be mutually consistent

with current observations while disagreeing for future projections. Here too, physical understanding is helpful in distinguishing disparate estimates.

The goal of this thesis is to provide physically based constraints on the general circulation of the tropical atmosphere and climate changes. Before describing the specific climate changes that I address in detail, the basic aspects of the tropical climate on which this thesis builds are reviewed.

1.2 Basic aspects of tropical climate

1.2.1 Surface energy balance[1]

The dominant balance in the tropical surface energy budget over oceans is between heating by shortwave radiation and cooling by evaporation (e.g., Trenberth et al. 2009). This balance occurs generally on sufficiently warm Earth-like aquaplanets (Pierrehumbert 2002; O'Gorman and Schneider 2008b). The dominance of evaporation in the surface energy budget in sufficiently warm climates can be understood by considering how the Bowen ratio, the ratio of sensible to latent surface fluxes, depends on temperature. For surface fluxes given by bulk aerodynamic formulas, the Bowen ratio B depends on the surface temperature T_s, the near-surface air temperature T_a, and the near-surface relative humidity $\mathcal{H}$,

$$B \sim \frac{c_p(T_s - T_a)}{L\big(q_s(T_s) - \mathcal{H}q_s(T_a)\big)}, \tag{1.1}$$

where q_s is the saturation specific humidity, c_p is the specific heat of air at constant pressure, and L is the latent heat of vaporization. Figure 1.1 shows the Bowen ratio as a function of surface temperature, assuming a fixed surface–air temperature difference and fixed relative humidity. We have fixed these to values that are representative of Earth's atmosphere, but the surface–air temperature difference and relative humidity can vary as well. For surface temperatures greater than $\sim$290 K, latent heat fluxes are a factor of $\gtrsim$4 larger than sensible heat fluxes, as at Earth's surface (Trenberth et al.

[1]This section is a near-verbatim reproduction of section 3.2 of Merlis and Schneider (2010).

2009). Similar arguments apply for net longwave radiative fluxes at the surface, which become small as the longwave optical thickness of the atmosphere and with it surface temperatures increase; see Pierrehumbert (2010) for a more complete discussion of the surface energy budget.

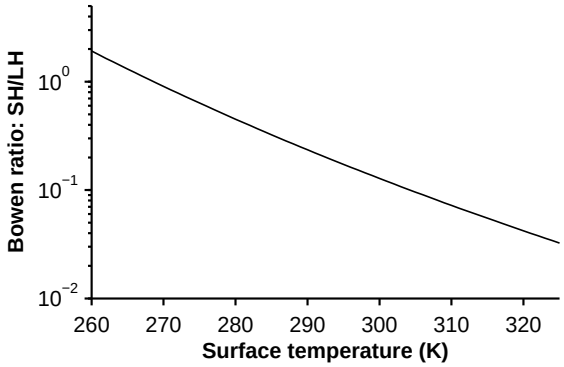

Figure 1.1. Bowen ratio vs. surface temperature assuming a 3-K surface–air temperature difference, 70% relative humidity, and surface and surface air pressure of 10^5 Pa, using the simplified saturation vapor pressure formula described in O'Gorman and Schneider (2008b).

1.2.2 Convective quasi-equilibrium[2]

Radiation and surface fluxes destabilize the tropical atmosphere. The ensuing convective instability is released by convective cumulus clouds on the scale of $\sim$1 km, which is much smaller than the horizontal resolution of typical GCMs ($\sim$100 km). Therefore, the effect of moist convection on the GCM-resolved scales must be parameterized. That is, the subgrid-scale fluxes of moisture, heat, and momentum must be determined in terms of the resolved variables.

One standard approach to parameterize cumulus convection in GCMs is based on the quasi-equilibrium (QE) hypothesis, which was introduced by Arakawa and Schubert (1974). The hypothesis is that the generation of potential energy by processes that destabilize the atmosphere is balanced by the consumption of potential energy by moist convection at the rate that the potential energy is generated.

[2]This section follows Emanuel (2007) and Emanuel (1994).

There is observational support for the QE hypothesis (see, e.g., Emanuel 1994, and references therein), though fluctuations in the tropical atmosphere necessitate sufficient space ($\sim$100 km) and time ($\sim$1 day) averaging for the hypothesis to hold (Emanuel 2007). This thesis is concerned exclusively with the long temporal and large spatial scale aspects of the tropical climate, so it is assumed throughout that the QE hypothesis holds.

The QE hypothesis can be defined in terms of convective available potential energy (CAPE). A standard definition of CAPE integrates the buoyancy of a parcel (expressed in terms of the specific volume α, the inverse density) lifted from pressure p to the parcel's level of neutral buoyancy p_{LNB}:

$$\mathrm{CAPE}(p) = \int_{p_{LNB}}^{p} (\alpha_p - \alpha_e)\, \mathrm{d}p', \tag{1.2}$$

where $(\cdot)_e$ denotes the environmental value of a variable and $(\cdot)_p$ denotes the parcel value of a variable (Emanuel 1994). One can express CAPE in terms of the virtual (density) temperature $T_v = T(1 + r/\varepsilon)/(1 + r)$ with water vapor mixing ratio r and the ratio of the molecular weights of water and dry air ε.

$$\mathrm{CAPE}(p) = \int_{p_{LNB}}^{p} R_d(T_{vp} - T_{ve})\, \mathrm{d}ln\, p'. \tag{1.3}$$

This shows that CAPE is connected to lapse-rate based stability measures.

The QE hypothesis can be expressed as the requirement that the rate of change of CAPE, on the timescale τ that the hypothesis is valid, be near zero:

$$\frac{\partial \mathrm{CAPE}}{\partial \tau} \approx 0. \tag{1.4}$$

The QE hypothesis, being a constraint on the rate of change of CAPE, does not require a particular value of CAPE and so allows for regional variations.

Consider the limit in which CAPE is zero (termed "strict quasi-equilibrium" in the literature), i.e., the timescale τ is infinitely small. In this limit, the lapse rate will be given by that defined by the moist adiabat of a lifted parcel, typically from close

to the surface (eqn. 1.3).

In observations, not only is the rate of change of CAPE small, but also typical tropical soundings are nearly neutral (i.e., the buoyancy of a parcel lifted from the near-surface is small) to suitably defined moist adiabats (e.g., Xu and Emanuel 1989). That the stratification is close to a moist adiabat can be understood as a consequence of the difference between the timescale of moist convection ($\sim$0.5 day) and that of radiation ($\sim$20 day): $\tau_{conv} \ll \tau_{rad}$.

There are a variety of convection parameterizations that are consistent with the quasi-equilibrium hypothesis. The approach employed here follows Betts (1986) and Betts and Miller (1986) and relaxes convective unstable columns toward moist adiabatic profiles (i.e., zero CAPE) over a finite timescale. With the parameters used here, the tropical lapse rate is close to that of a moist adiabat over a wide range of climates (Schneider and O'Gorman 2008). Thus, the vertical thermal structure of the tropical atmosphere is tightly constrained by the quasi-equilibrium hypothesis.

1.2.3 Weak temperature gradients[3]

In the tropics, the magnitude of horizontal temperature variations can be estimated through scale analysis of the horizontal momentum equations (Charney 1963). In the free atmosphere, where frictional forces can be neglected, inertial accelerations scale advectively, like $\sim U^2/L$ if the Rossby number is not small, and are balanced by accelerations owing to pressure gradients, which scale like $\delta p/(\rho L)$, where δp is the scale of horizontal pressure variations and ρ is density. The density and vertical pressure variations are related by the hydrostatic relation, $p/H \sim \rho g$, where $H = RT/g$ is the pressure scale height (specific gas constant R and temperature T). If one combines the scalings from the horizontal momentum and hydrostatic equations, horizontal variations in pressure, density, and (potential) temperature (using the ideal gas law) scale like

$$\frac{\delta p}{p} \sim \frac{\delta \rho}{\rho} \sim \frac{\delta \theta}{\theta} \sim \frac{U^2}{gH} \equiv \mathrm{Fr}, \tag{1.5}$$

[3]This section closely follows section 3 of Merlis and Schneider (2010).

where $\mathrm{Fr} = U^2/(gH)$ is the Froude number. For Earth, with $H \approx 7\,\mathrm{km}$ and $g = 9.8\,\mathrm{m\,s^{-2}}$, the Froude number is $\mathrm{Fr} \lesssim 10^{-2}$ for velocities $U \lesssim 25\,\mathrm{m\,s^{-1}}$. So free-atmospheric horizontal temperature and pressure variations are expected to be small insofar as velocities are not too strong (e.g., if their magnitude is limited by shear instabilities).

This scaling argument can be generalized to include diabatic processes, which is known as the Weak Temperature Gradient (WTG) approximation of the tropical atmosphere (Sobel et al. 2001). The combination of the QE-hypothesis and WTG imply that the tropospheric temperature throughout the tropics is determined nonlocally by convecting regions (Sobel et al. 2002). The WTG approximation also has implication for the atmospheric circulation of the tropics (as reviewed by Sobel 2002, for example). The dominant balance of the water vapor budget of the simulations presented in Chapter 2 and the factors determining the meridional variations in moist static energy with its implications for Hadley circulation mass fluxes presented in Chapter 3 are both consequences of weak temperature gradients on the general circulation of the tropical atmosphere.

1.3 The problem at hand

This work examines the response of tropical climate and atmospheric circulations to changes in radiation. First, the effect of changes in the atmosphere's longwave absorber (in analogy to greenhouse gases) on climatological zonal asymmetries in the tropics is examined. Next, the response of the tropical climate and atmospheric circulations to changes in top-of-atmosphere insolation due to orbital precession is examined. The goal of this thesis is to develop and test scaling theories that account for the simulated climate changes obtained by systematically perturbing these "external" parameters.

Two appendices cover topics outside the primary area of study: the scales of linear baroclinic instability and atmospheric macroturbulence in dry atmospheres and the atmospheric circulation and surface climate of tidally locked Earth-like aquaplanets.

1.3.1 Tropical asymmetries and climate change

Deviation from zonal symmetry in the forcing and boundary conditions in the tropics—in particular, that associated with the ocean circulation—gives rise to time-mean or climatological zonal asymmetries in the surface climate and atmospheric circulation. For example, the relatively cold surface temperatures in the eastern Pacific basin and the relatively warm surface temperatures in the western Pacific basin are a consequence of the ocean circulation's energy transport.

Another prominent zonal asymmetry is the large-scale overturning circulation in the longitude-pressure plane. In the Pacific ocean basin, this circulation is named the Walker circulation after Sir Gilbert Walker who discovered the global-scale anticorrelation in surface pressure across the basin that is known as the Southern Oscillation.

The Walker circulation's interannual fluctuations have a notable role as the atmospheric component of the interannual variability of the coupled atmosphere–ocean system, known as El Niño–Southern Oscillation. As the Walker circulation plays a role in determining the variations of precipitation in longitude (for example, the difference between climatologically wet regions in the west like Indonesia and the dry regions in the east near the coast of South America), its interannual fluctuations in the tropical Pacific are noteworthy for their reorganization of tropical precipitation (e.g., Lintner and Chiang 2005).

How does the Walker circulation respond to increases in greenhouse gas concentrations? The work of Knutson and Manabe (1995) showed that the circulation weakens in a transient climate change simulation ($4\times$ CO_2) with a coupled GCM; they interpreted these changes in terms of changes in the (dry) thermodynamic and water vapor budgets. Held and Soden (2006) also made use of the water vapor budget to understand changes in the zonally asymmetric circulation in comprehensive GCM simulations prepared for the fourth Intergovernmental Panel on Climate Change assessment report. Chapter 2 extends these studies by examining the change in the Walker circulation over a wide range of climates in an idealized GCM.

The east–west surface temperature contrast over the wide range of climates is

examined and compared to a scaling estimate in Chapter 2. This chapter exposes links between the zonal asymmetries in the mean overturning atmospheric circulation (the Walker circulation), precipitation, and surface temperatures for GHG-type climate changes.

1.3.2 Orbital forcing

Orbital forcing gives rise to climate changes on timescales (∼10–100 kyr) that are much longer than those associated with anthropogenic greenhouse gas emissions. The climate forcing associated with changes in Earth's orbit—the astronomical parameters and the associated top-of-atmosphere insolation—is well-known for the past ∼10 Myr. The details of the changes in surface climate are less well-known as there are uncertainties in the geological reconstructions of climate variables. As such, it is of interest to develop physically based estimates of the range of possible climate changes. This will help interpret proxy evidence and resolve the ambiguities arising from non-climatic influences on proxies.

Earth's orbit can be described by the parameters obliquity Φ (the tilt of the planet relative to the plane of the orbit), the eccentricity ϵ (a measure of the deviation of the orbit from circular), and perihelion Λ (the point of the orbit when the planet is closest to the Sun). Earth's obliquity varies on ∼40 kyr timescales, and in the last million years, it has varied between $22.1°and24.5°$ (Berger 1978). Obliquity variations affect the meridional structure top-of-atmosphere insolation: when the obliquity is low, the pole receives less sunlight in the summer and the annual-mean equator-to-pole insolation gradient is higher. Earth's eccentricity varies on ∼100 kyr timescales, and in the last million years, it has varied between $0.005and0.057$ (Berger 1978). The eccentricity of the orbit introduces a seasonal cycle in insolation associated with the varying Earth–Sun distance (in contrast to the seasonal cycle of a circular orbit that is the result of the planet's obliquity). Earth's perihelion precesses over the full range of values in ∼20 kyr. The effect of changes in eccentricity and perihelion on the top-of-atmosphere insolation are discussed in the appendix of this introduction. The

essential results are that perihelion variations do not affect annual-mean insolation at a given latitude, but do affect the instantaneous insolation by an amount that depends on the eccentricity.

Chapters 3 and 4 examine the changes in the tropical climate when the perihelion is varied. As the annual-mean insolation does not change when the perihelion is varied, climate variables that are linear in insolation will not change; if the annual-mean of a climate variable does change when the perihelion is varied, there is a nonlinear process that rectifies the insolation changes. We examine changes in the surface climate when precession is varied between extremal values, from northern hemisphere winter solstice to northern hemisphere summer solstice, and determine which aspects of the climate have annual-mean changes and what nonlinear process is acting to produce the annual-mean changes.

The principal rectified variable is precipitation, and the mechanism by which this occurs is assessed. The changes in the vertically-integrated water vapor convergence can be decomposed into thermodynamic (i.e., dominated by changes in water vapor concentration with fixed circulation) or dynamic (i.e., dominated by changes in circulation with fixed water vapor concentration) components (e.g., Held and Soden 2006). In aquaplanet simulations, the thermodynamic component dominates the precession-forced precipitation changes. The annual-mean changes are due to the quadratic nonlinearity associated with the correlation between seasonal cycle of the Hadley circulation mass convergence and the seasonal cycle of the perturbation specific humidity. In simulations with subtropical continents, the dynamic and thermodynamic component of the precipitation changes are both important.

The Hadley circulation in aquaplanet simulations responds to orbital precession in a somewhat surprising manner. When the perihelion is in northern hemisphere summer, the cross-equatorial Hadley circulation in that season weakens relative to the simulation with perihelion at December solstice. As the cross-equatorial Hadley circulation is close to the angular momentum-conserving limit, at least in the ascending branch, the circulation's energy flux divergence is determined by the top-of-atmosphere radiation balance. The Hadley circulation energy flux divergence in-

creases to balance the additional insolation, but this is accomplished by an increase in the gross moist stability, the vertical energy contrast of the Hadley circulation, that is sufficiently large that the mass fluxes decrease. As such, the aquaplanet Hadley circulation mass fluxes do not respond as one might expect from nonlinear, angular momentum-conserving circulations with fixed stability (Lindzen and Hou 1988).

Chapter 4 examines how the presence of a continental region in subtropical latitudes alters the response of the atmospheric circulation to orbital precession. In this case, the Hadley circulation does increase with increasing insolation. To understand this, the top-of-atmosphere energy balance and the surface moist static energy distribution are examined. First, the land-sea contrast in surface energy storage (substantial storage over oceanic regions and negligible storage over land regions) sets up a small meridional scale region in which the atmosphere energy flux divergence must balance the radiative perturbation. To understand why it is the cross-equatorial, monsoonal Hadley circulation that accomplishes the additional energy flux, we consider the surface moist static energy maximum, as this determines the poleward boundary of monsoonal circulations (Privé and Plumb 2007a). The moist static energy increases in response to additional insolation, in particular over the region with low surface heat capacity. To understand why the changes in the circulation in the summer season are not offset by the winter season, we consider the time-dependent angular momentum balance. Whereas the ascending branch of the Hadley circulation is near the angular momentum-conserving limit, the descending branch is not. The result is that the strength of the descent that occurs in winter is not determined solely by energetic considerations.

1.4 Appendix: Insolation changes associated with non-circular orbits[4]

The insolation of an eccentric orbit can be related to that of a circular orbit. First, the insolation of a circular orbit with obliquity Φ is defined by $Q\tilde{s}(\Phi;\phi,t)$, where Q is the solar constant and the flux factor $\tilde{s}$ varies between 0 and 1 and depends on latitude ϕ and time of year t. The relationship between the insolation of a non-circular orbit with eccentricity ϵ and perihelion Λ to that of the circular orbit is

$$Qs(\epsilon,\Lambda,\Phi;\phi,t) = Q\tilde{s}(\Phi;\phi,\omega(t))\frac{a^2}{\tau^2(t)}, \tag{1.6}$$

where a is the semi-major axis of the orbit, $\tau(t)$ is the Earth–Sun distance at time t, and $\omega(t)$ is the angle in the orbital plane between the line connecting the Earth to the Sun at time t and the line connecting the Earth to the Sun at vernal equinox. $\omega(t)$ is called the true longitude. The Earth–Sun distance τ is geometrically related to the true longitude ω

$$\tau(t) = \frac{a(1-\epsilon^2)}{1+\epsilon cos(\omega(t)-\Lambda)}. \tag{1.7}$$

The time rate of change of the true longitude is a consequence of the conservation of angular momentum—the planet proceeds more rapidly through the orbit when it is closer to the Sun than when it is farther away. Expressed in time units in which 2π is one year, it is

$$\frac{d\omega}{dt} = \frac{a^2}{\tau^2}(1-\epsilon^2)^{1/2} = \frac{[1+\epsilon cos(\omega(t)-\Lambda)]^2}{(1-\epsilon^2)^{3/2}}, (\omega(0)=0). \tag{1.8}$$

The insolation of the eccentric orbit is

$$Qs(\epsilon,\Lambda,\Phi;\phi,t) = Q\tilde{s}(\Phi;\phi,\omega)\frac{d\omega}{dt}(1-\epsilon^2)^{-1/2}. \tag{1.9}$$

[4]The material in this section follows the treatment in Held (1982).

When integrated over a year, the right-hand side of the equation is zero as can be seen by integration by substitution. This demonstrates that the annual-mean insolation at each latitude ϕ does not depend on the perihelion Λ. The annual-mean insolation changes by a very small amount when the eccentricity is changed ($\lesssim$0.1% for Earth-like changes in ϵ).

Rewriting the insolation of the eccentric orbit (1.9) to make the perihelion-dependence explicit using eqn. 1.8,

$$Qs(\epsilon, \Lambda, \Phi; \phi, t) = Q\tilde{s}(\Phi; \phi, \omega)\frac{[1 + \epsilon\cos(\omega(t) - \Lambda)]^2}{(1 - \epsilon^2)^2}, \tag{1.10}$$

one can see that the effect of varying perihelion between extreme phases on instantaneous insolation is 4ϵ, neglecting ϵ^2 terms. So, the magnitude of insolation changes due to orbital precession depends on the eccentricity. For Earth's recent orbital history, this magnitude is $\sim$7–20%.

Chapter 2

Changes in zonal surface temperature gradients and Walker circulations in a wide range of climates

This chapter, excluding its Appendices B and C, is in press in *Journal of Climate* (Merlis and Schneider 2011).

2.1 Abstract

Variations in zonal surface temperature gradients and zonally asymmetric tropical overturning circulations (Walker circulations) are examined over a wide range of climates simulated with an idealized atmospheric general circulation model (GCM). The asymmetry in the tropical climate is generated by an imposed ocean energy flux, which does not vary with climate. The range of climates is simulated by modifying the optical thickness of an idealized longwave absorber (representing greenhouse gases).

The zonal surface temperature gradient in low latitudes generally decreases as the climate warms in the idealized GCM simulations. A scaling relationship based on a two-term balance in the surface energy budget accounts for the changes in the zonally asymmetric component of the GCM-simulated surface temperature.

The Walker circulation weakens as the climate warms in the idealized simulations,

as it does in comprehensive simulations of climate change. The wide range of climates allows a systematic test of energetic arguments that have been proposed to account for these changes in the tropical circulation. The analysis shows that a scaling estimate based on changes in the hydrological cycle (precipitation rate and saturation specific humidity) accounts for the simulated changes in the Walker circulation. However, it must be evaluated locally, with local precipitation rates. If global-mean quantities are used, the scaling estimate does not generally account for changes in the Walker circulation, and the extent to which it does is the result of compensating errors in changes in precipitation and saturation specific humidity that enter the scaling estimate.

2.2 Introduction

The evolution of zonal surface temperature gradients in the tropics is of interest in the study of future and past climates (e.g., Knutson and Manabe 1995; Fedorov et al. 2006). Recently, the changes in the zonally asymmetric component of the tropical overturning circulation, the Walker circulation, have been highlighted as a robust response to warming in climate change simulations with comprehensive GCMs (Held and Soden 2006; Vecchi and Soden 2007). Here, we examine the response of these zonally asymmetric aspects of the mean tropical climate to radiative perturbations in an idealized GCM and test theoretical arguments designed to account for their changes.

How zonal surface temperature gradients evolve as the climate warms is unclear. On one hand, increased cooling associated with the upwelling of cold water on the eastern ocean margins may lead to increased zonal temperature gradients in transient warmings (Clement et al. 1996), and this mechanism appears to be important in coupled GCM simulations (Held et al. 2010). On the other hand, paleoclimate evidence from the Pliocene suggests substantially weakened or collapsed zonal temperature gradients in a climate only somewhat warmer than Earth's current climate (e.g., Fedorov et al. 2006). (However, see Wunsch (2009) for an alternative interpre-

tation of the data.) The multi-model mean of the fourth Intergovernmental Panel on Climate Change (IPCC) assessment models shows little change in zonal temperature gradients in the Pacific basin over the twenty-first century (DiNezio et al. 2009). As a step toward understanding the full climate dynamics that control the zonal surface temperature gradient in the tropics, we develop a scaling relationship based on the surface energy budget and compare it to the results of the idealized GCM simulations.

The connection between changes in the hydrological cycle and large-scale atmospheric circulations in response to radiative forcing, for instance, by changed greenhouse gas concentrations, can be subtle. For example, the mass fluxes in the Hadley cell and extratropical eddy kinetic energy can vary non-monotonically as a longwave absorber is systematically varied in an idealized GCM, with implications for water vapor fluxes and the distribution of evaporation and precipitation (O'Gorman and Schneider 2008b,a; Schneider et al. 2010; Levine and Schneider 2011).

Analysis of comprehensive GCM simulations suggests the connection between changes in the hydrological cycle and upward mass fluxes is straightforward (Held and Soden 2006; Vecchi and Soden 2007). The argument is that precipitation, which is constrained by the energy balance at the surface in the global mean, increases with warming more slowly than near-surface specific humidity, which increases similarly to the rate given by the Clausius-Clapeyron relation for small changes in relative humidity; thus, the upward vertical velocity that gives rise to condensation of water vapor weakens. This scaling argument is sometimes interpreted to account for changes in the Walker circulation (e.g., Vecchi et al. 2006), in part because changes in the zonally asymmetric component of the circulation are larger than those in the zonally symmetric component (Held and Soden 2006). A difficulty in applying the hydrological cycle argument directly to local circulations, such as the Walker circulation, is that the surface energy balance constraint on the precipitation is lost, as water vapor convergence depends locally on the atmospheric circulation. A central goal of this work is to assess the extent to which the hydrological cycle arguments apply locally to the Walker circulation, and to compare this to global-mean versions of the scaling arguments to determine the extent to which they are adequate.

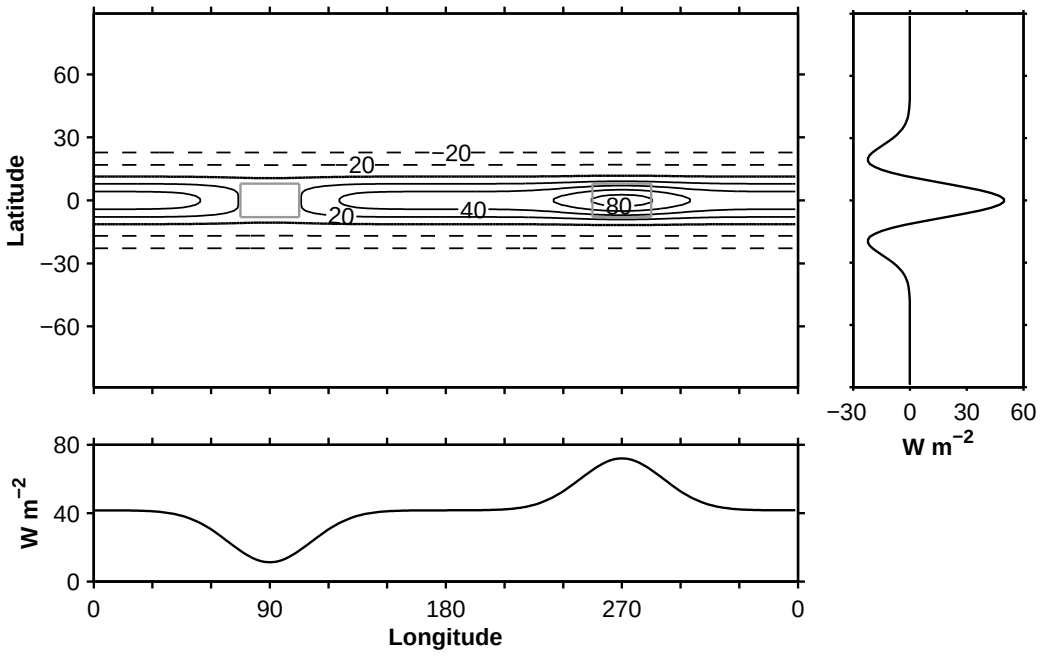

Figure 2.1. Ocean energy flux divergence, Q-flux, with positive values indicate cooling tendencies. Large panel: longitude-latitude Q-flux contours with contour interval of $20\,\mathrm{W\,m^{-2}}$ and negative values are dashed. The gray rectangles indicate the averaging regions. Right panel: latitude vs. zonal-mean Q-flux. Bottom panel: equatorial Q-flux (averaged within 8° of the equator) vs. longitude.

Here, we use an idealized GCM to systematically examine the response of the zonally asymmetric tropical surface temperature and the Walker circulation to changes in the atmosphere longwave opacity. A scaling estimate based on the surface energy balance accounts for the changes in the zonal surface temperature gradient. We assess the hydrological cycle estimate for changes in the Walker circulation by applying it locally. The scaling estimate is accurate, though it requires knowledge of the precipitation field. In contrast, the global-mean version of the scaling estimate does not in general account for the Walker circulation changes.

2.3 Idealized GCM

2.3.1 Model description

We use an idealized, moist primitive-equation atmospheric GCM similar to those described in O'Gorman and Schneider (2008b) and Frierson et al. (2006). Briefly, the model includes an active hydrological cycle with a simplified Betts-Miller convection scheme (Frierson 2007). The scheme relaxes over a fixed timescale convectively unstable columns to moist pseudoadiabatic temperatures with constant (70%) relative humidity. It has a gray longwave radiation scheme, and a slab-ocean surface boundary condition with the heat capacity of 1 m of water. The top-of-atmosphere insolation is an idealized, annual-mean profile, and there is shortwave absorption in the atmosphere, both of which are as described in O'Gorman and Schneider (2008b). There is no condensed water phase in the atmosphere (i.e., there are no clouds). The climate is perturbed by varying the optical depth in the gray radiation scheme by a multiplicative factor to mimic variations in the trapping of longwave radiation due to variations in greenhouse gas concentrations. The primitive equations are integrated using the spectral transform method in the horizontal with T85 resolution (but the simulation results are similar with T42 resolution). Finite differences in $\sigma = p/p_s$ (with pressure p and surface pressure p_s) discretize the vertical coordinate, with 30 unevenly spaced levels. The time-stepping is semi-implicit, with a leapfrog timestep of 300 s. The simulation statistics are averaged over the last 1100 days of the simulation following a spinup period of either 700 days for an isothermal, resting initial condition or 300 days for an initial condition from an equilibrated simulation with similar optical thickness. Aside from the horizontal resolution and timestep, the only difference between the simulations presented here and those presented in O'Gorman and Schneider (2008b) is that we include a representation of ocean energy flux divergence in the slab ocean and present fewer simulated climates.

2.3.2 Prescribed ocean energy flux divergence

The surface boundary condition is a slab ocean that accounts for the radiative and turbulent surface fluxes. Additionally, it has a prescribed ocean energy flux divergence that represents the influence of the ocean circulation on the surface temperature. This is commonly referred to as a Q-flux in climate modelling.

The Q-flux consists of a component that varies only in latitude and represents the divergence of the meridional ocean energy flux

$$\nabla \cdot F_0(\phi) = Q_0 \left(\frac{1 - 2\phi^2}{\phi_0^2}\right) \exp\left(-\frac{\phi^2}{\phi_0^2}\right), \tag{2.1}$$

where ϕ is latitude, $\phi_0 = 16°$, and $Q_0 = 50\,\mathrm{Wm}^{-2}$ following Bordoni (2007) and Bordoni and Schneider (2008). The meridional component of the Q-flux is necessary to have an Earth-like tropical circulation in the reference climate; without it, the zonal-mean (Hadley) circulation is sufficiently strong that there is mean ascending motion everywhere along the equator (i.e., the descending branch of the Walker circulation is weaker than the Hadley circulation).

Zonal symmetry is broken by adding and subtracting Gaussian lobes along the equator that are spaced 180° longitude apart,

$$\begin{aligned} \nabla \cdot (F_0(\phi) + F_1(\lambda, \phi)) = \nabla \cdot F_0(\phi) \\ + Q_1 \exp\left(-\frac{(\lambda - \lambda_E)^2}{\lambda_1^2} - \frac{\phi^2}{\phi_1}\right) \\ - Q_1 \exp\left(-\frac{(\lambda - \lambda_W)^2}{\lambda_1^2} - \frac{\phi^2}{\phi_1}\right), \end{aligned} \tag{2.2}$$

where λ is longitude, $\lambda_1 = 30°$, $\lambda_E = 90°$, $\lambda_W = 270°$, $\phi_1 = 7°$, and $Q_1 = 40\,\mathrm{Wm}^{-2}$.

The resulting Q-flux, shown in Fig. 2.1, has similar magnitude and spatial scale to reanalysis estimates (e.g., Trenberth et al. 2001, their Fig. 5).

2.3.3 Series of simulations

As in O'Gorman and Schneider (2008b), the longwave optical depth is varied to mimic changes in greenhouse gas concentrations. The optical depth $\tau = \alpha\tau_{\rm ref}$ is the product of a multiplicative factor α and a reference profile $\tau_{\rm ref}$ that depends on latitude and pressure,

$$\tau_{\rm ref} = [f_l\sigma + (1 - f_l)\sigma^4][\tau_{eq} + (\tau_p - \tau_{eq})\sin^2\phi], \tag{2.3}$$

where $f_l = 0.2$ and the reference optical depths at the equator and pole are $\tau_{eq} = 7.2$ and $\tau_p = 1.8$, respectively. We conduct simulations with rescaling factors $\alpha =$ (0.6, 0.7, 0.8, 0.9, 1.0, 1.2, 1.4, 1.6, 1.8, 2.0, 2.5, 3.0, 4.0, 6.0). The range of optical depths presented here is reduced compared to O'Gorman and Schneider (2008b); simulations with the smallest optical depths are omitted because the fixed meridional Q-flux leads to reversed Hadley cells and concomitant double intertropical convergence zones in sufficiently cold climates. In total, fourteen simulations are presented here.

2.4 Zonal surface temperature gradients

2.4.1 Simulation results

Figure 2.2 shows the simulated zonal surface temperature differences averaged over the regions indicated in Fig. 2.1 for each of the equilibrated climates, which are identified by the time- and global-mean (denoted $\langle\cdot\rangle$) surface temperature $\langle T_s\rangle$. Following O'Gorman and Schneider (2008b), the reference climate with $\alpha = 1.0$ is indicated by a filled symbol. The east–west surface temperature difference ΔT_s decreases nearly monotonically as the climate warms and varies by more than a factor of three over the simulated range of climates.

The simulated zonal temperature difference in the reference climate (1.4 K) is smaller than that in Earth's current climate ($\sim$5 K). While we have used a Q-flux that has comparable magnitude to estimates for the current climate, the lack of clouds and the concomitant zonal asymmetry in cloud radiative forcing leads to a smaller

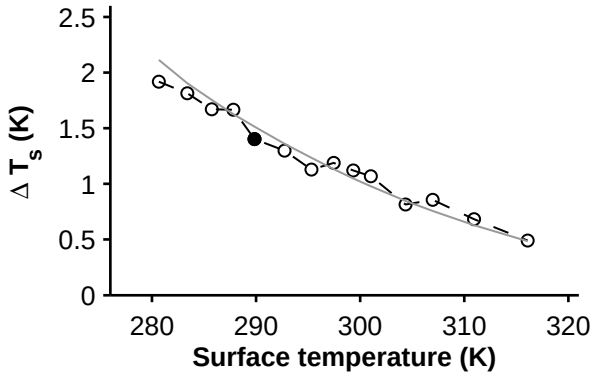

Figure 2.2. Zonal surface temperature difference (west minus east in Fig. 2.1) vs. global-mean surface temperature of GCM simulations (circles with black dashed line), and scaling estimate (2.8) (gray line). The averaging conventions used to evaluate the scaling estimate are described in the text.

zonal asymmetry in the equilibrated surface temperature. One remedy would be to impose a larger asymmetry in the Q-flux, since in quasi-equilibrium theory, there is a near equivalence between surface fluxes and radiative forcing (Sobel et al. 2010, section 2.3). However, we chose not to amplify the Q-flux asymmetry. Therefore, it is more meaningful to consider fractional changes in the simulated zonal surface temperature contrast than the magnitude of the simulated changes. Our results hence may give changes in the surface temperature contrasts that, in reality, would likely be modified by processes we ignored, such as cloud-radiative feedbacks.

2.4.2 Scaling estimate

Figure 2.3 shows the surface energy budget as a function of longitude for the Earth-like reference simulation. Examining the variations in longitude of the surface energy balance reveals that the dominant balance in the zonally asymmetric component is between the prescribed Q-flux and the evaporative fluxes. This is to be expected in Earth-like and warmer climates where the Bowen ratio (ratio of sensible to latent surface fluxes) is small in the tropics. An analogous ratio can be formed for the net longwave radiation at the surface (Pierrehumbert 2010), and this is also small for sufficiently warm climates.

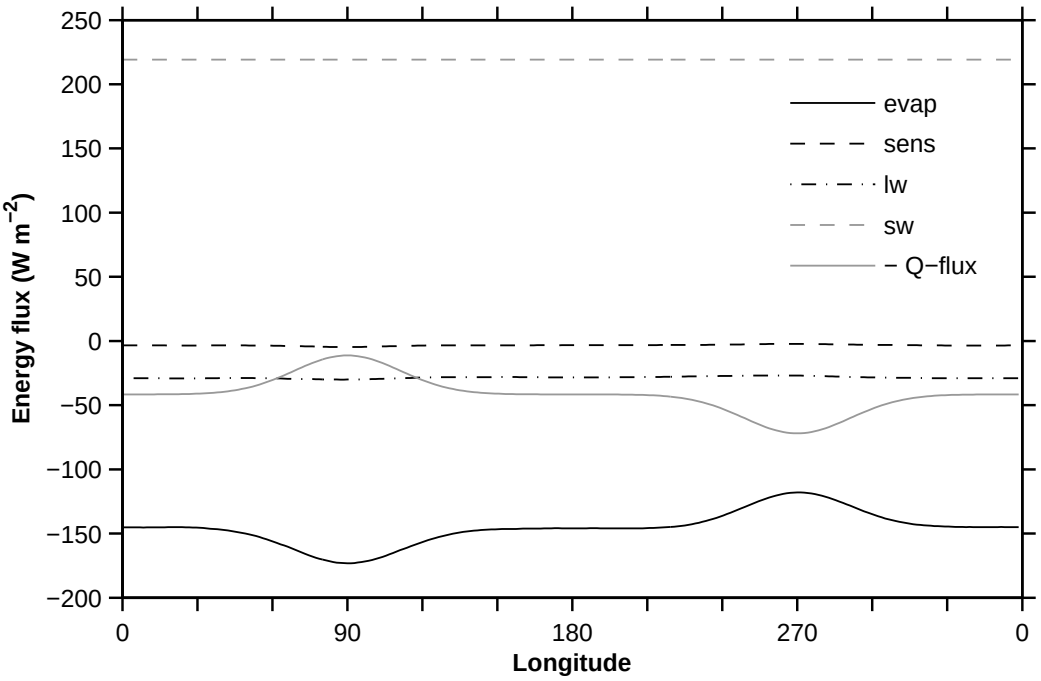

Figure 2.3. Surface energy fluxes of the reference simulation vs. longitude averaged within 8° of equator. "lw" and "sw" refer to the net longwave and shortwave radiative fluxes at the surface, respectively.

This two-term balance between the zonally asymmetric component of the Q-flux $\nabla \cdot F_1$ and evaporation holds over the range of climates we simulate, so that

$$\Delta \left(\nabla \cdot F_1 \right) \sim \Delta LE, \tag{2.4}$$

where Δ refers to east–west differences.

As the Q-flux (ocean energy flux divergence) is fixed, the bulk aerodynamic formula for evaporative fluxes can be manipulated with suitable assumptions to invert the zonal difference in the evaporative fluxes into a zonal difference in the surface temperature. The evaporative fluxes are computed by the bulk aerodynamic formula

$$E = \rho c_d ||\mathbf{v}|| (q_s(T_s) - q) \approx \rho c_d ||\mathbf{v}|| (1 - \mathcal{H}) q_s(T_s), \tag{2.5}$$

with air density ρ, drag coefficient c_d, surface wind speed $||\mathbf{v}||$, saturation specific

humidity q_s, specific humidity of surface air q, surface temperature T_s, and surface relative humidity $\mathcal{H}$. The second formula is approximate in that the ratio of the specific humidity and the saturation specific humidity is set equal to the relative humidity and in that the air–sea temperature difference is neglected. Neglecting the air–sea temperature difference is justifiable because the subsaturation of air dominates over the air–sea temperature difference for conditions typical of tropical oceans.

For the climate changes we are examining, the east–west evaporation difference then scales like the east–west difference in the surface saturation specific humidity[1]

$$\Delta E \sim \Delta q_s(T_s). \tag{2.6}$$

This is the result of the strong dependence of the saturation specific humidity q_s on temperature (fractional changes of $\sim 7\%\,\mathrm{K}^{-1}$ for Earth-like temperatures). In contrast, changes in the surface relative humidity $\mathcal{H}$ are relatively small. For example, Schneider et al. (2010) presented an argument based on a simplified surface energy budget that suggests $\sim 1\%\,\mathrm{K}^{-1}$ changes in $\mathcal{H}$. Regional changes that affect the zonal gradient of relative humidity are potentially important, but neither comprehensive GCM simulations (O'Gorman and Muller 2010) nor the idealized GCM simulations presented here exhibit substantial changes in the zonal relative humidity gradient. The neglected changes in the air-sea temperature difference and surface wind speed are also generally smaller than the changes in the surface saturation specific humidity.

To obtain an east–west surface temperature difference, rather than a saturation specific humidity difference, we linearize the saturation specific humidity,

$$\Delta q_s(T_s) \approx \frac{\partial q_s}{\partial T} \Delta T_s. \tag{2.7}$$

The resulting scaling estimate for the east–west temperature difference is the product of the east–west saturation specific humidity difference Δq_s and the inverse of the

[1]We are not suggesting that this scaling holds in general (see, e.g., O'Gorman and Schneider (2008b) and our Fig. 2.6 for a counterexample in the global mean), but only for the zonal difference in the tropics.

rate of change of the saturation specific humidity with temperature:

$$\Delta T_s \sim \Delta q_s \left(\frac{\partial q_s}{\partial T} \right)^{-1}. \tag{2.8}$$

For invariant ocean energy fluxes, as in the idealized GCM simulations, Δq_s is approximately constant by Eqns. (2.4) and (2.6), and the east–west surface temperature difference will decrease with warming by an amount given by the rate of change of the saturation specific humidity with temperature (i.e., given by the Clausius-Clapeyron relation as the surface pressure is nearly constant), evaluated using a temperature that is representative of the surface in the tropics.

The decrease in the zonal temperature difference in a warming scenario can be anticipated by considering the counterexample of invariant zonal surface temperature gradients: If the east–west temperature difference remained the same as the mean climate warmed, in the absence of changes in near-surface relative humidity, the east–west difference in evaporative fluxes would rapidly increase with warming. The resulting zonal asymmetry in the evaporation would be too large to be balanced by an invariant ocean energy flux, and the other terms in the surface energy balance are too small to restore equilibrium. In a transient adjustment, the excess in evaporation would lead to a reduction in the east–west surface temperature asymmetry as, for example, the large evaporation over warm regions would cool the surface. The sensitivity of the evaporative fluxes to climate change and concomitant reduction in zonal surface temperature gradients with warming was documented in the GCM simulations of Knutson and Manabe (1995), who called it "evaporative damping".

These approximations are adequate for the longwave radiation-induced climate changes in the idealized GCM simulations, though they may not be in general. For example, in analyses of climate change simulations, Xie et al. (2010) showed that changes in surface winds must be accounted for in the surface energy budget of some regions, and DiNezio et al. (2009) showed that cloud-radiative feedbacks affect the net surface shortwave radiation.

2.4.3 Assessment of scaling estimate

Fig. 2.2 shows the scaling estimate (2.8) in gray. The derivative of the saturation specific humidity with respect to temperature in (2.8) is evaluated with the same simplified formulation for the saturation specific humidity as is used in the GCM, using the simulated time- and zonal-mean surface temperature averaged within 8° of latitude of the equator. The saturation specific humidity difference Δq_s, evaluated over the averaging regions in Fig. 2.1, varies by ∼15% over the range of simulations, and we use the mean value, 2.4×10^{-3}, in the scaling estimate. The magnitude of the variations in Δq_s is consistent with the magnitude of the neglected terms in the bulk aerodynamic formula. Overall, there is close agreement (maximum deviations ∼15%) between the scaling estimate and the results of the GCM simulations.

We note that while the simulations and scaling estimate feature rapidly decreasing zonal temperature gradients as the mean temperature increases ($7.4\%\,\mathrm{K}^{-1}$ at the reference climate), the decreases are not as rapid as proxies of the Pliocene suggest ($\sim$15–30$\%\,\mathrm{K}^{-1}$). But it is possible that the neglected radiative and ocean feedbacks increase the sensitivity to changes.

2.5 Walker circulation

2.5.1 Simulation results

Figure 2.4 shows the zonally asymmetric component of the time-mean pressure velocity, $Dp/Dt = \omega$, in the longitude-sigma plane for three simulations.[2] The zonally asymmetric pressure velocity is large over the regions of perturbed Q-flux; it is small elsewhere. The pressure depth over which it has large amplitude increases with warming because the tropopause height increases; its magnitude decreases with warming. Note that a consequence of the Walker circulation's localization over the Q-flux perturbations is that the averaging convention we have chosen is adequate to capture

[2] All figures show $p_s D\sigma/Dt$, which differs only slightly (∼0.1% in the region of interest) from Dp/Dt as $\sigma Dp_s/Dt$ is small.

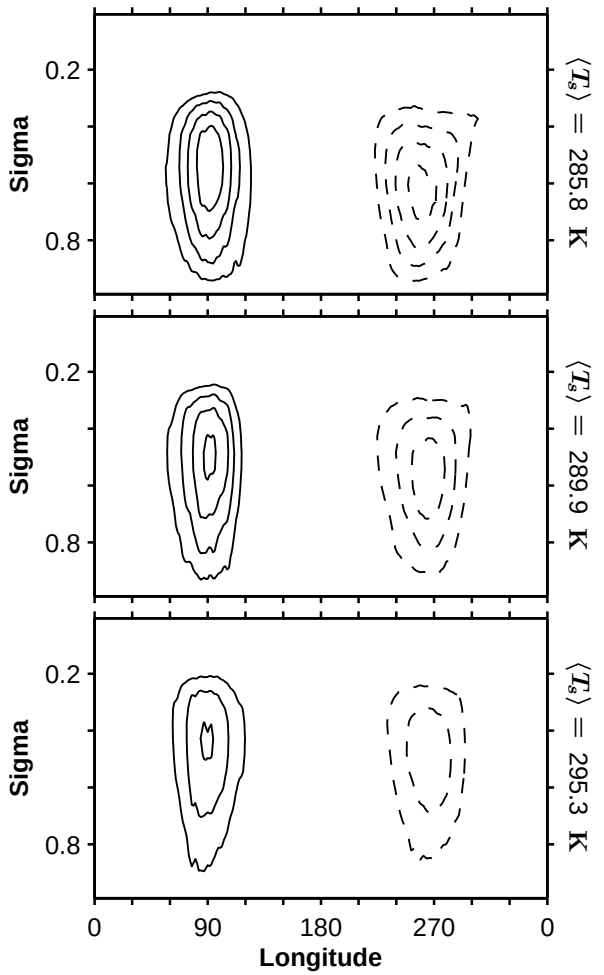

Figure 2.4. Contours of the zonally asymmetric component of the time-mean pressure velocity $\overline{\omega^*}$ in the longitude-sigma plane averaged within 8° of the equator for three simulations with global-mean surface temperature $\langle T_s \rangle$ indicated on the right. The contour interval is $0.01\,\mathrm{Pa\,s^{-1}}$ with positive values (descending motion) dashed. The zero contour is omitted.

nearly all of the ascending and descending mass fluxes—it is a closed circulation and alternative measures, such as surface pressure differences, yield similar results.

Figure 2.5 shows that the Walker circulation mass flux in the ascending region rapidly weakens with warming. The fractional rate of decrease is $4.4\%\,\mathrm{K^{-1}}$ at the reference climate relative to the global-mean surface temperature. (The fractional change is larger relative to local surface temperature changes as the warming is greater in high latitudes.) The Walker circulation varies by a factor of six over the simulated

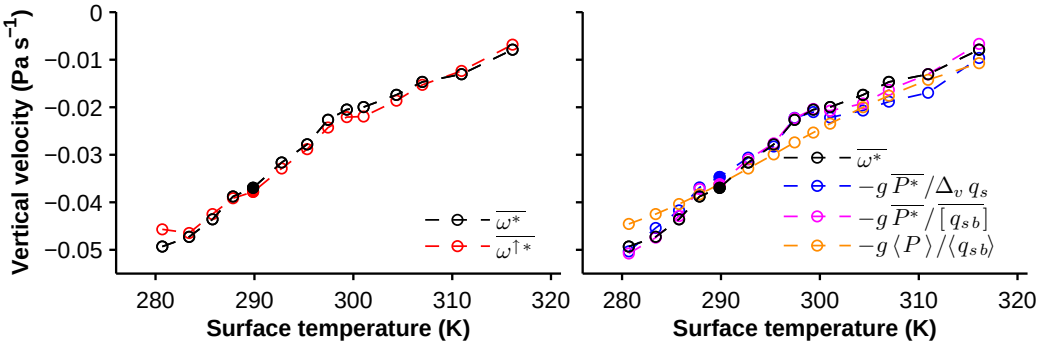

Figure 2.5. Left: zonally asymmetric component of the pressure velocity $\overline{\omega^*}$ (black) and zonally asymmetric component of the upward pressure velocity $\overline{\omega^{\uparrow *}}$ (red) averaged over the ascending region of the Walker circulation (cf. Fig. 2.1). The pressure velocity $\overline{\omega^*}$ is evaluated on the sigma level where it is minimum (strongest ascent), and $\overline{\omega^{\uparrow *}}$ is evaluated on the same level. The upward velocity has been multiplied by a factor of 1.3 determined by minimizing the mean squared deviation between $\overline{\omega^{\uparrow *}}$ and $\overline{\omega^*}$. Right: zonally asymmetric component of the pressure velocity, $\overline{\omega^*}$, (black) and hydrological cycle scaling estimates: $-g\,\overline{P^*}/\Delta_v q_s$ (blue), $-g\,\overline{P^*}/\overline{[q_{sb}]}$ (magenta), and $-g\,\langle P\rangle/\langle q_{sb}\rangle$ (orange). The scaling estimates are multiplied by constants of 1.5, 1.7, and 0.8, respectively, chosen to minimize the mean squared deviations between the scaling estimates and $\overline{\omega^*}$. The near-surface saturation specific humidity is evaluated on a fixed sigma level $\sigma = 0.96$. The free-tropospheric contribution to the saturation specific humidity difference $\Delta_v q_s$ is evaluated on a sigma level that is a fixed amount larger than the sigma level of the tropopause, σ_t: $\sigma = \sigma_t + 0.15$. The scale estimates $\overline{P^*}/\Delta_v q_s$ and $\overline{P^*}/\overline{[q_{sb}]}$ are evaluated within 8° of the equator and $\langle P\rangle/\langle q_{sb}\rangle$ is evaluated using global means. Zonal averages are used for $\Delta_v q_s$ and $\overline{[q_{sb}]}$.

range of climates. In this figure, the zonally asymmetric component of the pressure velocity is evaluated on the sigma surface where it is maximum, which varies from $\sigma = 0.60$ in the coldest climate to $\sigma = 0.32$ in the warmest climate. These changes roughly follow those of the zonal-mean tropical tropopause (averaged within 8° of the equator) which rises from $\sigma = 0.24$ to $\sigma = 0.03$ determined by the World Meteorological Organization (WMO) $2\,\mathrm{K\,km^{-1}}$ lapse rate criterion. If the Walker circulation is evaluated using fixed sigma levels in the lower troposphere, the weakening with warming is more rapid owing to the combined changes in the vertical structure of the circulation and the changes, shown in Fig. 2.5, that are independent of the vertical structure.

2.5.2 Scaling estimate

In saturated ascending motion, the vertical advection of saturation specific humidity q_s leads to condensation c,

$$-\omega^{\uparrow}\partial_p q_s \approx c, \tag{2.9}$$

where $\omega^{\uparrow} = \omega H(-\omega)$ is a truncated upward pressure velocity and H is the Heaviside step function (Schneider et al. 2010). For a mass-weighted vertical average taken from the lifting condensation level to the tropopause (denoted by $\{\cdot\}$), the precipitation P balances the vertical advection of specific humidity:

$$-\left\{\omega^{\uparrow}\partial_p q_s\right\} \approx P. \tag{2.10}$$

Equation 2.10 assumes that we are averaging over horizontal scales that are large enough to include convective downdrafts and the associated evaporation of condensate. Neglecting transients aside from those implicitly included by using the truncated vertical velocity, equation (2.10) can be decomposed into zonal-means, denoted by $[\cdot]$, and deviations thereof, denoted by $(\cdot)^*$. The time-mean, denoted by $\overline{(\cdot)}$, of the zonally asymmetric component of the budget is then

$$-\left\{\overline{\omega^{\uparrow *}}\partial_p\overline{[q_s]} + \overline{[\omega^{\uparrow}]}\partial_p\overline{q_s^*} + \overline{\omega^{\uparrow *}}\partial_p\overline{q_s^*} - \left[\overline{\omega^{\uparrow *}}\partial_p\overline{q_s^*}\right]\right\} \approx \overline{P^*}. \tag{2.11}$$

Terms 2-4 on the left-hand side, which include zonal asymmetries in saturation specific humidity $\overline{q_s^*}$, are negligible as a result of the weak temperature gradients in the free troposphere of the tropics (Charney 1963; Sobel et al. 2001). In the simulations, these terms combined are an order of magnitude smaller than the terms in the dominant balance

$$-\left\{\overline{\omega^{\uparrow *}}\partial_p\overline{[q_s]}\right\} \approx \overline{P^*}. \tag{2.12}$$

Our interest is in the zonally asymmetric component of the tropical overturning circulation (denoted $\overline{\omega^*}$), the Walker circulation, and so we estimate the mass fluxes

of the ascending or descending branches from (2.12) as

$$-\frac{\overline{\omega^*}}{g} \sim -\frac{\overline{\omega^{\uparrow *}}}{g} \sim \frac{\overline{P^*}}{\Delta_v q_s}, \tag{2.13}$$

where $\Delta_v q_s$ is a zonal-mean vertical saturation specific humidity difference.

This is closely related to the thermodynamic budget in the tropics where the stratification is close to moist adiabatic. On a moist adiabat (at constant saturation equivalent potential temperature θ_e^*), the vertical gradients of potential temperature θ and saturation specific humidity (assuming constant latent heat of vaporization) are related by

$$-(T/\theta)\partial_p \theta|_{\theta_e^*} \approx (L/c_p)\partial_p q_s|_{\theta_e^*} \tag{2.14}$$

(e.g., Iribarne and Godson 1981). Thus, as discussed in Held and Soden (2006) and Schneider et al. (2010), the water vapor budget and thermodynamic budget are closely linked. The zonally asymmetric component of both budgets is an approximate two-term balance between vertical advection of the zonal-mean potential temperature or saturation specific humidity by the zonally asymmetric velocity and the zonally asymmetric precipitation.

Held and Soden (2006) suggested that the free-tropospheric saturation specific humidity in scaling estimates for the upward mass flux is negligible or, as in Betts and Ridgway (1989) and Betts (1998), it is linearly related to the boundary layer saturation specific humidity $\overline{[q_{sb}]}$. In equation (2.13), $\Delta_v q_s \sim \overline{[q_{sb}]}$ leads to the scaling estimate

$$-\frac{\overline{\omega^*}}{g} \sim -\frac{\overline{\omega^{\uparrow *}}}{g} \sim \frac{\overline{P^*}}{\overline{[q_{sb}]}}, \tag{2.15}$$

Schneider et al. (2010) argued that the free-tropospheric contribution is not generally negligible—that is, an actual difference in saturation specific humidity must be considered in (2.13). Physically, this can occur as the result of the amplification of warming aloft for moist adiabatic stratification. However, the amplification of temperature increases at fixed pressure levels can be offset by increases in the pressure depth of the mass fluxes, as occur with a rising tropopause. A concrete example of

offsetting changes in stratification and pressure depth is given by the "Fixed Anvil Temperature" hypothesis (Hartmann and Larson 2002), which posits that the temperature that convection reaches is approximately climate invariant. If this hypothesis holds precisely, the free-tropospheric saturation specific humidity at the tropical tropopause would also be climate invariant. Schneider et al. (2010) also showed that a scaling that includes the free-tropospheric contribution to the saturation specific humidity difference accounted better for changes in the upward component of zonal-mean tropical circulation in simulations with zonally symmetric forcing and boundary conditions.

Whether or not the free-tropospheric water vapor contributes depends on the vertical velocity profile $\Omega(p)$ that is used to separate the integrand: $\{\omega^{\uparrow}\partial_p q_s\} \approx \hat{\omega}^{\uparrow}\{\Omega(p)\partial_p q_s\}$, where $\hat{\omega}^{\uparrow}$ depends on the horizontal, but not the vertical, coordinates (e.g., Sobel 2007). This is discussed further in the appendix.

2.5.3 Assessment of scaling estimate

The left panel of Fig. 2.5 shows that the zonally asymmetric component of the pressure velocity in the ascent region scales with the zonally asymmetric component of the upward pressure velocity: $\overline{\omega^*} \sim \overline{\omega^{\uparrow *}}$. However, the zonally asymmetric total pressure velocity $\overline{\omega^*}$ is systematically larger (by about 30%) than $\overline{\omega^{\uparrow *}}$. The zonal-mean upward vertical velocity $\overline{[\omega^{\uparrow}]}$ is larger than the zonal-mean total vertical velocity $\overline{[\omega]}$; hence, when the zonal-mean is removed to form the zonally asymmetric component (e.g., $\overline{\omega^*} = \overline{\omega} - \overline{[\omega]}$), the total velocity $\overline{\omega^*}$ is larger than the upward velocity $\overline{\omega^{\uparrow *}}$. The fact that $\overline{\omega^*} \sim \overline{\omega^{\uparrow *}}$ suggests that if the hydrological cycle scaling estimate accounts for the changes in the upward pressure velocity, to which it is more directly related (2.10), it will also account for the changes in the total pressure velocity, i.e., the Walker circulation. However, consistent with the results of Schneider et al. (2010), the simulated changes in the zonal-mean pressure velocity $\overline{[\omega]}$ in the ascending branch of the Hadley circulation are not straightforwardly related to the changes in the upward component of the zonal-mean pressure velocity $\overline{[\omega^{\uparrow}]}$.

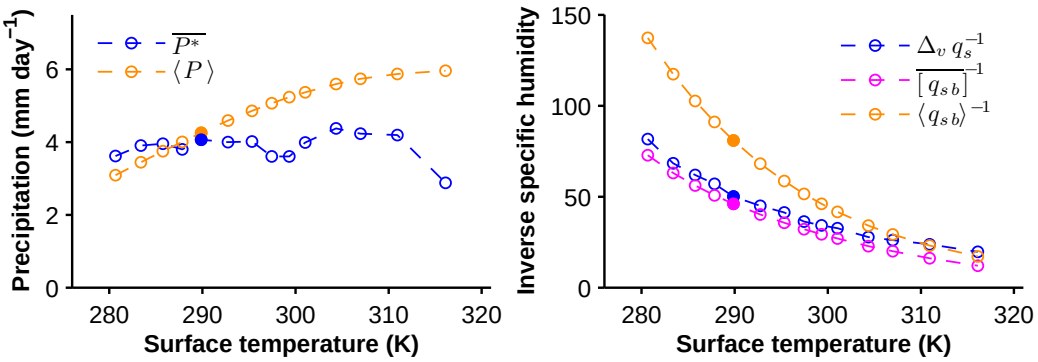

Figure 2.6. Left: precipitation vs. global-mean surface temperature for zonally asymmetric tropical-mean $\overline{P^*}$ (blue) and global-mean $\langle P \rangle$ (orange). Right: inverse specific humidity vs. global-mean surface temperature for tropical-mean $\Delta_v q_s$ (blue), tropical-mean $\overline{[q_{sb}]}$ (magenta), and global-mean $\langle q_{sb} \rangle$ (orange). The averaging conventions are the same as in Fig. 2.5.

The right panel of Fig. 2.5 shows that the hydrological cycle estimate (2.13) applied locally accounts for the changes in the Walker circulation. There are two variants of the local scaling in the right panel of Fig. 2.5: one includes the free-tropospheric saturation specific humidity contribution to $\Delta_v q_s$ (blue) and one that neglects it $\Delta_v q_s \sim \overline{[q_{sb}]}$ (magenta). The two are largely indistinguishable and both account for the simulated changes in $\overline{\omega^*}$. The scaling that neglects the free-tropospheric saturation specific humidity is an approximation, so while it appears to be more accurate in the warm limit, this is the result of compensating errors. The scaling constants, obtained by least squares, are approximately 1.5 which is consistent with the factor of 1.3 that relates $\overline{\omega^{\uparrow *}}$ and $\overline{\omega^*}$.

Figure 2.5 also shows the global-mean scaling estimate, $-g\,\langle P \rangle / \langle q_{sb} \rangle$, in orange. This is similar to the convention used in the analysis of IPCC simulations in Held and Soden (2006) and Vecchi and Soden (2007), who further approximated the saturation specific humidity changes by linearizing its dependence on temperature about the present climate (i.e., $\delta \langle q_{sb} \rangle \approx 0.07 \times \delta \langle T_s \rangle$). The global-mean scaling captures the gross magnitude of the weakening, but not the detail. It tends to underestimate the circulation changes for climates colder than the reference climate; at the reference climate, the global-mean scaling decreases by $3.1\%\,\mathrm{K}^{-1}$, compared with $\overline{\omega^*}$ which

decreases by $4.4\%\,\mathrm{K}^{-1}$.

As the local scaling convention captures the variations in the Walker circulation with climate, we can decompose it to determine the relative contributions from the precipitation changes (Fig. 2.6, left panel) and the saturation specific humidity changes (Fig. 2.6, right panel). Two factors—approximately constant $\overline{P^*}$ and rapidly decreasing $\Delta_v q_s^{-1}$ or $\overline{[q_{sb}]}^{-1}$—account for the rapid decrease in the Walker circulation with warming.

The zonally asymmetric component of tropical precipitation, $\overline{P^*}$, is approximately constant with climate; however, this is not a general result. Alternative convection scheme parameters, in particular relaxing to 90% relative humidity instead of 70%, can produce non-monotonic changes in $\overline{P^*}$ with climate. The locally averaged version of the scaling for Walker circulation changes (2.13) is similarly accurate in the alternate set of simulations. These simulations have increases in $\overline{P^*}$ and a less rapid decrease in the Walker circulation $\overline{\omega^*}$ with warming from the Earth-like reference climate than the simulations presented here. The multi-model mean of the models participating in the fourth IPCC assessment also features increased $\overline{P^*}$ with warming (Meehl et al. 2007).

Changes in local precipitation cannot be understood independently of the circulation changes as local water vapor convergence depends, in part, on the circulation changes. In the simulations presented here, the changes in the zonally asymmetric component of net precipitation in the deep tropics have a large dynamic component, i.e., a component associated with changed winds and fixed specific humidity. The dynamic changes reduce the zonally asymmetric precipitation due to weakening surface easterlies with warming and offset the thermodynamic component of the changes, i.e., the component associated with changes in specific humidity and fixed winds, which increase the zonally asymmetric precipitation with warming. This is qualitatively consistent with the multi-model mean of the fourth IPCC assessment simulations presented in Fig. 7 of Held and Soden (2006): the equatorial Pacific is a region in which the changes in net precipitation are quite different from a thermodynamic estimate that assumes fixed circulation.

The saturation specific humidity is a rapidly increasing function of temperature, so, as expected, its inverse rapidly decreases with warming. The difference between the inverse saturation specific humidity when the free-tropospheric component of $\Delta_v q_s$ is neglected and when it is retained is small. This is a consequence of the depth of the circulation—it reaches sufficiently low pressures and temperatures that q_s is negligible in that region of the free troposphere. The appendix has a more extensive discussion of the dependence of the scaling estimate on the vertical structure of the circulation and how the results of the simulations presented here relate to previous work.

Figure 2.6 also sheds light on why the global-mean convention may, in some cases, appear adequate. Global-mean precipitation $\langle P \rangle$ increases more rapidly than the zonally asymmetric component of tropical precipitation $\overline{P^*}$; global-mean surface saturation specific humidity $\langle q_{sb} \rangle$ increases more rapidly than the tropical-mean surface saturation specific humidity difference $\Delta_v q_s$. As the scaling depends on the ratio, the more rapid changes in the individual components largely cancel, but this must be regarded as fortuitous.

2.6 Conclusions

Zonal surface temperature gradients decrease rapidly as the climate warms in the idealized GCM. This can be understood by considering a simplified surface energy budget that consists of a two-term balance between the zonally asymmetric component of the Q-flux and evaporation. It leads to a scaling for the zonal difference in tropical surface temperature that depends inversely on the rate of change of saturation specific humidity (or the Clausius-Clapeyron relation), evaluated using the mean surface temperature in the tropics if the Q-flux is fixed.

The Walker circulation rapidly weakens with warming in the idealized GCM. The changes can be accounted for using locally evaluated hydrological cycle scaling estimates. The changes in the scalings can be decomposed into i) equatorial precipitation increases being approximately zonally uniform with warming and ii) rapid, Clausius-Clapeyron increases in near-surface saturation specific humidity with warming. The

global-mean version of the hydrological cycle scale estimate does not accurately account for the changes in the Walker circulation in all climates, though it does capture gross changes due to compensating changes in precipitation and saturation specific humidity that are larger than the locally averaged quantities.

That the hydrological cycle scaling estimate requires knowledge of local precipitation changes is a limitation. Ideally, one would want to understand circulation changes independently and use that result in the water vapor budget to constrain local precipitation changes. The moist static energy budget is one approach, though it has established difficulties (Sobel 2007). Another approach is that of the Lindzen-Nigam model (Lindzen and Nigam 1987), in which the surface temperature field is used to determine pressure gradients, which in combination with a linear momentum equation determine boundary layer convergence. We have solved the Lindzen-Nigam equations using the GCM simulated surface temperature fields as forcing and found that the changes the Lindzen-Nigam model predicted in the boundary layer mass flux underestimated those simulated by the GCM by roughly a factor of two over the range of climates. Devising conceptual models of how tropical circulations change with climate that adequately account for GCM simulations remains a challenge.

A limitation of this study is the prescribed and invariant Q-flux. But understanding the atmosphere-only dynamics is a necessary step toward the more realistic case that includes an interactive ocean.

2.7 Acknowledgments

We thank Simona Bordoni, Isaac Held, Yohai Kaspi, Xavier Levine, and Paul O'Gorman for helpful discussions and technical assistance. The comments of two anonymous reviewers helped clarify the presentation of our work. This work was supported by a National Defense Science and Engineering Graduate Fellowship, a National Science Foundation Graduate Research Fellowship, and a David and Lucile Packard Fellowship. The GCM simulations were performed on Caltech's Division of Geological and Planetary Sciences Dell cluster. The program code for the simulations, based on the

Flexible Modeling System of the Geophysical Fluid Dynamics Laboratory, as well as the simulation results themselves are available from the authors upon request.

2.8 Appendix A: Dependence of water vapor scaling on vertical structure

To understand why the free-tropospheric contribution to the saturation specific humidity difference is negligible, we examine the vertical structure of the vertical velocity, as $\Delta_v q_s$ is an approximation of $\{\Omega(p)\partial_p q_s\}$. Also, the vertical structure of the circulation has importance beyond the hydrological cycle scaling estimate: it determines whether moist static energy is imported or exported by overturning circulations (Sobel 2007; Back and Bretherton 2006; Peters et al. 2008). If the vertical velocity profile has larger amplitude in the free troposphere, it makes the saturation specific humidity difference less sensitive to the free-tropospheric values entering $\Delta_v q_s$ because temperature and saturation specific humidities are small there. Indeed, the vertical velocity profile is "top-heavy" in the ascending branch of the Walker circulation (solid lines in Fig. 2.7); that is, it has significant amplitude in the upper troposphere. In contrast, the zonal-mean vertical velocity profile has more amplitude near the surface and less amplitude in the upper troposphere (dashed lines in Fig. 2.7). The vertical velocity profiles of the idealized simulations are broadly consistent with the regional variations in the vertical velocity profile in Earth's tropics (Back and Bretherton 2006).

For the zonal-mean component of the simulations presented here, the hydrological cycle scaling estimate that neglects the changes in the saturation specific humidity away from the boundary layer ($\Delta_v q_s \sim \overline{[q_{sb}]}$) is distinguishable from the scaling estimate that retains the full $\Delta_v q_s$ (i.e., the representative pressure levels when the integral is discretized are closer to each other than in the zonally asymmetric case and the free-tropospheric contribution is not negligible). This is consistent with the results presented in Schneider et al. (2010).

Figure 2.7 also shows that the pressure depth over which there is significant vertical velocity amplitude increases and the tropopause pressure decreases with warming. For this reason, we vary the pressure at which the free-tropospheric contribution to $\Delta_v q_s$ is evaluated in Fig. 2.5; neglecting these changes can potentially lead to different scaling behavior.

There are two ways in which the vertical velocity profile can lead to Clausius-Clapeyron-like scaling of $\Delta_v q_s$. First, a larger pressure depth decreases the free troposphere's weight (e.g., in the limit of the whole troposphere, the tropopause saturation specific humidity is orders of magnitude smaller than that of the surface). Second, holding the pressure depth fixed and shifting it upward (e.g., the difference between 800 hPa and 300 hPa compared to the difference between 900 hPa and 400 hPa) leads to more rapid changes in the saturation specific humidity difference as the temperatures are lower and the rate of change of the saturation specific humidity is larger. These changes will appear closer to the rate given by the Clausius-Clapeyron relation if it is evaluated at a fixed level such as the surface (related issues about the sensitivity of saturation specific humidity to where it is evaluated and the possible imprecision that results are discussed in O'Gorman and Muller 2010).

In an analysis of comprehensive GCMs, Vecchi and Soden (2007) showed that changes in the global-mean upward component of the vertical velocity scaled with the hydrological cycle scaling estimate that neglects the free-tropospheric contribution to the saturation specific humidity (i.e., $\langle \omega^{\uparrow} \rangle \sim -g \langle P \rangle / \langle q_{sb} \rangle$), but the scaling overestimated the magnitude of the vertical velocity changes by about a factor of two to three. However, when Vecchi and Soden (2007) considered only upward pressure velocities exceeding $0.05\,\mathrm{Pa\,s^{-1}}$ (i.e., $\omega^{\uparrow} = \omega H(-0.05\,\mathrm{Pa\,s^{-1}} - \omega)$), the changes in the vertical velocity were larger and consistent with the scaling estimate. Changes in the vertical structure of the circulation may explain why the scaling in Fig. 5 of Vecchi and Soden (2007) improved when a non-zero threshold for upward vertical velocity was introduced: With a threshold of zero, the vertical velocity profile is less top-heavy and the changes in the free-tropospheric saturation specific humidity contribution to $\Delta_v q_s$ cannot be neglected, in which case approximating $\Delta_v q_s$ with $\overline{[q_{sb}]}$

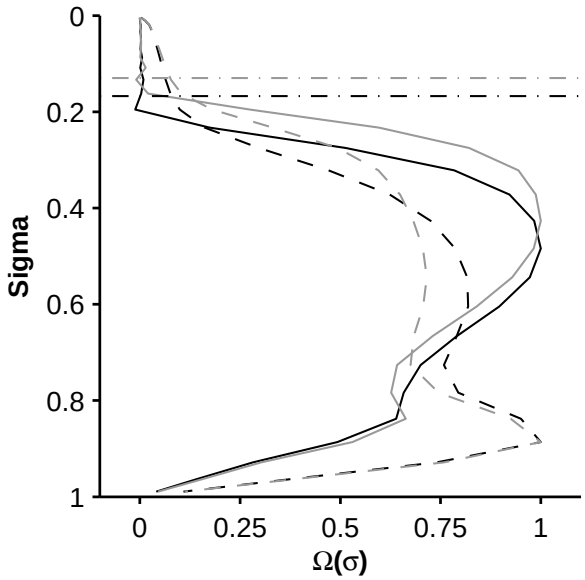

Figure 2.7. Vertical structure of vertical velocity $\Omega(\sigma) = \omega^{\uparrow}/\min(\omega^{\uparrow})$ for simulations with global-mean surface temperature $\langle T_s \rangle$ 289.9 K (black) and 295.3 K (gray). Solid lines are zonally asymmetric pressure velocity profiles $\overline{\Omega^*}$ evaluated in the ascending region (cf. Fig. 2.1) and dashed lines are zonal-mean pressure velocity profiles $\overline{[\Omega]}$. The dashed-dotted lines are the zonal-mean tropical tropopause defined by the WMO 2 K km^{-1} lapse rate criterion.

leads to an overestimate of the predicted weakening of the circulation with warming; however, for regions of strong ascent (such as those considered here), the vertical velocity profile can be sufficiently deep that the free-tropospheric contribution to $\Delta_v q_s$ is negligible, $\Delta_v q_s$ scales similarly to $\overline{[q_{sb}]}$, and the circulation weakens rapidly with warming. Another factor is that Vecchi and Soden (2007) changed from a threshold of 0 Pa s^{-1}, which includes extratropical regions of ascending motion, to a threshold of 0.05 Pa s^{-1}, which limits the area considered to a few, strongly ascending tropical locations, while using global-mean precipitation and surface specific humidity in both cases. The utility of global-mean scaling estimates for local circulation changes is assessed in Fig. 2.5 and Fig. 2.6, which show that they do not generally account for the simulation results. Because changing the threshold changes both the geographic area under consideration and vertical structure, it is unclear which is more important.

2.9 Appendix B: Lindzen-Nigam model results

The zonal asymmetries in surface temperature and the overturning circulation in the GCM simulations both change with climate at a rate that is similar to that given by the inverse Clausius-Clapeyron relation. How are these aspects of the climate related and is there a direct connection between their changes? To answer this, we use the Lindzen-Nigam (LN) model that relates surface winds to surface temperatures (Lindzen and Nigam 1987).

Lindzen and Nigam (1987) proposed a model for the zonally asymmetric component of the tropical surface winds. This model assumes that pressure gradients can be related to surface temperature gradients and uses linear horizontal momentum equations. The height of the surface layer in the model is determined from a balance between the convergence of the horizontal winds and a linear damping term; physically, the damping term represents the finite time over which convection vents mass out of the boundary layer (Sobel 2007, and references therein). The Walker circulation (or the component of it that is forced by surface temperature gradients) is then, by continuity, the vertically integrated surface-layer convergence. Sobel (2007) reviews the Lindzen-Nigam model, its relation to the Gill model, and provides an observational assessment of these simple models.

We will compare results from the LN model to the GCM, while acknowledging that surface-forced convergence is not a complete description of the tropical circulation. For example, Sobel and Neelin (2006) and Back and Bretherton (2009) discuss how the surface-forced and deep circulations interact.

2.9.1 Model equations

We use a simplified form of the Lindzen-Nigam model following Neelin (1989):[3]

$$\epsilon_m \overline{u^*} - f\overline{v^*} + g\partial_x h = C\,\partial_x \overline{T_s^*}; \tag{2.16}$$

$$\epsilon_m \overline{v^*} + f\overline{u^*} + g\partial_y h = C\,\partial_y \overline{T_s^*}; \tag{2.17}$$

$$\epsilon_T h + H_0(\partial_x \overline{u^*} + \partial_y \overline{v^*}) = 0, \tag{2.18}$$

where the horizontal velocities ($\overline{u^*}$ and $\overline{v^*}$) are mass-weighted vertical averages in the boundary layer, h is the perturbation height of the boundary layer, H_0 is the mean height of the boundary layer, ϵ_m is the momentum damping coefficient, and ϵ_T is the thermal damping coefficient. The dimensional constant $C = gH_0/2T_0$ relates temperature gradients to geopotential gradients. We use the parameter values $H_0 = 3\,\mathrm{km}$, $T_0 = 280\,\mathrm{K}$, $\epsilon_m = (2\,\mathrm{days})^{-1}$, and $\epsilon_T = (0.5\,\mathrm{days})^{-1}$ following Lindzen and Nigam (1987).

The model equations are discretized by Fourier transforming in the periodic x-dimension and finite differences in the y-dimension. The domain is an equatorial β-plane that extends to the poles. The GCM-simulated time-mean surface temperature field is used for the right-hand side of eqns. 2.16 and 2.17, and the derivatives are computed in the same way as the other terms in the system of equations.

2.9.2 Model results

Figure 2.8 shows the vertical velocity in the ascending branch of the Walker circulation over the range of climates in the GCM simulations and the LN model solutions. As the LN model determines the mass-weighted vertically integrated horizontal winds, the divergence is the vertical velocity at the top of the boundary layer: $\partial_x \overline{u^*} + \partial_y \overline{v^*} = \overline{\omega^*}(z = H_0)$. We compare this to the GCM-simulated vertical velocities at fixed σ-level, and ignore the difference that arises because of the differences in coordinates.

As in the GCM simulations, the LN model has a decreasing vertical velocities

[3]Results using the set of equations in Lindzen and Nigam (1987) are similar.

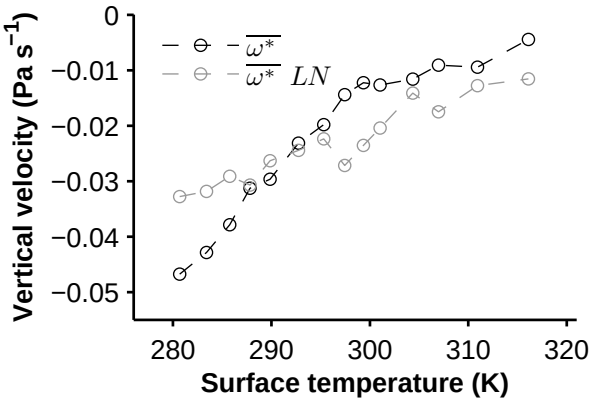

Figure 2.8. GCM simulated $\overline{\omega^*}$ (black) and Lindzen-Nigam model $\overline{\omega^*}$ (gray). GCM results are evaluated at $\sigma = 0.73$, in contrast to the flow-dependent σ-level convention used in Fig. 2.5.

with warming. However, the LN model underestimates the reduction in the Walker circulation. Over the range of climates, LN model estimates decreases of a factor of $\sim$3 whereas the GCM simulated changes by $\sim$6.

There are several possible factors that may cause the LN model to underestimate the Walker circulation changes—even while both the surface temperature that enters the LN model and GCM-simulated Walker circulation decrease with warming following the inverse of the Clausius-Clapeyron relation (see the estimates eqn. 2.8 and eqn. 2.15, respectively).

An important factor why the LN model underestimates the Walker circulation changes is that the temperature that enters the LN model is different from that entering the saturation specific humidity for the Walker circulation scaling estimate (2.15). The LN model uses the surface temperature, while the temperature at the lifting condensation level is what enters (2.15). As the surface temperature is larger than that at the LCL, this will lead to a less rapid rate of change with temperature (cf. Appendix A).

Another potential factor is that the meridional temperature gradient enters the LN model formulation, while Fig. 2.2 and the estimate (2.8) solely concern the zonal temperature contrast, which decreases like the inverse of the Clausius-Clapeyron relation. The inclusion of the meridional temperature gradients and their changes in

the LN model are not quantitatively important: the LN model results are similar if the right-hand side of eqn. 2.17 is explicitly set to zero.

Allowing T_0 in the LN model to change with the mean tropical temperatures will not resolve the discrepancy as they change by ∼15% over the range of climates, and the resulting change in the LN-model simulated $\overline{\omega^*}$ will have similar magnitude, as the equations are linear.

2.10 Appendix C: Moist static energy budget

This appendix offers a qualitative discussion of the implications of the moist static energy (MSE) budget on the Walker circulation. The MSE budget is the foundation of some conceptual models of the the tropical atmosphere (Neelin 1997; Sobel 2003; Peters and Bretherton 2005). Analyzing the moist static energy budget in the GCM simulations to quantitatively assess the importance of the different terms and their role in determining circulation changes is left for future work.

The MSE budget, neglecting transient eddies and horizontal advection is

$$\left\{\overline{\omega \partial_p h}\right\} \approx \left\{\overline{Q_{rad}}\right\} + \overline{LE} + \overline{H}, \tag{2.19}$$

where $h = c_p T + gz + Lq$ is the moist static energy, Q_{rad} is the radiative tendency, and H is the sensible surface flux.

The zonally asymmetric component of the MSE budget is

$$\overline{\omega^*}\partial_p\overline{[h]} + \overline{[\omega]}\partial_p\overline{h^*} + \overline{\omega^*}\partial_p\overline{h^*} - \left[\overline{\omega^*}\partial_p\overline{h^*}\right] \approx \left\{\overline{Q^*_{rad}}\right\} + \overline{E^*} + \overline{H^*}. \tag{2.20}$$

This can be re-arranged to solve for $\overline{\omega^*}$

$$\overline{\omega^*} \approx \frac{\left\{\overline{Q^*_{rad}}\right\} + \overline{LE^*} + \overline{H^*} - \overline{[\omega]}\partial_p\overline{h^*} + \left[\overline{\omega^*}\partial_p\overline{h^*}\right]}{\partial_p\overline{h}}. \tag{2.21}$$

Note that the denominator includes both the zonal-mean and zonally asymmetric moist static energy $\partial_p\overline{h} = \partial_p\overline{[h]} + \partial_p\overline{h^*}$.

Consider the implications of eqn. 2.21 with certain approximations:

- i) $\left\{\overline{Q^*_{rad}}\right\}$ is generally small as a consequence of the weak temperature gradients of the tropical free trosphere (Sobel et al. 2001).

- ii) $\overline{LE^*} \sim \overline{\nabla \cdot F_1}$ and so is climate invariant if F_1 is prescribed, as in our simulations.

- If $\overline{[\omega]}\partial_p\overline{h^*}$ and $\left[\overline{\omega^*}\partial_p\overline{h^*}\right]$ can be neglected, then $\overline{\omega^*}$ can only change due to changes in the term $\partial_p\overline{h}$ that is the denominator of eqn. 2.21, assuming i) and ii) hold

- The change in $\partial_p\overline{h}$ may be dominated by $\partial_p\overline{h^*}$ as the Hadley cell gross moist stability, $\partial_p\overline{[h]}$, does not change substantially with climate and may decrease in the warmest climates (Held and Hoskins 1985; Levine and Schneider 2011).

- The change in $\partial_p\overline{h^*}$ will be dominated by the change in $\overline{q^*}$ as a consequence of weak temperature gradients. The zonally asymmetric specific humidity, $\overline{q^*}$, in turn, may be approximated as $\overline{q^*} \approx \overline{[q_s]}\,\overline{\mathcal{H}^*}$. In the ascending branch, $\mathcal{H}$ is close to saturation and is determined by the $\mathcal{H}$ that the Betts-Miller scheme relaxes toward in our simulations. In the descending branch, $\mathcal{H}$ depends on the strength of the large-scale descent and on convective processes (Couhert et al. 2010).

Thus, using the MSE budget to determine the strength of the Walker circulation leads to an implicit equation, as the right-hand side of eqn. 2.21 depends on the left-hand side through the dependence of the relative humidity $\mathcal{H}$ on $\overline{\omega^*}$. For this to be a predictive estimate for the Walker circulation strength, there must be a clear relationship between the relative humidity $\mathcal{H}$ of the descending branch and the strength of the circulation.

Chapter 3

Response of tropical climate to orbital forcing. Part I: aquaplanets

This chapter is a joint work with Tapio Schneider, Simona Bordoni, and Ian Eisenman.

3.1 Introduction

Secular changes in Earth's orbit affect the seasonal and meridional distribution of incoming solar radiation. The changes affect the surface climate and the general circulations of the atmosphere and ocean. There is extensive geological evidence of such orbitally forced climate changes.

One striking record of past climate that shows the influence of orbital forcing is the stable oxygen isotopes preserved in subtropical speleothems. The perihelion, the point in Earth's elliptical orbit when it is closest to the Sun, precesses with a $\sim$20 kyr timescale. Stalagmites are more depleted of heavy oxygen isotopes when the perihelion occurs in the summer over the last 200 kyr (Wang et al. 2008). However, it is unclear what the source of the oxygen isotope variations are, as the naïve estimate in which the modern climate relationship between the isotopic composition of precipitation and the amount of precipitation is extrapolated suggests implausibly large ($> 50\%$) changes in precipitation (Dayem et al. 2010). Simulations with isotope-enabled GCMs show that nonlocal influences on the isotopic composition of precipitation are important (Legrande and Schmidt 2009; Pausata et al. 2011).

Beyond the speleothem record, atmospheric methane preserved in ice cores has

variations on precessional timescales that may be related to the tropical hydrological cycle (e.g., Schmidt et al. 2004, and references therein). Also, the African Sahara is thought to have been substantially wetter earlier in the Holocene when the perihelion was closer to northern hemisphere summer solstice than it is at present (deMenocal et al. 2000).

A central goal of this work is to constrain the magnitude of possible changes in annual-mean tropical precipitation in response to orbital precession. Our approach is to use an idealized atmospheric general circulation (GCM) model and analyze the changes that occur in the statistical steady-states of simulations with orbital parameters and associated changes in top-of-atmosphere insolation that are representative of those experienced by Earth in its history. In particular, we closely examine the changes in climate forced by changes in the time of year when the perihelion occurs (orbital precession).

The changes in water vapor convergence and net precipitation are examined to determine the extent to which they are thermodynamic (i.e., dominated by changes in water vapor concentration with fixed circulation) or dynamic (i.e., dominated by changes in circulation with fixed water vapor concentration). The angular momentum and energy balance of the atmosphere are considered to illuminate the factors affecting the strength of the circulation and the dynamic component of net precipitation.

The conventional picture of the monsoons as a land–sea breeze circulation driven by warmer surface temperatures over land (e.g., Webster and Fasullo 2003) suggests that larger summer insolation leads to stronger monsoonal circulations (chapter 8 Ruddiman 2008). While this idea about monsoons has been called into question (Bordoni and Schneider 2008), an early GCM simulation with fixed sea-surface temperature and interactive land-surface temperature met the expectation of increasing circulation strength in the Asian monsoon region when the perihelion is in northern hemisphere summer (Kutzbach 1981). GCM experiments with energetically consistent surface boundary conditions over land and ocean have found both strengthening and weakening of the cross-equatorial Hadley circulation in northern hemisphere summer in response to orbital precession (Khon et al. 2010; Clement et al. 2004, respec-

tively). Our examination of tropical circulations allows us to determine the factors that control the circulation strength and understand the conditions under which larger summer insolation does or does not lead to stronger monsoonal circulations.

In this chapter, simulations with aquaplanet boundary conditions are analyzed. In the next chapter, we analyze the role that land surface properties, and their differences with ocean surface, play in modifying these results.

3.2 Idealized GCM

3.2.1 Model description

We use an idealized moist atmospheric GCM based on GFDL's FMS spectral dynamical core and radiation scheme of GFDL's comprehensive climate model, AM2 (Anderson et al. 2004). We briefly describe the GCM's representations of physical processes, which follows the work of Frierson (2007), O'Gorman and Schneider (2008b), and Bordoni and Schneider (2008) except for the radiation scheme.

The GCM's active hydrological cycle solely models the vapor-liquid phase transition, with a constant latent heat of vaporization. Precipitation occurs when resolved motion leads to supersaturation and in parameterized convection. A simplified Betts-Miller convection scheme relaxes convectively unstable columns to a moist pseudoadiabat with constant (70%) relative humidity over a constant timescale (Frierson 2007). When precipitation occurs, it is assumed to immediately return to the surface, so there is no liquid water in the atmosphere.

The spectral dynamical core integrates the primitive equations with T42 horizontal resolution and 30 vertical levels. In addition to ∇^8 hyperviscosity throughout the atmosphere, there is ∇^2 viscosity with coefficient $4.0 \times 10^6\,\mathrm{m\,s^{-2}}$ that acts on the zonal and meridional winds in the highest model level. The GCM's leapfrog timestep is 900 s. Averages are taken over the last 20 years following a spinup period of 10 years from an isothermal, resting initial condition or one from a simulation with similar parameters.

The ocean energy flux divergence plays an important role in determining aspects of the tropical circulation (Held 2001; Herweijer et al. 2005; Levine and Schneider 2011). Therefore, we prescribe a zonally symmetric ocean energy flux divergence ("Q-flux", shown in Fig. 4.2) that is time-independent and similar to the zonal mean of estimates based on reanalyses (Bordoni 2007; Bordoni and Schneider 2008). The surface heat capacity is that of 5 m of water except where noted, and the surface albedo is 0.1 uniformly.

We focus on simulations with low thermal inertia as this permits convergence zones to migrate poleward to latitudes similar to the Asian monsoon (Bordoni and Schneider 2008). In addition, the low thermal inertia reduces the magnitude of energy storage, so aspects of the climate are close to being in equilibrium with the instantaneous insolation. Last, it is useful to have somewhat exaggerated changes to clearly isolate them.

The radiative transfer is the most significant departure from previous work and is described next.

3.2.2 Radiative transfer

Previous work with similar idealized GCMs has employed gray radiation with prescribed, latitude-dependent optical depths. This approach has limitations; for example, in the case of tidally locked exoplanets, this is inappropriate as it ignores important water vapor variations in longitude (Merlis and Schneider 2010). Here, our concern is that the seasonal cycle has reduced amplitude if there is no water vapor feedback, so we employ the comprehensive radiation scheme described in Anderson et al. (2004).

Adding a comprehensive treatment of radiative transfer necessitates including clouds in some fashion, as the meridional structure of cloud properties and the associated radiative forcing determines, in part, the meridional temperature gradient. In the extratropics, clouds have a net cooling effect, while in low latitudes there is little net warming or cooling (e.g., Hartmann 1994). Therefore, without the cloud

radiative forcing, the equator-to-pole temperature difference would be reduced.

The approach taken here is to prescribe time-independent low clouds and to neglect the ice-phase clouds of the upper troposphere.[1] The model does not simulate liquid water, so the prescribed cloud liquid water field only enters the model formulation in the radiative transfer calculation.

The vertical structure of the cloud liquid water is given by a half-sine function over the lowest quarter of the atmosphere:

$$\ell(\sigma) = \begin{cases} \ell_0 \times 2\pi \sin(-4\pi\sigma) & \text{if } \sigma > 0.75; \\ 0 & \text{otherwise.} \end{cases} \tag{3.1}$$

The vertical structure is inspired by observations (cf. Fig. 4a of Li et al. 2008) but is highly idealized. The normalization factor, 2π, is included so that the mass-weighted vertical integral of cloud water over the atmosphere takes the value of ℓ_0. Satellite observations suggest cloud water varies from $\sim 0.01\,\mathrm{kg\,m^{-2}}$ in low latitudes to $\sim 0.1\,\mathrm{kg\,m^{-2}}$ in high latitudes (Li et al. 2008). We use $\ell_0 = 0.1 \times 10^{-5}$, which corresponds to $0.01\,\mathrm{kg\,m^{-2}}$ at all latitudes. This is a smaller value in high latitudes than the observational estimate, which is chosen to keep the global mean temperature Earth-like, as neglecting clouds higher in the atmosphere can raise the emission temperature of the planet.

The cloud fraction, f, is vertically uniform in the atmosphere,[2] but varies meridionally as

$$f(\phi) = f_{eq} + (f_p - f_{eq}) \sin^2\phi. \tag{3.2}$$

We use $f_{eq} = 0.02$ and $f_p = 0.4$.

The solar constant is $1365\,\mathrm{W\,m^{-2}}$. The only greenhouse gas is CO_2 with a concentration of 300 ppm in the simulations. No ozone, aerosol, or other greenhouse gases are included in the radiative transfer calculation.

[1] Low clouds in polar regions where the air temperature is below the freezing point of water are still assumed to be in the liquid water phase.

[2] Cloud fraction has no effect on the radiative transfer where cloud liquid water and ice water is zero.

3.2.3 Insolation changes

The orbital eccentricity—defined as the difference of the semi-major and semi-minor axes over their sum—of Earth leads to a seasonal cycle associated with the changing Earth–Sun distance r; this seasonal cycle is weaker than that associated with obliquity. The perihelion precesses over a $\sim$20 kyr period, so the seasonal cycle in top-of-atmosphere insolation varies on these timescales. The annual-mean insolation at a given latitude is unchanged, on the other hand. This is a consequence of canceling factors of the square of the Earth–Sun distance r^2 in the conservation of angular momentum (Earth moves faster through the orbit when it is closer to the Sun) and the radiative flux reaching Earth, which depends inversely on r^2.

Note that climate statistics that are linear in insolation will not change in the annual-mean when the phase of the perihelion is varied since the annual-mean insolation does not change. If a climate statistic has annual-mean changes when the perihelion varied, a nonlinear process is operating that rectifies the insolation changes.

We vary the orbital configuration using a 360-day year. The specified orbital parameters are the orbital eccentricity, obliquity, and phase of perihelion.

3.2.4 Series of simulations

The standard orbital parameters we use are a near-contemporary obliquity of 23°, a relatively large eccentricity of 0.05, and perihelion occurring at southern hemisphere summer solstice, which is close to the contemporary value.

We present results from several simulations in which the phase of perihelion, orbital eccentricity, orbital obliquity, and surface heat capacity are varied.

3.3 Climate response to orbital precession

Here, we present the simulation results for the reference climate and precession-forced climate changes followed by the three balances required to understand the changes: water vapor, angular momentum, and energy. The reference climate has perihelion at

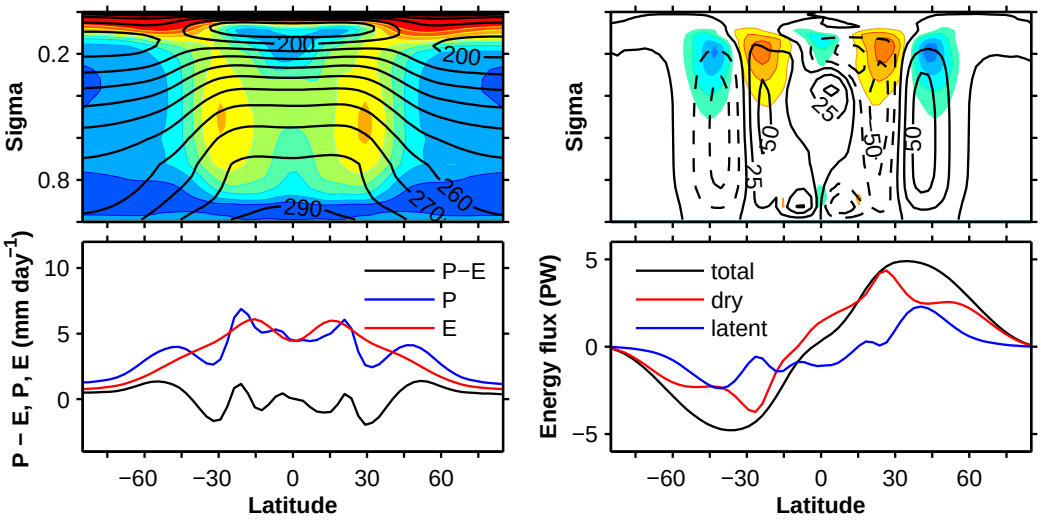

Figure 3.1. Top left: Annual- and zonal-mean temperature (black contours with contour interval 10 K) and relative humidity (colors with contour interval of 10%). Top right: Annual-mean Eulerian streamfunction (contours) with contour interval 25×10^9 kg s^{-1} and eddy (deviation from monthly mean) angular momentum flux divergence (colors) with contour interval 1.2×10^{-5} m s^{-2}. Bottom left: Annual- and zonal-mean precipitation and evaporation. Bottom right: Annual- and zonal-mean meridional moist static energy flux $\overline{vh}$ ($h = c_pT + gz + Lq$), dry static energy flux ($c_pT + gz$) and latent energy flux (Lq).

southern hemisphere summer solstice, which we refer to as December perihelion, and the perturbed climate has perihelion at northern hemisphere summer solstice, which we refer to as June perihelion.

3.3.1 Reference climate and simulated precession-forced changes

The simulated reference climate (Fig. 3.1) is broadly similar to Earth's climate (Fig. 3.2). Tropical air temperatures are close to 295 K near the surface, and the equator-to-pole surface temperature gradient is 33 K in the annual mean. The relative humidity is 80% near the surface and has subtropical minima of 30%. Consistent with the temperature field and eddy momentum flux divergence, there are sheared westerly jets in midlatitudes, with Earth-like maxima of ∼45 m s^{-1} in the upper troposphere. The annual-mean Hadley circulation is relatively weak (streamfunction maxima of ∼50 × 10^9 kg m s^{-1}). With a greater (20 m) mixed layer depth, the strength of the

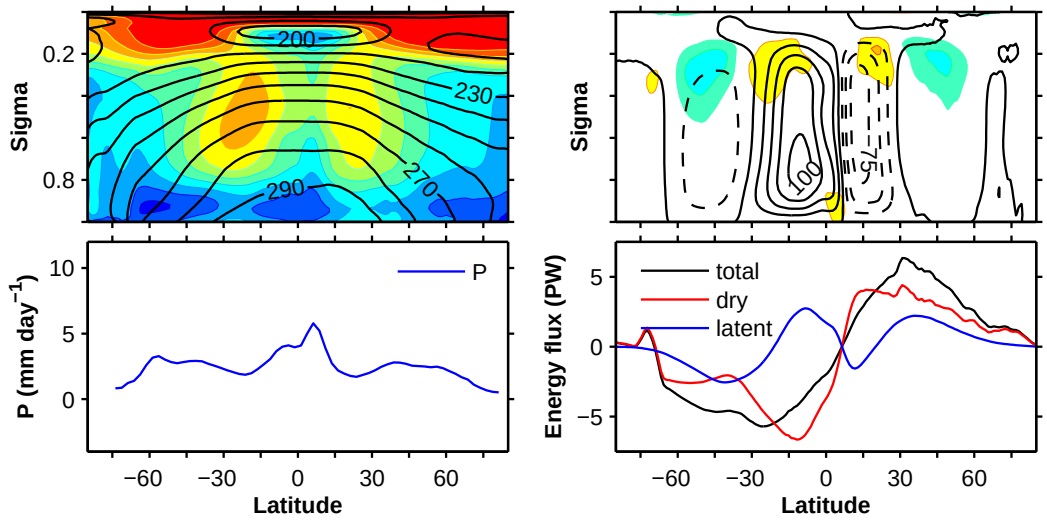

Figure 3.2. Top left: Annual- and zonal-mean temperature (black contours with contour interval 10 K) and relative humidity (colors with contour interval of 10%) from ERA-40 Reanalysis (Kållberg et al. 2004). Top right: Annual-mean Eulerian streamfunction (contours) with contour interval $25 \times 10^9\,\mathrm{kg\,s^{-1}}$ and eddy (deviation from monthly mean) angular momentum flux divergence (colors) with contour interval $1.2 \times 10^{-5}\,\mathrm{m\,s^{-2}}$ from ERA-40 Reanalysis. Bottom left: Annual- and zonal-mean precipitation from GPCP (Adler et al. 2003). Bottom right: Annual- and zonal-mean meridional moist static energy flux, dry static energy flux, and latent energy flux from ERA-40 Reanalysis. The ERA-40 Reanalysis and GPCP are averaged over the period 1981-2000.

annual-mean Hadley circulation is more similar to that of Earth's current climate (maxima of $\sim 100 \times 10^9\,\mathrm{kg\,s^{-1}}$). The evaporation has a minimum at the equator where the Q-flux offsets some of the net surface shortwave radiation and is maximum in the subtropics where the Q-flux and net surface shortwave radiation have the same sign. The precipitation is maximum off of the equator, and the latitude of the maxima is associated with the seasonal extremes of the convergence zones. In contrast, there is one precipitation maximum on Earth that is located near the equator. The spatial structure and magnitude of the meridional energy fluxes is similar to Earth: small in the tropics and increasing to maxima of ~ 5 PW in the extratropics.

Apart from the effect of limited time sampling, time-mean asymmetries between the hemispheres in the GCM simulations are a consequence of rectification of the time-dependent asymmetry in insolation. In fact, one could compare the hemispheres (i.e.,

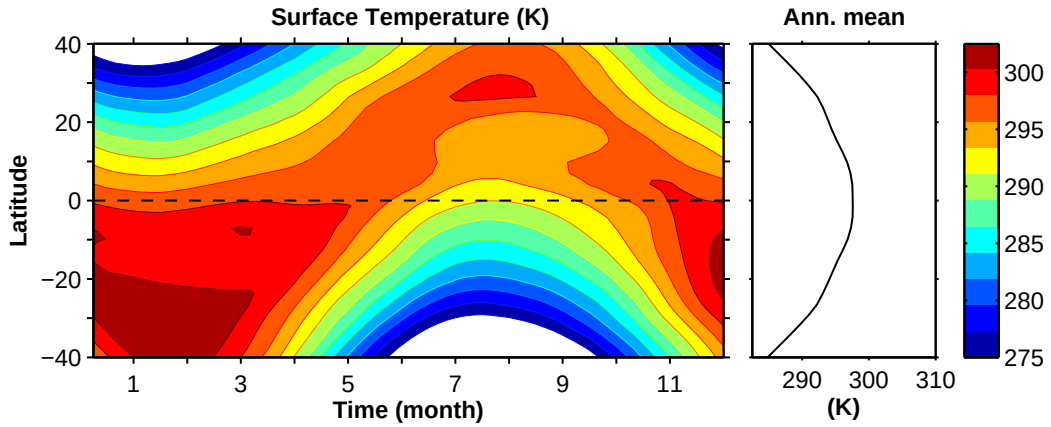

Figure 3.3. Left: Seasonal cycle of surface temperature of reference simulation with contour interval of 2.5 K. Right: Annual-mean surface temperature of reference simulation.

the degree of hemispheric asymmetry) to determine the effect of changing precession between the solstices, provided the boundary conditions and forcing are otherwise hemispherically symmetric. We do not take that approach here to maintain continuity in the presentation of results, as the next chapter has simulations with asymmetric boundary conditions.

Figure 3.3 shows the seasonal cycle of surface temperature in low latitudes for the simulation with perihelion in December. The maximum surface temperature ($\sim$300 K) occurs in the summer following perihelion with a phase lag relative to the maximum insolation of $\sim$1 month. The amplitude of the seasonal cycle increases from $\sim$5 K near the equator to $\sim$10 K at 30°. This amplitude and, therefore, the seasonal temperature gradients are exaggerated compared to Earth as a result of the low thermal inertia.

Figure 3.4 shows the seasonal cycle of precipitation in low latitudes of the reference simulation. The latitude of maximum precipitation and the intertropical convergence zone move seasonally into the summer hemisphere. The region of large precipitation is 15°–25°, as in the Asian monsoon region. Due to the low thermal inertia of the surface, the convergence zone rapidly crosses the equator; in this sense, both the monsoon onset and decay are rapid.

When the perihelion is changed to northern hemisphere summer solstice (June

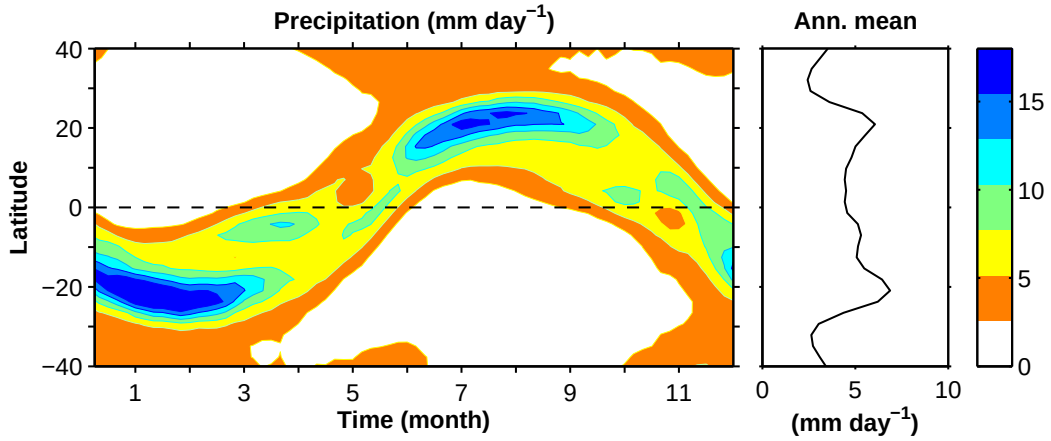

Figure 3.4. Left: Seasonal cycle of precipitation of reference simulation with contour interval of 2 mm day^{-1}. Right: Annual-mean precipitation of reference simulation.

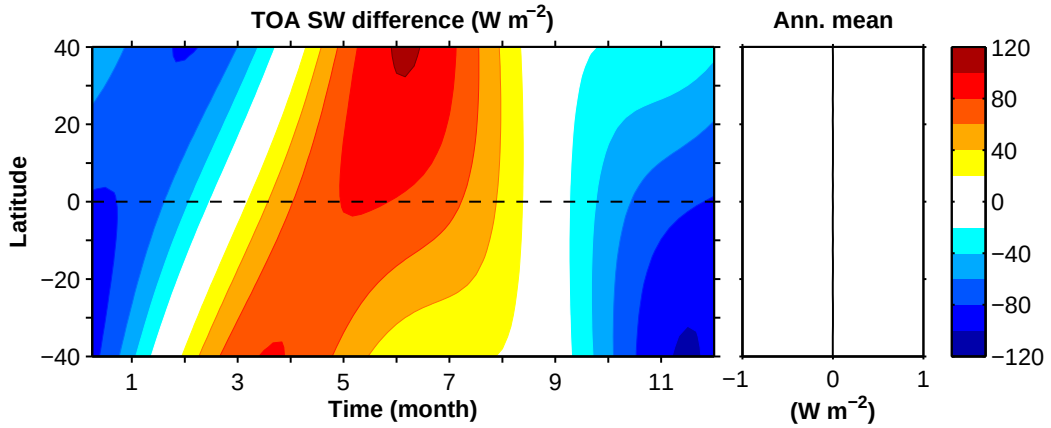

Figure 3.5. Left: Seasonal cycle of the top-of-atmosphere insolation difference between perihelion in June and December with contour interval of 20 W m^{-2}. Right: Annual-mean top-of-atmosphere insolation difference.

perihelion), the top-of-atmosphere insolation increases in the northern hemisphere summer and decreases in the southern hemisphere summer (Fig. 3.5). With eccentricity of 0.05, the instantaneous insolation changes are ∼50 W m^{-2} in the tropics. At each latitude, the annual-mean insolation does not change (right panel of Fig. 3.5).

The simulated changes in surface temperature echo the insolation changes (Fig. 3.6) with a phase lag of ∼1 month, so the summer with more insolation is warmer than the summer with less insolation. The seasonal changes average to much less than

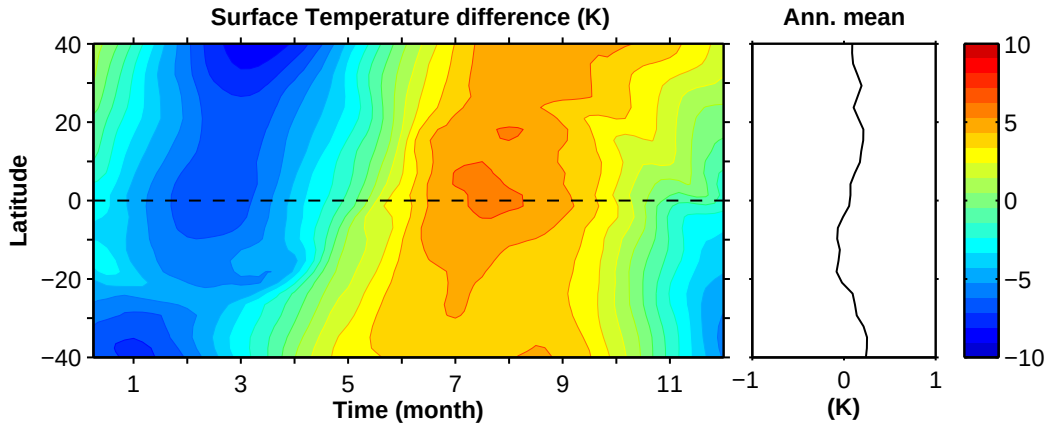

Figure 3.6. Left: Seasonal cycle of surface temperature difference between simulations with perihelion in June and December with contour interval of 1 K. Right: Annual-mean surface temperature difference.

1 K over the year; the magnitude of the rectification is $\lesssim 1\%$ if one compares the precession-forced changes in annual-mean surface temperature to the amplitude of the seasonal cycle.

The precipitation changes are phased similarly to those of the insolation and surface temperature: more precipitation occurs in the summer with perihelion. Unlike insolation and surface temperature, there are changes in annual-mean precipitation (right panel of Fig. 3.7). The annual-mean precipitation is 1 mm day^{-1} ($\sim$15%) larger in the hemisphere with perihelion coinciding with the summer solstice. In the next section, the column-integrated water vapor budget is analyzed to determine the relevant climate nonlinearity that leads to the rectification of precipitation.

In contrast to the precipitation, there is no substantial ($\lesssim 2\%$) annual-mean change in evaporation (dashed line in right panel of Fig. 3.7). This is consistent with the dominance of evaporation in the surface energy balance in low latitudes ($\delta E \sim \delta S_{\rm surf}$, due to the small Bowen ratio), so the time-dependent changes in evaporation—greater evaporation rates in the summer with greater insolation, for example—are largely averaged away in the annual mean.

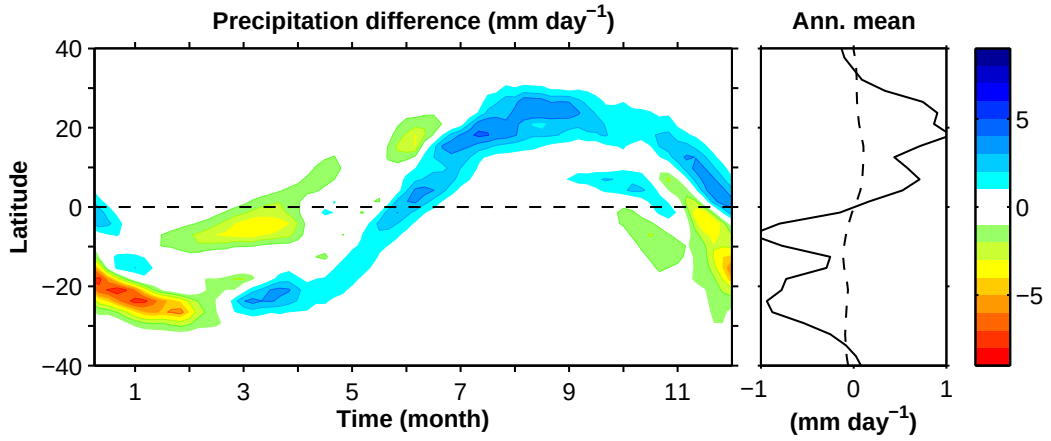

Figure 3.7. Left: Seasonal cycle of precipitation difference between simulations with perihelion in June and December with contour interval of 1 mm day^{-1}. Right: Annual-mean difference in precipitation (solid) and evaporation (dashed) between simulations with perihelion in June and December.

3.3.2 Water vapor budget

In the annual mean (denoted $[\cdot]$), the net precipitation, $[P - E]$, is balanced by the mass-weighted vertical integral ($\{\cdot\}$) of the convergence of the water vapor flux, $-\nabla \cdot [\mathbf{u}\, q]$:

$$[P - E] = -\int_0^{p_s} \nabla \cdot [\mathbf{u}\, q]\, \frac{\mathrm{d}p}{g} = -\nabla \cdot \{[\mathbf{u}\, q]\}. \tag{3.3}$$

As the annual-mean changes in evaporation are small, the changes in the water vapor convergence are balanced by the precipitation changes,

$$\delta[P] \approx -\delta\nabla \cdot \{[\mathbf{u}\, q]\}. \tag{3.4}$$

The Reynolds-averaged form of the water vapor flux, with $\overline{(\cdot)}$ defined as a monthly mean and $(\cdot)'$ indicating a deviation thereof, is $\overline{\mathbf{u}\, q} = \overline{\mathbf{u}}\, \overline{q} + \overline{\mathbf{u}' q'}$. The perturbation water vapor flux is $\delta\overline{\mathbf{u}\, q} = \delta\overline{\mathbf{u}}\, \overline{q} + \overline{\mathbf{u}}\, \delta\overline{q} + \delta\overline{\mathbf{u}}\, \delta\overline{q} + \delta\overline{\mathbf{u}' q'}$, where variables not immediately preceeded by δ are unperturbed. One can further decompose the changes in specific humidity δq, into those due to relative humidity changes $\delta\mathcal{H}$ or saturation specific humidity changes δq_s: $\delta q \approx \mathcal{H}\, \delta q_s + \delta\mathcal{H}\, q_s$, where the product of the perturbed quantities has been neglected. Also, there is a small approximation due to setting the

ratio of the specific humidity and the saturation specific humidity is set equal to the relative humidity. Combining these terms, we have

$$\delta\overline{\mathbf{u}q} = \delta\overline{\mathbf{u}}\,\overline{q} \tag{3.5}$$

$$+ \overline{\mathbf{u}}\,\mathcal{H}\,\delta\overline{q}_s \tag{3.6}$$

$$+ \overline{\mathbf{u}}\,\delta\mathcal{H}\,\overline{q}_s \tag{3.7}$$

$$+ \delta\overline{\mathbf{u}}\,\delta\overline{q} \tag{3.8}$$

$$+ \delta\overline{\mathbf{u}'q'}, \tag{3.9}$$

where the right-hand side of (3.5) is the "dynamic" component of the changes, (3.6) is the "thermodynamic" component of the changes, (3.7) is the component of specific humidity changes associated with changes in relative humidity, and (3.9) is the transient eddy component of the changes. This type of analysis has been performed for GCM simulations of climate changes forced by greenhouse gases (Held and Soden 2006) and orbital precession (Clement et al. 2004).

Figure 3.8 shows the change in the vertically integrated water vapor convergence between the simulations with perihelion in June and December. The change in water vapor convergence is positive in the northern hemisphere (net moistening) and negative in the southern hemisphere (net drying). The total changes are dominated by the thermodynamic component (3.6) of the changes. This is consistent with increased water vapor concentrations due to the increase in temperature (Fig. 3.6) associated with the greater insolation near perihelion (Fig. 3.5). The dynamic changes (3.5) offset part of the thermodynamic changes and are well-approximated by the annual-mean: $[\delta\overline{\mathbf{u}}\,\overline{q}] \approx [\delta\mathbf{u}]\,[q]$. The angular momentum and energy balance are analyzed in sections 3.3.4 and 3.3.5 to understand the factors affecting the circulation changes. The terms associated with changes in relative humidity (3.7), the product of perturbed mean fields (3.8; not shown), and transient eddies (3.9) are negligible.

The results shown in Fig. 3.8 are similar if the vertical integral in (3.3) is truncated above $\sigma = 0.73$, as expected from the small ($\sim$2 km) scale height of water vapor.

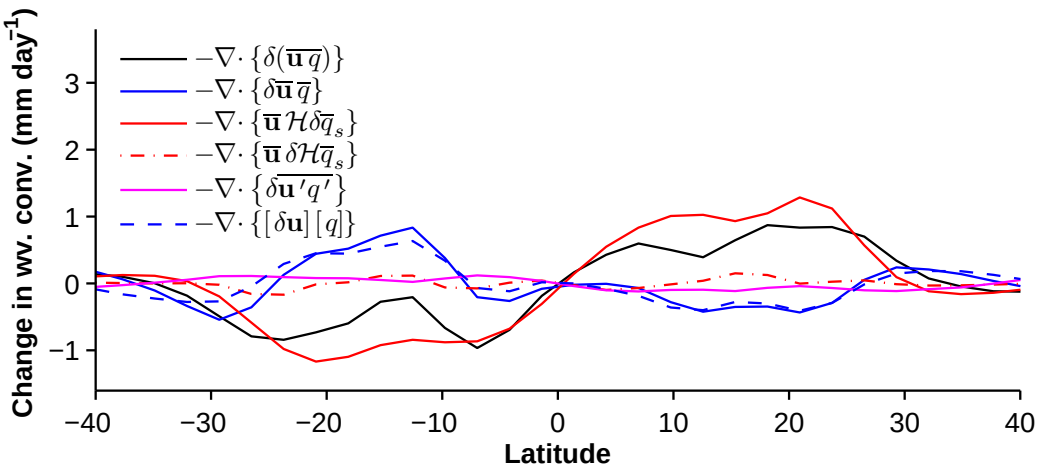

Figure 3.8. Decomposition of annual-mean difference in water vapor flux convergence between simulations with perihelion in June and December.

That the thermodynamic component is large and is associated with changes in water vapor concentration might lead to the expectation that the nonlinearity that gives rise to the annual-mean changes is that of the Clausius-Clapeyron relation. To evaluate the importance of this nonlinearity, we form a linearized thermodynamic component,

$$[\overline{\mathbf{u}}\,\mathcal{H}\,\delta\overline{q}_s] \approx \left[\overline{\mathbf{u}}\,\mathcal{H}\,\frac{\partial\overline{q}_s}{\partial\overline{T}}\delta\overline{T}\right], \tag{3.10}$$

using the monthly-mean GCM-simulated temperature field and the simplified saturation specific humidity formulation of the GCM. This linearized approximation of the thermodynamic component is quite similar to the full thermodynamic component (Fig. 3.9). Therefore, it is not the case that the nonlinearity associated with the Clausius-Clapeyron relation or the saturation specific humidity is important.

One can form a more severe linearization of the thermodynamic component and use a fractional rate of change of the saturation specific humidity with respect to temperature of $6.5\%\,\mathrm{K}^{-1}$ throughout the atmosphere. This value, $6.5\%\,\mathrm{K}^{-1}$, is the fractional rate of change of the saturation specific humidity at $T = 290\,\mathrm{K}$ and $p = 10^5\,\mathrm{Pa}$, which are representative values for the near-surface tropical atmosphere. This linearization is quite similar to both the more complete linearization and the nonlinear

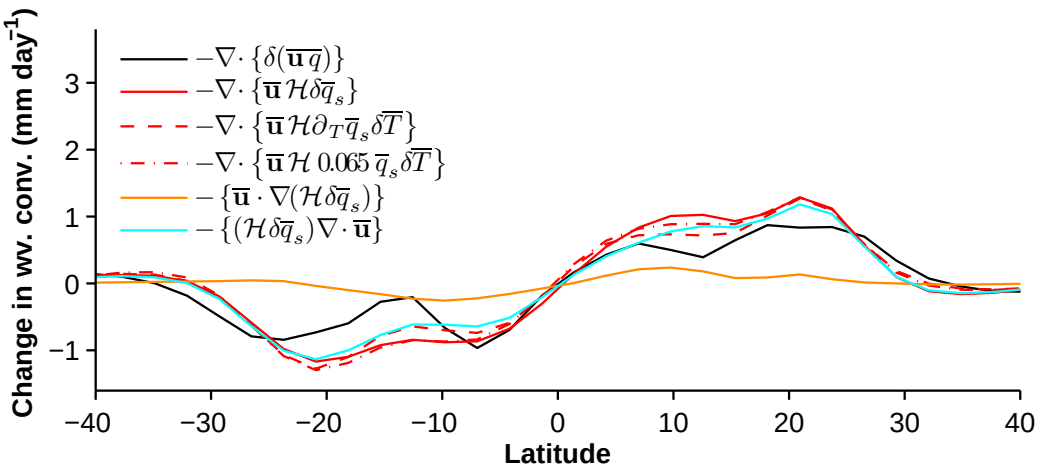

Figure 3.9. Decomposition of the thermodynamic component of annual-mean difference in water vapor flux convergence between simulations with perihelion in June and December. The red dashed line is a linearized thermodynamic component that uses the monthly mean temperature field (eqn. 3.10). The red dashed-dotted line is a linearized thermodynamic component that uses a fractional rate of change of the saturation specific humidity with respect to temperature of $6.5\%\,\mathrm{K}^{-1}$ throughout the atmosphere. The magenta and cyan curves are the two terms of the advection form of the thermodynamic component (eqn. 3.11).

thermodynamic component (the red dashed-dotted line in Fig. 3.9 compared to the red dashed and red solid lines, respectively), as expected from the dominance of the near-surface specific humidity in the vertically integrated water vapor budget.

The thermodynamic component of the water vapor flux convergence can be further decomposed into the advection of the perturbation specific humidity $-\overline{\mathbf{u}}\cdot\nabla(\mathcal{H}\delta\overline{q}_s)$ and the product of the perturbation specific humidity and the convergence of the mean wind $-(\mathcal{H}\delta\overline{q}_s)\,\nabla\cdot\overline{\mathbf{u}}$:

$$-\nabla\cdot(\overline{\mathbf{u}}\,\mathcal{H}\delta\overline{q}_s) = -\overline{\mathbf{u}}\cdot\nabla(\mathcal{H}\delta\overline{q}_s) - (\mathcal{H}\delta\overline{q}_s)\,\nabla\cdot\overline{\mathbf{u}}. \tag{3.11}$$

In the simulations, the convergence term, $-(\mathcal{H}\delta\overline{q}_s)\,\nabla\cdot\overline{\mathbf{u}}$, dominates the advection term, $-\overline{\mathbf{u}}\cdot\nabla(\mathcal{H}\delta\overline{q}_s)$ (Fig. 3.9).

Figure 3.10 shows the timeseries of the convergence of mean meridional wind and the thermodynamic change in specific humidity in the northern hemisphere lower tro-

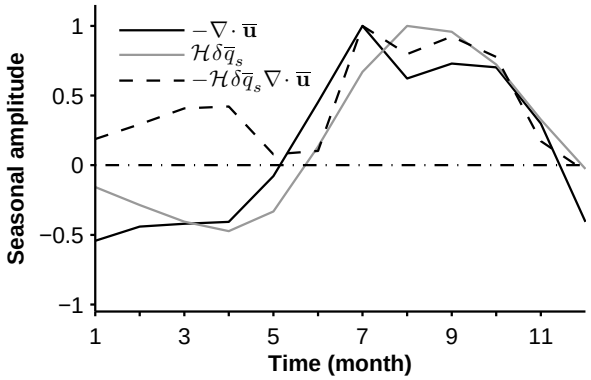

Figure 3.10. Amplitude timeseries of convergence of mean wind ($-\nabla\cdot\overline{\mathbf{u}}$, black solid line), thermodynamic change in specific humidity ($\mathcal{H}\delta\overline{q}_s$, gray solid line), and the product of the two ($-\mathcal{H}\delta\overline{q}_s\nabla\cdot\overline{\mathbf{u}}$, black dashed line) averaged over the lower troposphere (from $\sigma = 1$ to $\sigma = 0.73$) and from 5° N to 20° N. The fields have been divided by the maximum monthly mean values of $2.1\times10^{-6}\,\mathrm{s}^{-1}$ and 5.1×10^{-3}, respectively.

posphere, which largely determine the dominant, thermodynamic component in the perturbation water vapor budget (Figs. 3.9 and 3.8). The two timeseries are correlated; thus, the nonlinearity that gives rise to the annual-mean response of precipitation is the quadratic nonlinearity of the product of the unperturbed mean meridional circulation and the perturbed saturation specific humidity. Both timeseries are asymmetric, with the magnitude of the most positive values exceeding the magnitude of the most negative values.

The asymmetry in the specific humidity timeseries is due to two factors. First, the control relative humidity $\mathcal{H}$, averaged over the lower troposphere, has a seasonal cycle with larger values in summer and smaller values in winter (the opposite is true immediately above the surface). Second, the approximately exponential behavior of the saturation specific humidity with temperature leads to more positive humidities for warm perturbations than negative values for cold perturbations assuming, as in the simulations, that temperature perturbations are symmetrically distributed. The effect of the nonlinearity of the saturation specific humidity on the annual-mean water vapor convergence was evaluated in Fig. 3.9 and found not to be substantial. While it is not quantitatively important, neglecting this nonlinearity does reduce

the magnitude of the thermodynamic component of the changes shown in Fig. 3.9 slightly, which is consistent with its role in creating asymmetry in the timeseries of $\mathcal{H}\delta\overline{q}_s$ (Fig. 3.10).

The convergence of the mean meridional wind is asymmetric due to the ascending branch of the Hadley cell having smaller meridional scale than the descending branch of the Hadley cell (Fig. 3.11). The asymmetries in the timeseries determine, in part, the magnitude of the annual-mean precipitation changes, but they are not what is responsible for the fact that there are non-zero annual-mean changes: there would still be annual-mean precipitation changes if the two timeseries were sinusoids, provided the phase relationship is not changed.

The thermodynamic changes dominate the changes in annual-mean water vapor convergence, though one might have expected that the nonlinear Hadley circulation dynamics of the cross-equatorial, winter cell (Lindzen and Hou 1988; Bordoni and Schneider 2008) are an important factor in the climate response to orbital precession. Lindzen and Pan (1994), for example, suggest nonlinear Hadley cell dynamics acting on precessional timescales have important implications for glacial cycles. Hadley circulation changes and the factors affecting them are examined in sections 3.3.4 and 3.3.5 to address the reasons why they do not display the nonlinearity one might expect.

3.3.3 Implications for paleoclimate record

Here, we discuss the implications of the thermodynamic mechanism of generating annual-mean precipitation changes for the paleoclimate record. First, in addition to the speleothems from China that have oxygen isotope variations that are correlated with northern hemisphere summer insolation (e.g., Wang et al. 2008), there are speleothems from Brazil that are correlated with southern hemisphere summer insolation (Wang et al. 2006, 2007). Taken together, the records suggest that orbital precession variations have opposite phasing between the hemispheres: when the isotopic composition of calcite in the northern hemisphere is relatively depleted, such

as when perihelion is in northern hemisphere summer, the calcite in the southern hemisphere is relative enriched.

The thermodynamic mechanism that gives rise to annual-mean precipitation changes outlined above is the simplest mechanism of generating hemispherically antisymmetric precipitation changes on the timescales of orbital precession. When the perihelion is in a hemisphere's summer, the temperature and specific humidity increase. Since summer is a season with climatological convergence and ascending motion, the additional water vapor will lead to additional precipitation, if the circulation does not change. In the other hemisphere, the summer season will have less insolation and lower specific humidity, so there is less precipitation for the same magnitude of ascent.

3.3.4 Angular momentum balance

The steady angular momentum balance of the free troposphere (away from the near-surface region of friction) is[3]

$$(f+\overline{\zeta})\,\overline{v} - \overline{\omega}\frac{\partial \overline{u}}{\partial p} \approx \frac{1}{a\cos^2\phi}\frac{\partial(\cos^2\phi\,\overline{u'v'})}{\partial\phi} + \frac{\partial\overline{u'\omega'}}{\partial p}. \tag{3.12}$$

Neglecting the vertical advection of angular momentum by the mean meridional circulation, the approximate free-tropospheric balance becomes

$$(f+\overline{\zeta})\,\overline{v} = f(1-\mathrm{Ro})\,\overline{v} \approx \mathcal{S}, \tag{3.13}$$

with local Rossby number $\mathrm{Ro} = -\overline{\zeta}/f$ and eddy momentum flux divergence $\mathcal{S}$ (Walker and Schneider 2006; Schneider 2006). Consider two limits of this three-term angular momentum balance: small and large Rossby number.

When the Rossby number is small ($\mathrm{Ro} \sim 0.1$), the meridional circulation responds directly to eddy angular momentum flux divergences, $f\overline{v} \approx \mathcal{S}$, and the mean meridional circulation is slaved to the turbulent eddy stresses. This regime occurs over

[3]Formulas in the text are expressed in pressure coordinates, but the GCM simulations are analyzed in the model's σ-coordinate.

a wide range of simulated equinox Hadley circulations in dry atmospheres and in Earth's atmosphere during equinox and in the annual mean (Walker and Schneider 2006; Schneider et al. 2010; Levine and Schneider 2011). In this limit, a theory for the strength of the Hadley circulation then depends on a closure theory for the magnitude of the eddy momentum flux divergence (Walker and Schneider 2006; Schneider and Walker 2008).

When the Rossby number is large (Ro $\sim$1), the mean meridional circulation is angular momentum-conserving, as $f(1-\mathrm{Ro}) = -(a^2\cos\phi)^{-1}\partial_\phi \overline{m}$, where $\overline{m} = (\Omega a\cos\phi + \overline{u})a\cos\phi$ is the absolute angular momentum per unit mass. In this limit of the angular momentum balance, the mean meridional velocity decouples from the momentum balance and the circulation is determined by thermodynamic and radiative considerations (Held and Hou 1980; Held 2000; Schneider 2006).

The mean meridional circulation can be decomposed into components that are associated with the divergence of eddy and mean-flow momentum fluxes (Schneider and Bordoni 2008; Levine and Schneider 2011). The eddy-driven component of the streamfunction is defined by the integral of the eddy momentum flux divergence from the top of the atmosphere to pressure p,

$$\Psi_e(\phi, p) = -\frac{2\pi a\cos\phi}{fg}\int_0^p \mathcal{S}\ \mathrm{d}p' \,. \tag{3.14}$$

The mean-flow momentum flux component of the streamfunction is defined analogously:

$$\Psi_m(\phi, p) = -\frac{2\pi a\cos\phi}{fg}\int_0^p \mathcal{M}\ \mathrm{d}p' \,, \tag{3.15}$$

where $\mathcal{M}$ is the mean flow momentum flux divergence including the vertical momentum advection. With these definitions, a vertically averaged local Rossby number can be defined as

$$\langle \mathrm{Ro} \rangle = \frac{\Psi_m}{\Psi} = \frac{\Psi_m}{\Psi_m + \Psi_e}. \tag{3.16}$$

Figure 3.12 shows the seasonal cycle of the eddy and mean-flow momentum flux component of the streamfunction and the total streamfunction (left panel) and the

Rossby number (right panel) at $\phi = 15^\circ\,\mathrm{N}$. The simulated seasonal cycle of the angular momentum balance and Rossby number resembles that of Earth (e.g., Bordoni and Schneider 2008; Schneider et al. 2010), though the low-Rossby number, equinox regime is present for a vanishingly small period of time. Near the solstices, there is a strong, cross-equatorial winter Hadley cell that has large Rossby number and a weak summer Hadley cell that has small Rossby number (Fig. 3.11). The cross-equatorial circulation has large amplitude in the northern hemisphere summer, while the eddy-driven streamfunction is small ($< 50 \times 10^9\,\mathrm{kg\,s^{-1}}$ and therefore is below the contour interval) and of opposite sign, which is consistent with the eddy angular momentum convergence. The Rossby number at $15^\circ\,\mathrm{N}$ is close to one in this season, and so the strength of the mean meridional circulation is not directly determined from the angular momentum balance.

In northern hemisphere winter, the streamfunction is large and negative (i.e., it is the cross-equatorial winter cell) and the eddy-driven streamfunction is approximately half of the total streamfunction. The Rossby number is about 0.5. The subtropical eddy momentum fluxes contribute to the strength of the mean meridional circulation in the winter hemisphere subtropics (see, e.g., the southern hemisphere subtropics in Fig. 3.11), whereas they do not in the summer hemisphere.

We closely examine the July, August, and September (JAS) time-mean[4] circulation as it is the canonical northern hemisphere summer monsoon season. While Fig. 3.8 shows that the annual-mean circulation changes largely account for the dynamic changes in the water vapor budget, examining one solstice lends some insight into this as the changes in circulation near the December solstice will be similarly signed to the changes near the June solstice.[5] The Eulerian mean streamfunction averaged over JAS is shown in Figure 3.11. The cross-equatorial Hadley circulation

[4]The orbital calendar is defined with respect to the northern hemisphere autumnal equinox—i.e., the autumnal equinox occurs on September 21 for all orbital parameters. In all simulations, JAS is defined as Julian days 181–270 without shifts that would account for the changing day of the year at which, e.g., the northern hemisphere summer solstice occurs.

[5]While this may not be intuitive, it follows from symmetry considerations: if the JAS Hadley cell strengthens, for example, when the perihelion moves to that solstice, the DJF Hadley cell will weaken; as the climatological streamfunction reverses sign between the solstices, the changes (strengthening and weakening) will have the same sign.

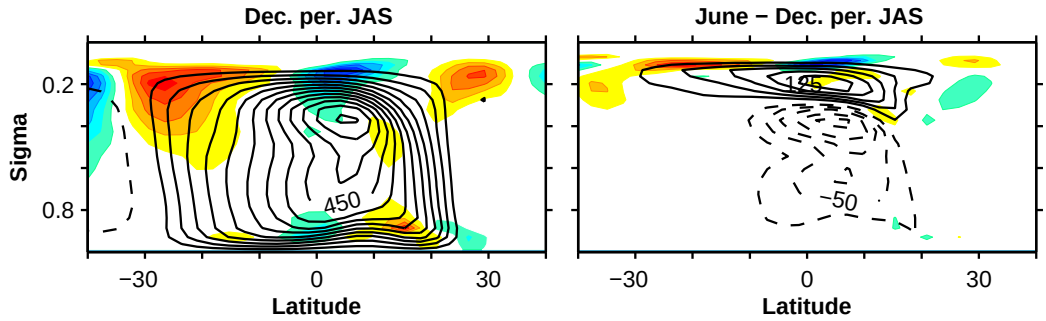

Figure 3.11. Left: JAS mean Eulerian streamfunction (contours) with contour interval $50 \times 10^9\,\mathrm{kg\,s^{-1}}$ and eddy angular momentum flux divergence (colors) with contour interval $1.2 \times 10^{-5}\,\mathrm{m\,s^{-2}}$ for simulation with perihelion in December. Right: Change in JAS mean Eulerian streamfunction (contours) with contour interval $25 \times 10^9\,\mathrm{kg\,s^{-1}}$ and eddy angular momentum flux divergence (colors) with contour interval $1.2 \times 10^{-5}\,\mathrm{m\,s^{-2}}$ between simulations with perihelion in June and December (June − December).

is strong (maximum $\sim 500 \times 10^9\,\mathrm{kg\,s^{-1}}$) compared to Earth observations (maximum value $\sim 200 \times 10^9\,\mathrm{kg\,s^{-1}}$ in the zonal mean or $\sim 350 \times 10^9\,\mathrm{kg\,s^{-1}}$ for a mean over the longitudes of the Asian monsoon, Schneider et al. 2010; Bordoni and Schneider 2008). The magnitude of the circulation is closer to observations in simulations with 20 m slab ocean depth. There is eddy momentum flux divergence in the subtropics of the winter and summer hemispheres with larger magnitude in the winter hemisphere as a result of the stronger eddy activity in winter (Fig. 3.11). Just north of the equator, there is eddy momentum flux convergence, which is likely the result of barotropic instability.

When the perihelion is in June, the Hadley circulation undergoes an upward shift, as can be seen by the pattern of negative perturbation streamfunction values in the mid-troposphere and positive perturbation streamfunction in the upper troposphere in Figure 3.11. The changes in eddy momentum fluxes also have a vertical dipole pattern with larger magnitudes near the tropopause and reduced magnitudes below. The seasonal cycle of the Rossby number does not change substantially when the perihelion is varied: in the summer hemisphere, the cross-equatorial Hadley cell is nearly angular momentum conserving; in the winter hemisphere, the cross-equatorial

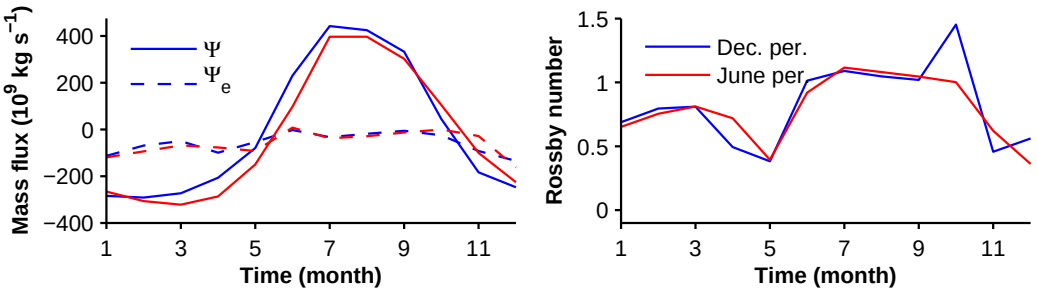

Figure 3.12. Left: seasonal cycle of the streamfunction (solid) and eddy-component of the streamfunction (dashed) evaluated on the $\sigma = 0.73$ model level at $\phi = 15°$ N for simulations with perihelion in June (red) and December (blue). Right: vertically averaged Rossby number $\langle \mathrm{Ro} \rangle$ above the $\sigma = 0.73$ model level at $\phi = 15°$ N; the Rossby number is not plotted for $\Psi < 20 \times 10^9\,\mathrm{kg\,s^{-1}}$ as it is ill-defined for near-zero values.

Hadley cell is influenced by eddies and the Rossby number is ∼0.5 (Fig. 3.12).

The Hadley circulation is *weaker* when the perihelion is in June than when it is in December; i.e., the Hadley circulation strength decreases as the insolation and insolation gradient increase. This seems to defy intuition based on the off-equatorial extension of the angular momentum conserving Hadley circulation theory (Lindzen and Hou 1988), an issue that we return to in section 3.3.5. As this result may be unexpected, it is worth noting that the comprehensive atmospheric GCM-slab ocean simulations presented in Clement et al. (2004) have similar changes in Hadley circulation strength in the lower troposphere (cf. their Figs. 5 and 10) when the perihelion is varied in a similar manner to the simulations presented here, albeit with smaller eccentricity.

3.3.5 Energy balance

The time-dependent, vertically integrated (denoted $\{\cdot\}$) energy balance of the atmosphere is

$$\left\{\frac{\partial \overline{E}}{\partial t}\right\} = -\nabla \cdot \left\{\overline{\mathbf{u}h}\right\} + S_{\mathrm{TOA}} - L_{\mathrm{TOA}} - S_{\mathrm{surf}} + L_{\mathrm{surf}} + LE + H, \tag{3.17}$$

with total atmospheric energy (neglecting kinetic energy) $E = c_v T + gz + Lq$, moist static energy h, net top-of-atmosphere shortwave radiation S_{TOA}, net top-of-atmosphere longwave radiation L_{TOA}, net surface shortwave radiation S_{surf}, net surface longwave radiation L_{surf}, latent surface enthalpy flux LE, and sensible surface enthalpy flux H. Note that moist static energy h is not a materially conserved quantity (e.g., Neelin 2007). The surface energy evolution is governed by

$$\rho_o c_{po} d \frac{\partial \overline{T}_s}{\partial t} = S_{\mathrm{surf}} - L_{\mathrm{surf}} - LE - H - \nabla \cdot F_o, \tag{3.18}$$

with water density ρ_o, water heat capacity c_{po}, mixed layer depth d, surface temperature T_s, and ocean energy flux divergence $\nabla \cdot F_o$. Summing over the surface and atmosphere, this is a three-term equation with energy storage, energy flux divergence, and radiative imbalance terms

$$\left\{ \frac{\partial \overline{E}}{\partial t} \right\} + \rho_o c_{po} d \frac{\partial \overline{T}_s}{\partial t} = S_{\mathrm{TOA}} - L_{\mathrm{TOA}} - \nabla \cdot \left\{ \overline{\mathbf{u} h} \right\} - \nabla \cdot F_o. \tag{3.19}$$

When averaged for a sufficient time that the storage terms are small, the familiar result that the ocean and atmosphere energy flux divergences balance the top-of-atmosphere radiative imbalance is obtained: $S_{\mathrm{TOA}} - L_{\mathrm{TOA}} = \nabla \cdot \left\{ \overline{\mathbf{u} h} \right\} + \nabla \cdot F_o$. Consider two limiting balances for the seasonal cycle: large and small energy storage.

If the energy storage is large, the seasonally varying net radiation can be balanced by the energy storage without changes in the energy flux divergence. In this case, the atmospheric circulation does not respond directly to balance the radiation changes, but can be perturbed indirectly by changes in the thermal properties of the surface, for example.

If the energy storage is minimal, there is a balance between the energy flux divergences and the top-of-atmosphere radiation, as in the annual mean. In this limit, assuming eddy moist static energy flux divergences are small, the ocean energy flux divergence is unchanged, and the meridional Hadley cell mass flux is confined to thin

layers near the surface and tropopause, we have

$$\partial_y(\overline{v}\,\Delta h) = S_{\mathrm{TOA}} - L_{\mathrm{TOA}}, \tag{3.20}$$

with gross moist stability (GMS) $\Delta h = \overline{h}(p = p_{\mathrm{trop}}) - \overline{h}(p = p_{\mathrm{surf}})$ (cf. Held 2000). It is clear that the energy balance does not require a particular Hadley circulation strength; the energy balance constrains the *product* of the Hadley circulation and the gross moist stability.

Kang et al. (2008) and Kang et al. (2009) developed a theory for precipitation changes in response to cross-equatorial ocean energy transport based on the atmospheric energy balance by assuming that thermodynamic changes in the water vapor budget were negligible and that the control GMS could be used in perturbed climates (i.e., GMS perturbations are negligible).[6] Figure 3.8 makes clear that thermodynamic contributions to the water vapor budget are not negligible for orbital precession. In this section, we will examine the changes in the atmospheric energy fluxes and gross moist stability to understand their role in determining the changes in the mean circulation.

Consider perturbations to equation 3.20 and neglect quadratic terms:

$$\partial_y(\delta\overline{v}\,\Delta h) = \delta S_{\mathrm{TOA}} - \delta L_{\mathrm{TOA}} - \partial_y(\overline{v}\,\delta\Delta h). \tag{3.21}$$

The perturbation energy budget shows that a change in top-of-atmosphere insolation gradient, such as a larger gradient in the summer season when the perihelion occurs near the summer solstice, can be balanced by i) a larger gradient in the top-of-atmosphere longwave radiation (though this does not generally occur because of the weakness of the tropical temperature variations), ii) an increase in the mass flux of the mean meridional circulation, or iii) an increase in the gross moist stability.

A simple estimate of the gross moist stability variations given the surface temperature and relative humidity is provided by arguments presented in Held (2001):

[6]The definition of the GMS in Kang et al. (2009) includes transient eddy moist static energy fluxes in addition to the mean flow component.

assuming the moist static energy of the upper troposphere is approximately uniform (consistent with weak temperature gradients and low specific humidities), the GMS increases with latitude away from the ascending branch of the Hadley circulation following the surface enthalpy gradient. The resulting estimate for the gross moist stability takes the form

$$\Delta h(\phi)|_{H01} = \overline{h}_s(\phi_1) - \overline{h}_s(\phi), \tag{3.22}$$

where $\overline{h}_s$ is the near-surface time- and zonal-mean moist static energy and ϕ_1 is the latitude of the ascending branch of the Hadley circulation. If this is an adequate description, the GMS of the Hadley circulation will be larger in the summer with greater insolation and insolation gradients because the meridional surface enthalpy gradient will be greater, as the increase in insolation will be balanced by surface fluxes that increase the surface temperature and specific humidity. A potential consequence is that, instead of the mass transport of the mean meridional circulation increasing to transport energy across the equator to offset the larger cross-equatorial insolation gradient, the gross moist stability increases sufficiently that the circulation changes little or can have changes of opposite sign as the insolation gradient.

Figure 3.13 shows the mean flow and transient eddy moist static energy flux in northern hemisphere summer. The mean flow component of the moist static energy flux dominates the transient eddy energy flux in the deep tropics. When the perihelion is in northern hemisphere summer, the southward, cross-equatorial mean flow energy flux increases by ∼20%, while the eddy energy flux is essentially unchanged. So, the energy fluxes by the mean meridional circulation balance the insolation changes. Next, we examine the gross moist stability and its changes to understand how the mass and energy fluxes of the Hadley circulation are related.

The simulated GMS in the summer season does change with the phase of perihelion (Fig. 3.14). When the perihelion is in June, the GMS of the northern hemisphere monsoonal Hadley cell is ∼30% larger than when it is in December. Figure 3.14 also assesses the GMS model of Held (2001) using the GCM-simulated surface moist static energy and assuming unchanged GMS in the ascending branch of the Hadley

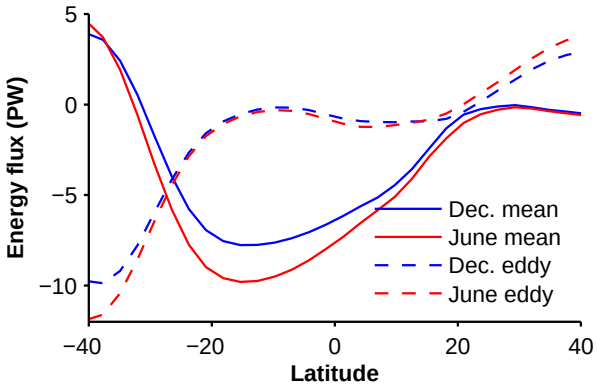

Figure 3.13. Meridional energy flux of the mean flow (solid) and transient eddies (dashed) for simulations with December perihelion (blue) and June perihelion (red).

circulation. This estimate captures the sign and magnitude of the changes in the southern hemisphere (south of ∼10° S), though there are GMS changes in the region of ascent (0° to 20° N) that are not captured by the estimate. In the ascending region, the circulation shifts upward when the perihelion is in June (Fig. 3.11), which would lead to an increase in GMS in the absence of changes to the moist static energy distribution. However, the vertical moist static energy distribution does change, and it is possible to have an upward shift of the circulation and an unchanged GMS, as approximately happens in global warming simulations (Levine and Schneider 2011). The factors determining the GMS in ascending regions is an outstanding question. The simulations results and considerations from the conceptual Held (2001) model of gross moist stability clearly illustrate that the response of the cross-equatorial circulation to increased insolation gradients is not necessarily a strengthening of the mass transport of the circulation.

The simulated atmospheric energy balance can be summarized as follows: increasing insolation gradients when the perihelion occurs in northern hemisphere summer are balanced by increased cross-equatorial energy fluxes (∼20% larger); the increased near-surface enthalpy gradient increases the gross moist stability (∼30% consistent with Held (2001) in the southern hemisphere subtropics); thus, the Hadley circulation mass flux is reduced (∼10%).

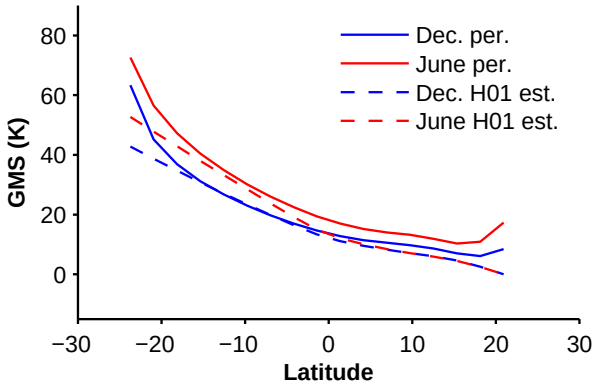

Figure 3.14. Gross moist stability $\Delta h = \{\overline{v}\,\overline{h}\}/(c_p\Psi(\sigma = 0.73))$ for simulations with December perihelion (blue solid line) and June perihelion (red solid line) averaged over July, August, and September. Held (2001) estimate for gross moist stability (see eqn. 3.22) using time-mean near-surface ($\sigma = 0.96$ model level) moist static energy of simulation with December perihelion (blue dashed line) and June perihelion (red dashed line).

3.4 Dependence on other parameters: thermal inertia, obliquity, eccentricity

3.4.1 Larger thermal inertia

When the heat capacity of the surface is that of 20 m of water, the annual-mean precipitation distribution has an equatorial peak and the seasonal excursions of the convergence zones are reduced (the maximum precipitation reaches $\sim$12° vs. $\sim$25°) compared to the simulations with low thermal inertia.

The decomposition of the changes in annual-mean, column integrated water vapor divergence between simulations with June and December perihelion is shown in Figure 3.15. The magnitude and spatial structure of the changes are reduced compared to the simulation with low thermal inertia. As before, the thermodynamic component dominates and the dynamic component offsets part of the thermodynamic changes.

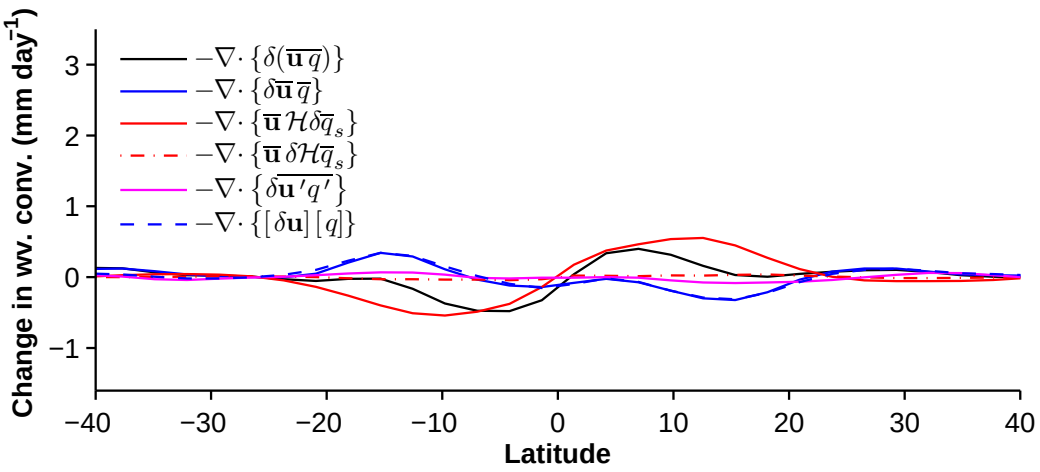

Figure 3.15. Decomposition of annual-mean difference in water vapor flux convergence between 20 m mixed layer depth simulations with perihelion in June and December.

3.4.2 Obliquity

We have varied the phase of perihelion for obliquities that are lower (20°) and higher (26°) than those of Earth's recent orbital history. Figure 3.16 shows the annual-mean precipitation and its changes over the precession shift for the three obliquities. The meridional variations in annual-mean precipitation depend on the obliquity: with lower obliquity, there is a less strong insolation seasonal cycle, the convergence zones do not undergo as large meridional displacements seasonally, and the region of large annual mean precipitation is confined closer to the equator.

The changes in climate when the perihelion is varied are similar in the climates with larger and smaller obliquity to those described for the control obliquity: i) the change in annual-mean evaporation is smaller (less rectification) than precipitation, ii) the changes water vapor flux divergence are largely thermodynamic, and iii) the dynamic component of water vapor flux divergence changes oppose the thermodynamic increases.

Thus, the magnitude of the precession-forced changes in annual-mean precipitation is similar across the range of obliquities, and the spatial structure of the changes is set by the location of convergence zones in the control climate.

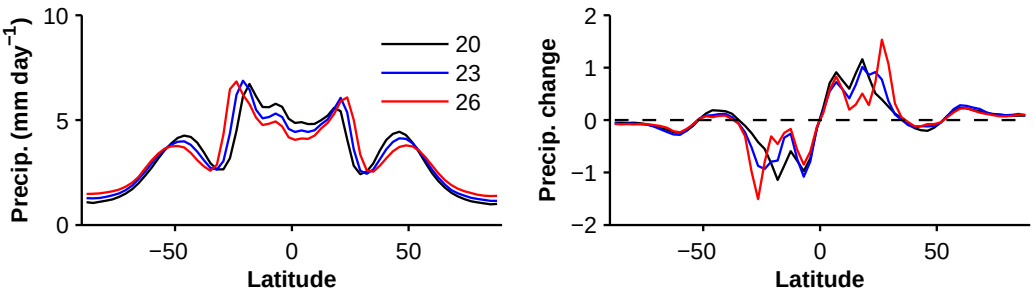

Figure 3.16. Left: Annual-mean precipitation (mm day^{-1}) for simulations with different obliquities and perihelion in December. Right: Change in annual-mean precipitation (mm day^{-1}) for simulations with different obliquities between June and December perihelion (June − Dec.).

3.4.3 Phase of perihelion

Figure 3.17 shows the results of a series of simulations in which the phase of perihelion is systematically varied.[7] When the surface has low thermal inertia, the annual-mean, northern-hemisphere tropical precipitation is maximum when the perihelion occurs at the northern hemisphere summer solstice.

When the surface has moderate thermal inertia, the seasonal cycle of the Hadley circulation mass convergence shifts ∼1 month later in the year compared to the low thermal inertia simulations. An adequate quantitative understanding of the timing of monsoon transitions is lacking as some of the factors known to affect the poleward boundaries of monsoons are flow-dependent (Chou et al. 2001; Privé and Plumb 2007a,b; Neelin 2007; Schneider and Bordoni 2008). Considering this change in isolation suggests that the thermodynamic component would be maximized for a later perihelion (e.g., 1 month after NH summer solstice). However, the response of the temperature field to the perturbed insolation also has a phase lag, and this is lag somewhat larger (∼2 months) than that of the Hadley circulation. Taken together, the changes in the seasonal cycle of the Hadley circulation and the phase lag of the temperature response to insolation lead to maximum annual-mean northern hemi-

[7] This figure is constructed by performing simulations with perihelion occurring in the half year after northern hemisphere winter solstice and before northern hemisphere summer solstice; for perihelion occurring in the other half of the year, the southern hemisphere of the appropriate simulation is plotted.

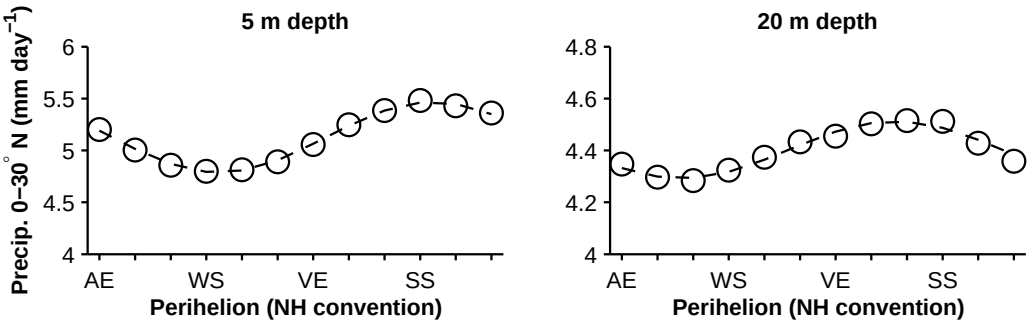

Figure 3.17. Annual-mean precipitation averaged over the northern hemisphere tropics (0–30° N) for intermediate values of perihelion (circles) and a sine fit of the simulation results (dashed line) for low (left, heat capacity of 5 m of water) and moderate (right, heat capacity of 20 m of water) surface thermal inertias.

sphere precipitation when the perihelion precedes the northern hemisphere summer solstice by ∼1 month.

One can understand these phase relationships as a consequence of the dominance of the thermodynamic component of the perturbation water vapor budget. The annual-mean precipitation will be maximum when the perturbed water vapor and the unperturbed convergence of the mean meridional wind are in phase (Fig. 3.10). With low thermal inertia, the perturbation temperature and specific humidity will not lag the perturbation insolation substantially. With Earth-like thermal inertia, the perturbation temperature will lag the perturbation insolation by ∼1–2 month.

3.4.4 Eccentricity

Here, we document the sensitivity of annual-mean precipitation and its changes with orbital precession to eccentricity variations. Figure 3.18 shows that annual-mean tropical precipitation in the summer with perihelion increases with eccentricity. Figure 3.19 shows that the changes in tropical precipitation with precession appear to be approximately linear in eccentricity. As eccentricity is doubled, the change in precipitation approximately doubles: for example, the change in precipitation is $0.7\,\mathrm{mm\,day^{-1}}$ compared to $1.4\,\mathrm{mm\,day^{-1}}$ for eccentricities of 0.05 and 0.1. This is what is expected if the thermodynamic component remains dominant and the tem-

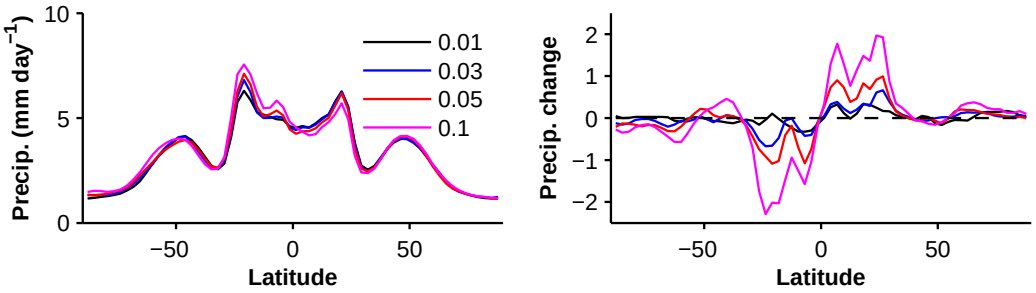

Figure 3.18. Left: Annual-mean precipitation (mm day^{-1}) for simulations with different eccentricities and perihelion in December. Right: Change in annual-mean precipitation (mm day^{-1}) for simulations with different eccentricities between June and December perihelion (June − Dec.).

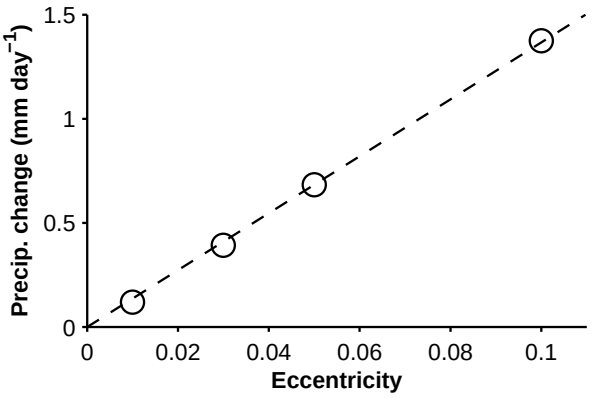

Figure 3.19. Annual-mean precipitation difference (mm day^{-1}) between simulations with June and December perihelion (June − Dec.) averaged from 0° to 30° N vs. eccentricity. The dashed line is a least squares regression of the simulation results through the origin.

perature changes remain small enough that the nonlinearity in the saturation specific humidity remains negligible: $\delta q_s \approx \partial_T q_s \, \delta T$. At sufficiently large eccentricity, the climate dynamics determining the annual-mean precipitation changes with orbital precession presented here likely change.

3.5 Time-independent insolation

Here, we present the results of simulations with time-independent insolation, e.g., fixed at 30 days after northern hemisphere vernal equinox, to confirm the result that the Hadley circulation mass flux can decrease with increasing insolation gradients. As the simulations have time-independent forcing and boundary conditions, we adopt a lower thermal inertia (of 1 m of water) and show averages of 600 days following a 800 day spinup period.

Past studies with hemispherically asymmetric forcing (such as time-independent insolation, prescribed surface temperatures, or Newtonian cooling with off-equator maxima) include Lindzen and Hou (1988), Walker and Schneider (2005), Walker and Schneider (2006), and Bordoni (2007). The essential results are that there is a transition in the regime of the angular momentum balance from small to large Rossby number (Walker and Schneider 2006) and the circulation energy fluxes increase rapidly as heating is displaced from the equator (Lindzen and Hou 1988).

Figure 3.20 shows the maximum value of the streamfunction for nine insolation distributions that span a range from northern hemisphere vernal equinox to 50 days later for June and December perihelion. The maximum top-of-atmosphere insolation occurs near 30° N for the last simulation in the series.

For near equinox insolation (from 0 to 20 days after vernal equinox), the Hadley circulation strength increases as the maximum insolation is displaced from equator. Beyond this range, the Hadley circulation strength increases weakly or decreases as the summer solstice is approached. When the change in regime occurs and the maximum streamfunction strength is reached depends on the phase of the perihelion: when the perihelion is in the northern hemisphere summer, the maximum strength is $\sim 440 \times 10^9\,\mathrm{kg\,s^{-1}}$; when the perihelion is in the southern hemisphere summer, the maximum strength is $\sim 510 \times 10^9\,\mathrm{kg\,s^{-1}}$. This confirms the result that the cross-equatorial Hadley circulation can be weaker when the insolation is stronger that we found in the time-dependent simulations.

Note that the different rate at which the Earth is moving through its orbit during

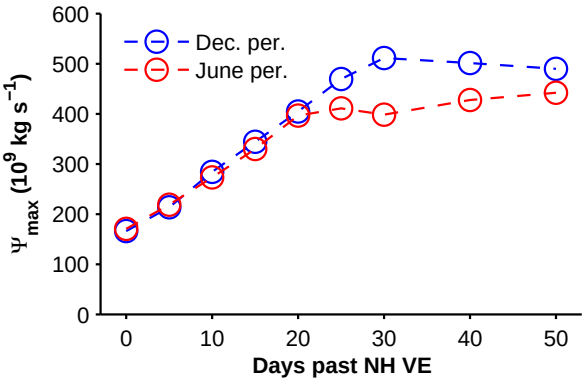

Figure 3.20. Maximum value of streamfunction on $\sigma = 0.73$ model level for simulations with time-independent insolation, expressed in days after northern hemisphere vernal equinox.

this time of the year enhances the insolation difference between the simulations with June and December perihelion. For June perihelion and 0.05 eccentricity, 50 days after vernal equinox is 34 days before the summer solstice; for December perihelion and 0.05 eccentricity, 50 days after vernal equinox is 46 days before the summer solstice. In short, the last simulation in the series is closer to northern hemisphere summer solstice in the simulation with June perihelion than the simulation with December perihelion.

3.6 Conclusions

Inspired by Earth history, we have studied the response of the tropical surface climate and atmospheric circulations to orbital precession and other changes in orbital parameters in an aquaplanet GCM. Orbital precession leads to warmer and wetter summers when the perihelion occurs near the summer solstice. The precipitation has annual-mean changes that are largely the result of thermodynamic changes: the seasonal cycle of the unperturbed mean meridional circulation and the seasonal cycle of the perturbed specific humidity are correlated, and it is this quadratic nonlinearity that rectifies the insolation changes. The magnitude of the thermodynamic component is due in part to the asymmetry in the width of the Hadley circulation's ascending

and descending branches: the convergence of the cross-equatorial Hadley circulation in the summer hemisphere is larger than the divergence in the winter hemisphere as a result of the more narrow ascent region (see Fig. 3.11, for example). Circulation changes have a smaller and opposing effect on the water vapor budget. The changes in annual-mean precipitation are not due to nonlinearities associated with the Clausius-Clapeyron relation or the off-equatorial Hadley circulation.

Interestingly, the solsticial Hadley cell defies the expectation that the strength of the mean meridional circulation increases with increasing insolation gradients. This can be understood by considering the atmospheric energy balance: insolation changes and the implied changes atmospheric energy fluxes constrain the product of the mass flux and the relevant energy contrast of the mean circulation (the gross moist stability). The changes in gross moist stability, which relates atmospheric energy and mass fluxes, are sufficiently large that the Hadley circulation mass fluxes actually decrease in the solstice seasons that coincide with the perihelion.

Last, we have examined the climate response to orbital precession over a range of orbital parameters, obliquity and eccentricity in particular, that is larger than that experienced by Earth in the last few million years. The basic climate dynamics that are fully explicated for the reference parameters hold over this range of orbital parameters. This is not to say that these arguments are generally adequate or explain the regional climate changes in Earth's history. In particular, the presence of land surfaces may modify the climate response to orbital precession—a topic explored in chapter 4.

3.7 Appendix: Response of high-latitude climate to orbital forcing

This appendix continues the analysis of the aquaplanet simulations and examines the response of high latitude climate to orbital forcing in the idealized GCM. We analyze the simulations with 20 m mixed layer depth.

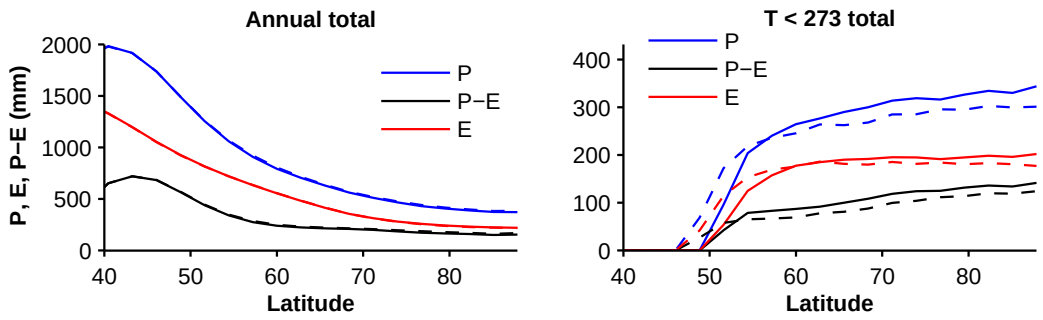

Figure 3.21. Left: annual-mean precipitation, evaporation, and precipitation minus evaporation for simulations with December perihelion (solid) and June perihelion (dashed). Right: precipitation, evaporation, and precipitation minus evaporation averaged over the times when the surface temperature is less than 273 K for simulations with December perihelion (solid) and June perihelion (dashed).

It is of interest to examine GCM simulations that include a representation of the hydrological cycle to assess the degree to which the timescales of glacial cycles are due to orbitally forced changes in ablation (e.g., Huybers 2006) or to orbitally forced changes in accumulation (e.g., Cutler et al. 2003; Raymo and Nisancioglu 2003).

3.7.1 High-latitude hydrological cycle

Figure 3.21 shows the response of the northern hemisphere extratropical hydrological cycle to precession of the perihelion. The changes in annual precipitation and evaporation are small (left panel of Fig. 3.21). The cold season precipitation, where the cold season is defined by sub-freezing surface temperature, north of 55° is larger when the perihelion is in the southern hemisphere summer (right panel of Fig. 3.21). $P - E$ conditioned on sub-freezing surface temperature is a simple estimate for the accumulation of ice on a glacier. The magnitude of the precession-forced change in cold season net precipitation is ∼20 mm near 60° N, with larger values for December perihelion than June perihelion.

Figure 3.22 shows the response of the northern hemisphere extratropical hydrological cycle to obliquity changes. North of 55°, the annual precipitation and evaporation increase when the obliquity increases (dashed above solid in left panel of Fig. 3.22)

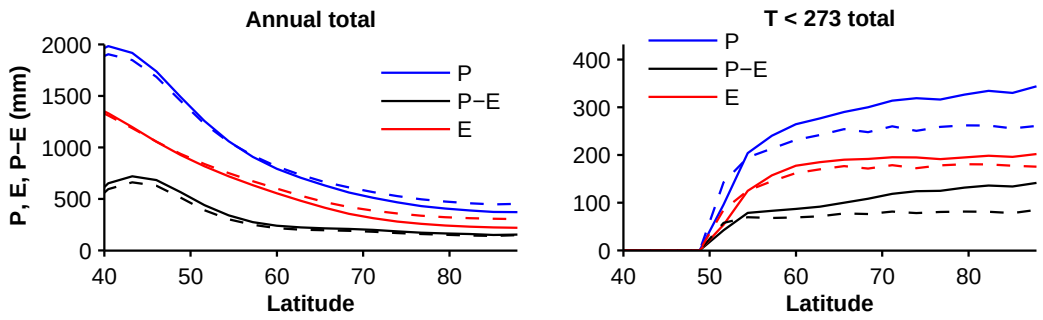

Figure 3.22. Left: annual-mean precipitation, evaporation, and precipitation minus evaporation for simulations with 23° obliquity (solid) and 26° obliquity (dashed). Right: precipitation, evaporation, and precipitation minus evaporation averaged over the times when the surface temperature is less than 273 K for simulations with 23° obliquity (solid) and 26° obliquity (dashed).

with somewhat larger increases in evaporation, so net precipitation in the extratropics is smaller with high obliquity. The cold season precipitation and net precipitation are larger when the obliquity is smaller (right panel of Fig. 3.22). The magnitude of the change in net precipitation when the temperature is freezing is ∼20 mm near 60° N, with larger changes at the pole.

Are the changes in cold season net precipitation due to having an altered cold season duration or greater rates of net precipitation during the cold season (i.e., precipitation intensity changes)? The number of days of the year with freezing surface temperatures is shown in the next section.

3.7.2 High-latitude temperature

For orbital precession, the length of the cold season does not change substantially (blue lines in Fig. 3.23). For orbital obliquity, the length of the cold season decreases as the obliquity increases from 23° to 26° (blue lines Fig. 3.24). This is approximately consistent with the lower annual-mean high-latitude insolation for smaller obliquity, though the crossover latitude for insolation and freezing days differ by ∼10°.

What do the differences in the length of the cold season imply about the average precipitation rate for the cold season (i.e., the ratio of the cold season net precipitation

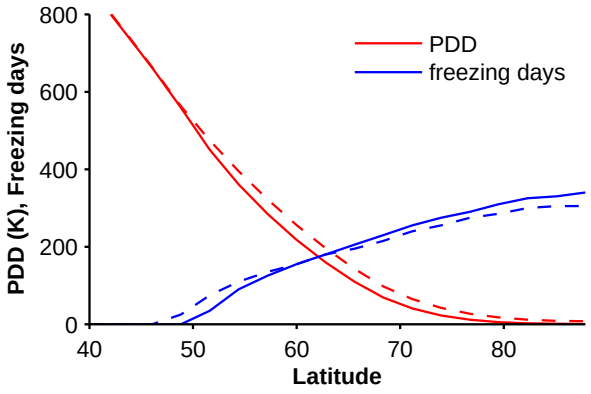

Figure 3.23. Positive degree days (red) and number of freezing days (blue) for simulations with December perihelion (solid) and June perihelion (dashed).

and number of freezing days)? For precession, the average precipitation rate for the cold season is ∼20% lower for June perihelion than for December perihelion. So, the precipitation rate rather than length of season changes dominate the changes in total winter net precipitation. For obliquity, the high obliquity precipitation rate is ∼15% lower than the standard obliquity. So, both the higher precipitation rate and longer season contribute to the larger total winter net precipitation for the standard obliquity simulation.

How do warm season temperatures change? In particular, what is the implied ablation of the simulated temperatures? The statistic positive degree days (PDD, defined as $\Sigma H(T - T_f) \times (T - T_f)$ with Heaviside step function H and freezing temperature T_f) is thought to be a reasonable proxy for ablation. Empirical relationships between ablation rate and PDD are $\sim 5\,\mathrm{mm\,K^{-1}}$ (Huybers and Molnar 2007, and references therein).

For orbital precession, PDD increases by ∼20 K when the perihelion changes from December to June (red lines in Fig. 3.23). This suggests ∼0.1 m more ablation per year when perihelion is in northern hemisphere summer.

For orbital obliquity, PDD increases by ∼100 K when the obliquity is increased from from 23° to 26° (red lines in Fig. 3.24). This suggests a change in ablation of ∼0.5 m for the increase in obliquity.

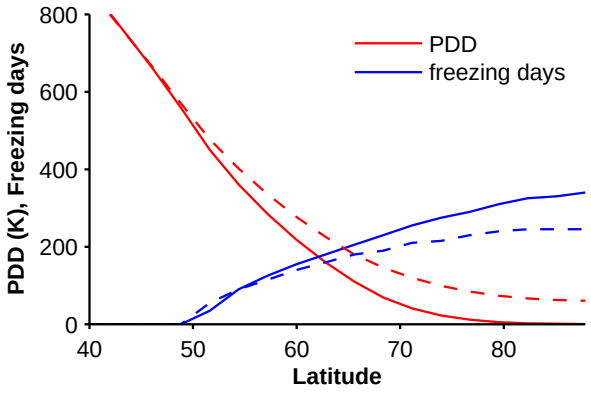

Figure 3.24. Positive degree days (red) and number of freezing days (blue) for simulations with 23° obliquity (solid) and 26° obliquity (dashed).

3.7.3 Discussion

According to the simple measures, the changes in accumulation $\sim$2 cm yr^{-1} are smaller than the changes in ablation $\sim$10–50 cm yr^{-1}.

For both sets of orbital parameter changes, the ablation and accumulation go the same direction in terms of glaciation: the high obliquity simulation has more ablation and less accumulation compared to the standard obliquity simulation; the June perihelion simulation has more ablation and less accumulation than the December perihelion simulation. This could result simply from changing season lengths, though the average precipitation rate in the cold season does change in these simulations. This anticorrelation between PDD and accumulation is similar to what Jackson and Broccoli (2003) found in simulations with a comprehensive atmospheric GCM. Their simulations had PDD changes of $\sim$300 K in Canada for the orbital variations experienced by Earth over the last 200 kyr; this is more sensitive than the simulations presented here. The simulation of Jackson and Broccoli (2003) had $\sim$20% changes in snowfall in Canada. This is a similar magnitude to our simulation results, though they are forced by larger changes in insolation as a result of the larger changes in orbital parameters.

PDD is appealingly simple, but does not properly take account of surface energy and mass balance (e.g., Rupper and Roe 2008). We have not pursued an approach

that does satisfy these balances.

Chapter 4

Response of tropical climate to orbital forcing. Part II: the role of land surfaces

This chapter is a joint work with Tapio Schneider, Simona Bordoni, and Ian Eisenman.

4.1 Introduction

In this chapter, the effect of orbital precession on tropical climate is revisited in an idealized atmospheric GCM that includes a representation of land surfaces. Building on the results of Chapter 3, we investigate how land surfaces modify the response of precipitation and the atmospheric circulation to orbital precession. Our goal is to understand simulations that bridge the gap between aquaplanet simulations (Chapter 3) and comprehensive GCM simulations (e.g., Clement et al. 2004; Kutzbach 1981). Also, it allows us to connect with the literature on monsoonal circulations that focuses on the role of the reduced heat capacity over land and its role in generating land-sea breeze circulations.

How might land surfaces affect the response of the atmospheric circulation to orbital precession? It is conceptually useful to separate ideas about the atmospheric circulation into those based on surface considerations and those based on top-of-atmosphere energy balance considerations. For example, the common interpretation of monsoons as land-sea breeze circulations emphasizes the surface temperature gradient, which can affect the surface winds by modifying pressure or geopotential gradients that enter the horizontal momentum equation (e.g., Webster and Fasullo 2003).

In contrast, angular momentum-conserving Hadley circulation theories determine the strength of the Hadley circulation, in an energetic sense, from the top-of-atmosphere energy balance (Held and Hou 1980).

We have found in Chapter 3 that it is useful to consider top-of-atmosphere energetics to understand the response of the cross-equatorial Hadley circulation to orbital precession. However, the surface enthalpy distribution is important in determining the gross moist stability—the energetic stratification that determines the relationship between energy and mass fluxes. Kang and Held (2011) also advocate for the primacy of the energetic perspective over surface perspectives in understanding the precipitation response to hemispherically-asymmetric ocean energy fluxes.

This chapter follows the work of Privé and Plumb (2007a) and Bordoni and Schneider (2008) in interpreting monsoons as regional manifestations of the seasonal migration of the Hadley circulation's convergence zones. The ascending branch of the cross-equatorial Hadley circulation is close to the angular momentum-conserving limit and so can respond directly to energetic changes. However, the surface and its changes can play a role in this limit. First, as in Chapter 3, surface changes can modify the gross moist stability. Second, as in Privé and Plumb (2007a), the surface moist static energy distribution can determine the poleward boundary of monsoonal Hadley circulations; the argument is reviewed in the appendix of the chapter. Last, variations in the surface heat capacity lead to regional and time-dependent differences in the enthalpy fluxes from the surface to the atmosphere (e.g., Neelin 2007).

Land regions differ from oceanic regions in several ways: they have lower surface heat capacity, a limited evaporation reservoir, different surface albedo, orography, and lack fluid energy transports. Some land surface processes will modify the mean climate, but will not affect the response to radiative perturbations. It is of interest here to examine land surface processes that mediate the climate response to orbital precession, i.e., those that interact with the radiative changes. This guides our choice of simulations presented, and we focus on simulations with regions of reduced surface heat capacity and simulations with regions in which land surface hydrology is modelled.

How can orbital precession lead to rectification of the Hadley circulation? Broadly, there are two ways for the annual-mean circulation to change. If the year is divided into warm and cold half years, the annual-mean circulation can change if both half years have similarly signed changes. Alternatively, if one of the half years has changes and the other does not, this will lead to rectification. In this case, one must explain why the circulation is sensitive to insolation changes in one of the half years, but not the other, since the insolation changes are present in both half years with opposite sign.

A concrete example of this second type of rectification is given by threshold behavior. For example, the model of Plumb and Hou (1992) has a regime transition between a viscous circulation and an angular momentum-conserving circulation as off-equatorial thermal forcing is increased. It is not clear that the dynamics described in Plumb and Hou (1992) are relevant for Earth's monsoon circulations since the threshold relies on there being no thermal gradients at the equator, a condition that is not satisfied in Earth's climate.

The aquaplanet simulations in Chapter 3 are an example of the first type of circulation rectification. The Hadley circulation had same signed changes in the two half years: the warm season had weaker Hadley circulation mass fluxes when the insolation increased when perihelion coincided with that season; by symmetry, the cold season mass fluxes increased when there was less insolation. The weaker warm half year and stronger cold half year Hadley circulation do not cancel because the sign of the circulation climatology is reversed. In the annual mean, this lead to Hadley circulation changes centered on the equator.

In this chapter, we examine how the Hadley circulation responds to inhomogeneous heat capacity and surface hydrology. In the simulations with idealized continents presented here, we find that the mass flux of monsoonal Hadley circulations can increase when summers receive more insolation, and this seasonal change can affect the annual-mean Hadley circulation. The summer season changes in the Hadley circulation can be understood by examining the role of the inhomogeneous surface heat capacity on atmospheric energetics and the role that the surface moist static energy distribution

plays in determining the poleward extent of monsoonal circulations. The dynamics of the circulation changes appear to be governed by a previously undocumented mechanism of generating annual-mean changes in the Hadley circulation. The summer responds differently than winter to insolation changes because of the differences in the regime of the angular momentum balance. The cross-equatorial circulation in the summer hemisphere is close to the angular momentum conserving limit, and so it responds directly to thermodynamic and energetic changes. In the winter hemisphere, the Rossby number in the descending branch of the cross-equatorial Hadley circulation is intermediate—it is affected by the energetic midlatitude eddies of the winter hemisphere. So, the descending branch of the circulation is not free to respond directly to energetic changes, such as those due to top-of-atmosphere insolation variations.

The other aspect of the tropical climate that we closely examine are the precession-forced annual-mean changes in precipitation and precipitation minus evaporation. As we have seen in aquaplanet simulations, it is possible to have annual-mean precipitation changes without substantial circulation changes (Chapter 3). However, land surfaces mediate the circulation changes, which in turn will affect the precipitation changes. In the land simulations in this chapter, the dynamic component of net precipitation changes is not negligible and contributes in the same sense as the thermodynamic component of the changes. Land surface hydrology introduces the constraint that annual-mean evaporation cannot exceed annual-mean precipitation in equilibrated climates. This can lead to annual-mean changes in surface temperature and evaporation due to changes in water availability that other simulations do not have.

4.2 Idealized GCM with continents

The simulations presented here use an idealized GCM with the same atmospheric component as that described in Chapter 3, but with slight differences in parameter values. The obliquity of the simulations is the contemporary value of 23.439°, rather

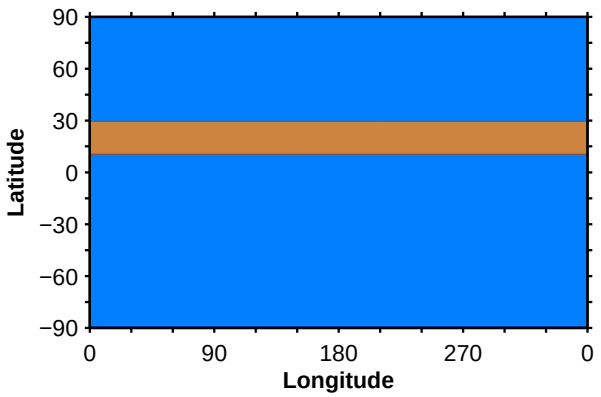

Figure 4.1. Latitude-longitude view of the northern hemisphere subtropical continent boundaries with orange indicating land and blue indicating ocean.

than 23° as in Chapter 3, and the default surface heat capacity is that of 20 m of water rather than 5 m. As in Chapter 3, we show averages over the last 20 years of a simulation following a 10 year spinup period. The substantial changes to the GCM are those associated with including representations of land surface processes in the lower boundary condition, which is described next.

4.2.1 Continent geometry

The continent geometry that we use in the simulations is a zonally symmetric, northern hemisphere subtropical continent with the southern boundary at 10° N and the northern boundary at 30° N (Fig. 4.1). This range of latitudes is chosen so that the continent is in latitudes characteristic of northern hemisphere tropical land masses such as the African Sahel and southern India. It is also a region of annual-mean divergence, and Earth's deserts are located in these subtropical latitudes.

Past work suggests that the placement of the southern boundary of continents can have a substantial impact on precipitation (Dirmeyer 1998), but we have not varied this aspect of the surface boundary condition.

4.2.2 Land model description

Land and ocean differ in several ways. The idealized land model that we use accounts for the differences in heat capacity, the limited evaporation reservoir, and lack of ocean energy flux divergence over land, while it neglects orography and albedo differences.

The mixed layer surface temperature, T_s, evolution equation is

$$\rho_o c_{po} d \frac{\partial T_s}{\partial t} = S_{\text{surf}} - L_{\text{surf}} - LE - H - \nabla \cdot F_o, \tag{4.1}$$

with ocean density ρ_o, ocean heat capacity c_{po}, ocean mixed layer depth d, net shortwave surface radiation S_{surf}, net longwave surface radiation L_{surf}, latent enthalpy flux LE, sensible enthalpy flux H, and ocean energy flux divergence $\nabla \cdot F_o$. The land model consists of modifying d to take into account inhomogeneous surface heat capacity, LE to take account of the limited evaporation reservoir of land surfaces, and setting $\nabla \cdot F_o = 0$ to account for the lack of ocean energy flux divergence in land regions.

The land-sea contrast in heat capacity can be modelled by replacing the constant mixed layer depth d in eqn. 4.1 with a mixed layer depth $d(\lambda, \phi)$ that depends on longitude λ and latitude ϕ. In the model, we express the lower heat capacity of land through changes in the mixed layer depth d, while retaining ocean values for ρ_o and c_{po}. The product of typical values for soil density and specific heat are almost an order of magnitude smaller than those of water: $(\rho c_p)_{\text{land}} \approx 0.15\text{–}0.3 \times \rho_o c_{po}$ (e.g., Pierrehumbert 2010). Temperature perturbations diffuse to a depth that depends on material conductivity κ and forcing frequency ω: $d \sim \sqrt{(}\kappa \rho^{-1} c_p^{-1} \omega^{-1})$. For typical soil conductivities ($\kappa \approx 0.1\text{–}0.3\,\mathrm{W\,m^{-2}\,K^{-1}}$), this depth is $\approx 1\,\mathrm{m}$ for the seasonal cycle (e.g., Pierrehumbert 2010). For land regions, we set the mixed layer depth $d = 0.2\,\mathrm{m}$, consistent with these estimates. One relevant non-dimensional parameter is the ratio of the land heat capacity and atmosphere heat capacity ($\approx 2\,\mathrm{m}$ of water); it is likely that the simulation results are not too sensitive to small variations in this parameter when it is sufficiently smaller than one. Also, with these parameters, the response time of the land surface is short compared to the timescale seasonal cycle.

To model the limited evaporation reservoir over land surfaces, a "bucket depth" variable b is added to the GCM. The bucket depth changes in response to net precipitation, $P - E$:

$$\frac{\partial b}{\partial t} = P - E. \tag{4.2}$$

The standard bulk aerodynamic formula for evaporation,

$$E_0 = \rho c_d ||\mathbf{v}|| (q_s(T_s) - q), \tag{4.3}$$

is modified to cap the evaporative flux of water when it would exceed the amount available at the surface:

$$E = \begin{cases} E_0 & \text{if } b > E; \\ b & \text{otherwise.} \end{cases} \tag{4.4}$$

Therefore, there is no evaporation if there is no surface water available ($b = 0$).

The prescribed ocean energy flux divergence $\nabla \cdot F_o$ (the Q-flux) should be zero where there is land—i.e., there are no fluid energy transports in the land surface. The basic climatological features of tropical precipitation, in particular the land-sea differences, depend on the spatial features of the ocean energy flux divergence (Chou et al. 2001). In Chapter 3, the divergence of the poleward ocean energy flux is represented by the simple function,

$$\nabla \cdot F_o(\phi) = Q_0 \left(\frac{1 - 2\phi^2}{\phi_0^2} \right) \exp\left(-\frac{\phi^2}{\phi_0^2} \right). \tag{4.5}$$

For subtropical continents an alternative Q-flux formulation is required. The approach we take is to use a different amplitude and width north and south of the equator:

$$F_o(\phi) = \begin{cases} Q_{NH}\ 2\pi a^2 \cos(\phi)\, \phi \exp\left(-\frac{\phi^2}{\phi_{NH}^2} \right) & \text{if } \phi > 0; \\ Q_{SH}\ 2\pi a^2 \cos(\phi)\, \phi \exp\left(-\frac{\phi^2}{\phi_{SH}^2} \right) & \text{if } \phi < 0, \end{cases} \tag{4.6}$$

The width and amplitude parameter are reduced in the hemisphere with the subtropical continent: $Q_{NH} = 10\,\mathrm{W\,m^{-2}}$, $\phi_{NH} = 5°$ vs. $Q_{SH} = 50\,\mathrm{W\,m^{-2}}$, $\phi_{SH} = 16°$. The northern hemisphere values are consistent with estimates of the ocean energy flux

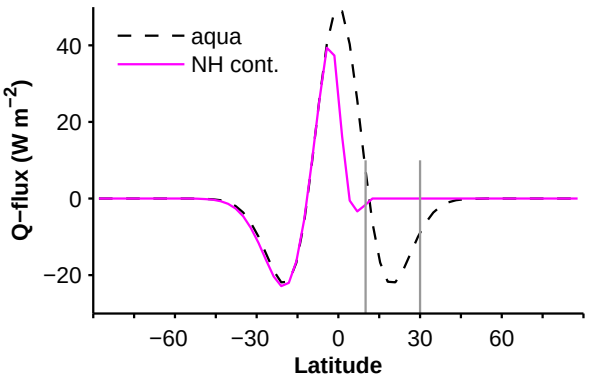

Figure 4.2. Q-flux (ocean energy flux divergence) vs. latitude for northern hemisphere subtropical continent simulations simulations (magenta line) and aquaplanet simulations (black dashed line) with vertical gray lines indicating the continent boundaries.

that assume the interior ocean stratification is adiabatic and the ocean mass transport is given by the Ekman transport (Klinger and Marotzke 2000) and truncating the integral of the temperature flux at the latitude of the southern boundary of the continent. The resulting Q-flux is shown in Fig. 4.2 (magenta line) with the Q-flux used in the aquaplanet simulations (black dashed line).

The ocean energy flux F_o is continuous across the equator, but the meridional divergence of the flux $\nabla \cdot F_o$ is not. To reduce the discontinuity, the flux is prescribed analytically and the divergence is computed numerically using second-order finite differences on the GCM's Gaussian grid. This approach is approximately equivalent to applying a 1–2–1 weighted moving average to the analytical Q-flux.

4.3 Zonally symmetric subtropical continent

One can independently include aspects of the land model in the GCM. For example, if only the asymmetric Q-flux is included, the mean climate changes (there is cooling and less precipitation in the northern hemisphere subtropics), but the climate response to orbital precession is similar to aquaplanet simulations.

We focus on representations of land that modulate the precession-forced changes. In particular, we describe in detail simulations with reduced land heat capacity and

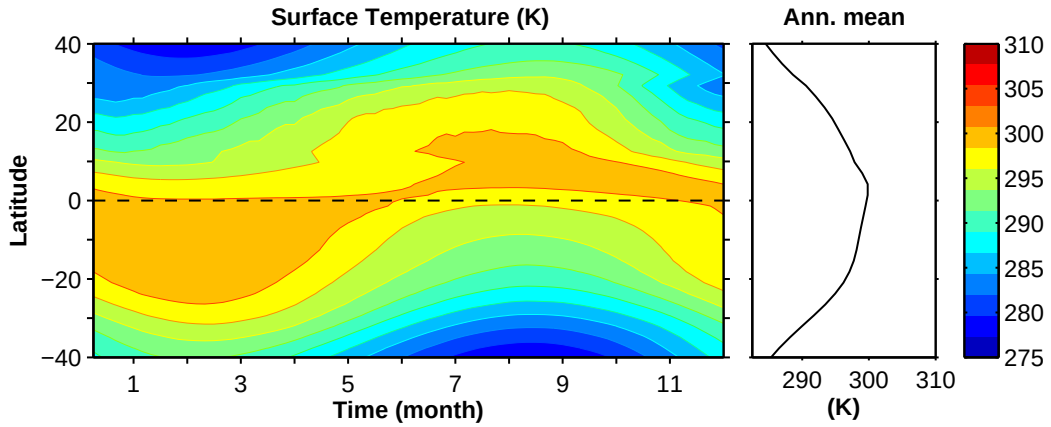

Figure 4.3. Left: Seasonal cycle of surface temperature in heat capacity simulation with perihelion in December. The contour interval is 2.5 K. Right: Annual-mean surface temperature.

simulations with both surface hydrology and reduced land heat capacity (referred to as "surface hydrology" simulations). Both configurations include the hemispherically asymmetric Q-flux.

4.3.1 Heat capacity: surface climate and changes

Here, we present the results of simulations with inhomogeneous heat capacity and hemispherically asymmetric Q-flux; the evaporation reservoir is infinite. In the text, the simulation is referred to as "heat capacity".

When the heat capacity of the continent in the northern hemisphere subtropics is reduced, the surface temperature in the continent region increases rapidly in the beginning of the northern hemisphere summer and decreases rapidly at the end (Fig. 4.3). The increase in temperature at the beginning of summer leads to a transient reversed temperature gradient in June. The relative warmth of the southern hemisphere subtropics is due to the larger Q-flux (right panel of Fig. 4.3).

The intertropical convergence zone (ITCZ) migrates seasonally from 15° S to 8° N, and the annual-mean precipitation is largest near the equator and has local minima in the subtropics as on Earth. The seasonal precipitation maximum does not extend as far poleward in the northern hemisphere as a result of the reduced Q-flux (Fig. 4.4).

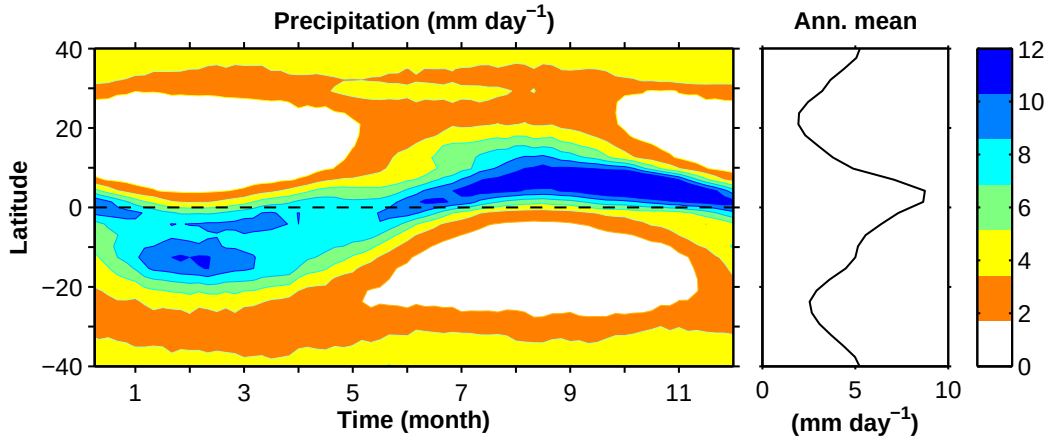

Figure 4.4. Left: Seasonal cycle of precipitation in heat capacity simulation with perihelion in December. The contour interval is 2.0 mm day^{-1}. Right: Annual-mean precipitation.

However, it does extend farther poleward than in a simulation with a hemispherically asymmetric Q-flux and no region of reduced heat capacity (not shown), suggesting that the reduced heat capacity does promote a more poleward monsoon boundary.

When the perihelion is in northern hemisphere summer, the surface temperature over the continent increases nearly as soon as the insolation does (in May), whereas to the south of the continent there is some phase delay (changes are more prominent in August). The annual-mean changes in surface temperature when perihelion is varied between the summer solstices are fairly small (∼0.5 K, right panel of Fig. 4.5).

The precipitation increases in the summer in the northern hemisphere subtropics in the simulation with June perihelion and decreases along the equator throughout the first half of the year (Fig. 4.6). The annual-mean precipitation changes have a dipole pattern centered north of the equator (∼5°) with positive values to the north and negative values to the south (right panel of Fig. 4.6). The magnitude of the annual-mean precipitation changes is ∼1 mm day^{-1}. This is similar to the magnitude of the low thermal inertia aquaplanet simulations and roughly twice as large as the aquaplanet simulation with a uniform 20 m mixed layer depth.

The annual-mean evaporation is not sensitive to the phase of the perihelion as in aquaplanets (dashed line in right panel of Fig. 4.6).

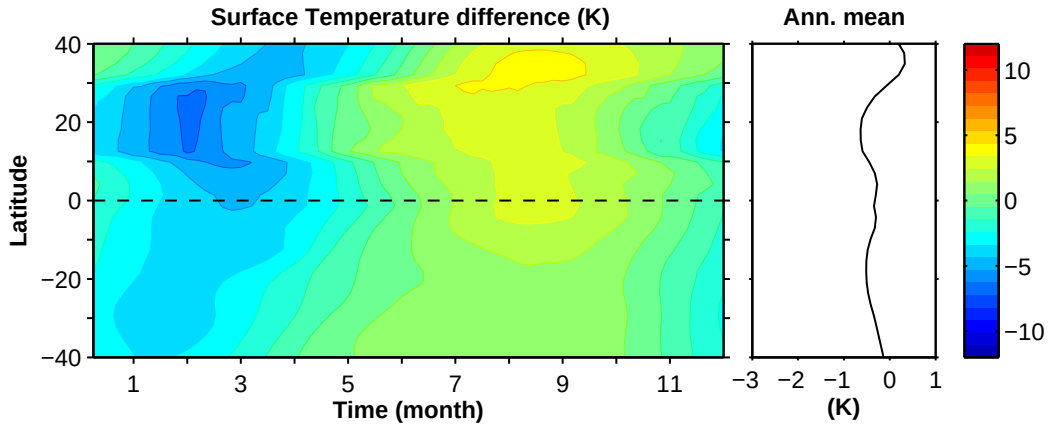

Figure 4.5. Left: Seasonal cycle of surface temperature difference between heat capacity simulations with perihelion in June and December with contour interval of 1 K. Right: Annual-mean surface temperature difference.

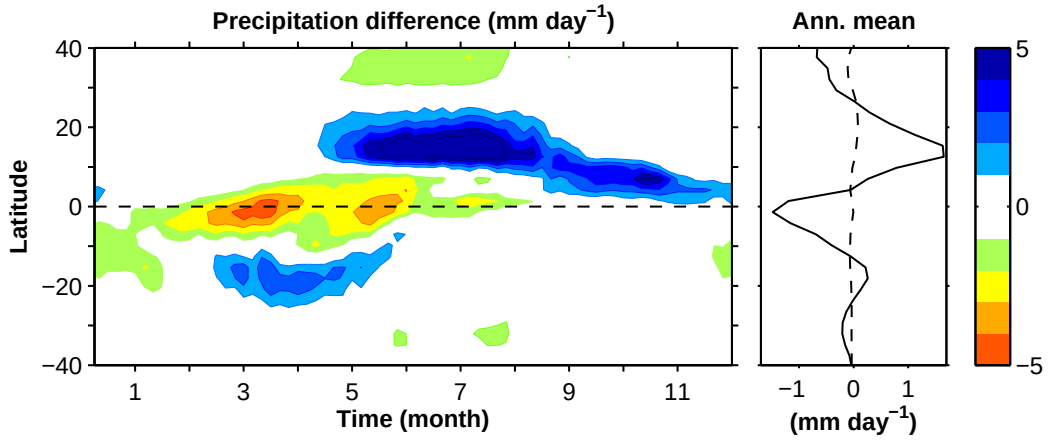

Figure 4.6. Left: Seasonal cycle of precipitation difference between heat capacity simulations with perihelion in June and December. The contour interval is 1 mm day^{-1}. Right: Annual-mean difference in precipitation (solid) and evaporation (dashed) between heat capacity simulations with perihelion in June and December.

We examine the decomposition of the vertically integrated water vapor flux convergence into dynamic and thermodynamic components in Fig. 4.7. When perihelion changes from December to June, the thermodynamic component is antisymmetric about the equator with a moistening tendency north of the equator and a drying tendency south of the equator, as in the aquaplanet simulations. The thermodynamic component is associated with the correlation of the seasonal cycle of the specific hu-

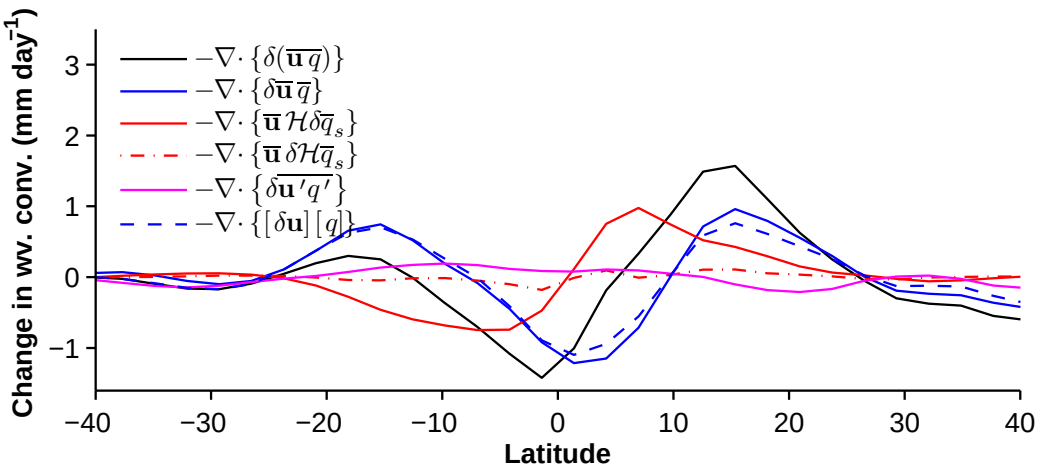

Figure 4.7. Decomposition of annual-mean difference in water vapor flux convergence between heat capacity simulations with perihelion in June and December.

midity changes (increase in the northern hemisphere summer and decrease in northern hemisphere winter) and the seasonal cycle of the unperturbed Hadley circulation mass flux convergence (convergence in northern hemisphere summer and divergence in northern hemisphere winter). Unlike in the aquaplanet simulations, the dynamic component makes a non-negligible contribution to the magnitude and structure of the response of net precipitation to orbital precession. It is the dynamic component that shifts the zero crossing of the change in net precipitation into the northern hemisphere. The magnitude of the dynamic component is $\sim$1 mm day^{-1}; it is larger than the thermodynamic component in the northern hemisphere from 10° to 25°. As in the aquaplanet simulations, the changes in water vapor flux convergence associated with the transient eddy component and changes in relative humidity are negligible. Next, we examine the changes in the mean meridional circulation that are responsible for the dynamic component of the net precipitation changes.

4.3.2 Heat capacity: Hadley circulation

The annual-mean Hadley circulation of the control simulation (December perihelion) is stronger in the northern hemisphere than in the southern hemisphere (left panel of Fig. 4.8). This is a consequence of the hemispherically asymmetric Q-flux—the

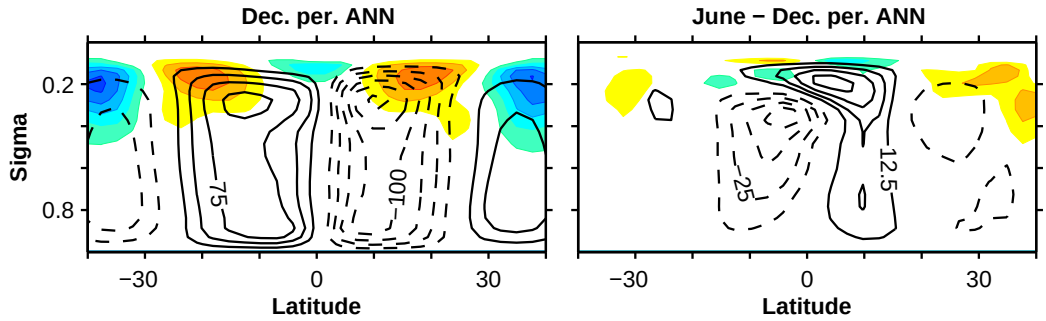

Figure 4.8. Left: Annual-mean Eulerian streamfunction (contours) with contour interval $25 \times 10^9\,\mathrm{kg\,s^{-1}}$ and eddy angular momentum flux divergence (colors) with contour interval $1.2 \times 10^{-5}\,\mathrm{m\,s^{-2}}$ for the heat capacity simulation with perihelion in December. Right: Change in Annual-mean Eulerian streamfunction (contours) with contour interval $12.5 \times 10^9\,\mathrm{kg\,s^{-1}}$ and eddy angular momentum flux divergence (colors) with contour interval $0.6 \times 10^{-5}\,\mathrm{m\,s^{-2}}$ between heat capacity simulations with perihelion in June and December (June − December).

atmosphere energy flux divergence must make up more of the top-of-atmosphere radiative imbalance—and this remains the case when the perihelion occurs in June. The annual-mean Hadley circulation weakens in both hemispheres when perihelion changes from December to June (the changes are of opposite sign as the control circulation, Fig. 4.8). To understand why the Hadley circulation changes this way, it is instructive to consider the seasonal circulations and their changes.

Figure 4.9 shows the Hadley circulation and its changes with perihelion averaged over two six-month periods of the year: from June to November and December to May. The months used in these averages are offset from the equinoxes as the Hadley circulation has some phase lag relative to the insolation; using different months to average (e.g., shifting one month earlier) gives similar results. Here, we see that the annual-mean weakening of the Hadley circulation is actually the result of changes in the cross-equatorial, winter Hadley circulations, which strengthen in both half years when perihelion changes from December to June.

In the northern hemisphere cold season, the strength of the cross-equatorial Hadley circulation increases from $225 \times 10^9\,\mathrm{kg\,s^{-1}}$ to $250 \times 10^9\,\mathrm{kg\,s^{-1}}$ when the perihelion changes from December to June (left column of Fig. 4.9). The southern hemisphere,

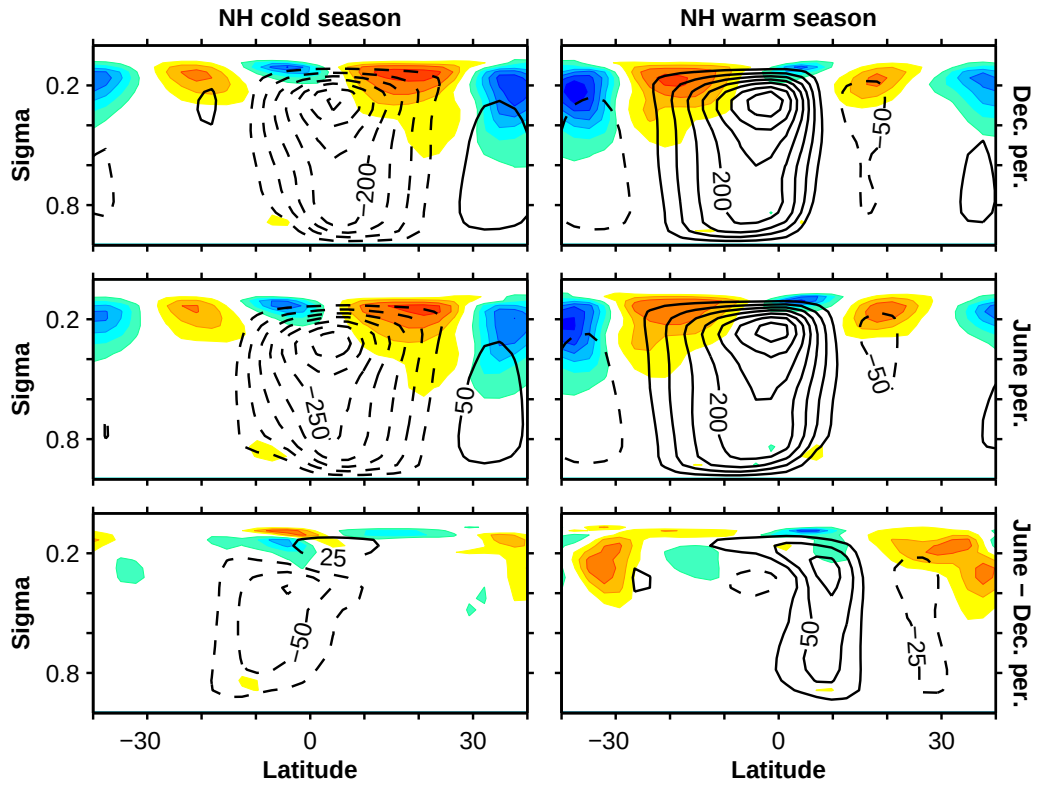

Figure 4.9. Eulerian mean streamfunction (contours) with contour interval $50 \times 10^9\,\mathrm{kg\,s^{-1}}$ and eddy angular momentum flux divergence (colors) with contour interval $1.2 \times 10^{-5}\,\mathrm{m\,s^{-2}}$ for the northern hemisphere cold season (DJFMAM, left column) and northern hemisphere warm season (JJASON, right column) for heat capacity simulations with December perihelion (top row) and June perihelion (middle row). Difference in Eulerian mean streamfunction (contours) with contour interval $25 \times 10^9\,\mathrm{kg\,s^{-1}}$ and eddy angular momentum flux divergence (colors) with contour interval $0.6 \times 10^{-5}\,\mathrm{m\,s^{-2}}$ between heat capacity simulations with June and December perihelion (bottom row).

which has uniform surface properties, has qualitatively similar response to precession changes as the aquaplanet simulations: Hadley circulation mass fluxes are weaker when the perihelion is in that season than when the aphelion is, though there are differences in the spatial structure and magnitude of the changes compared to aquaplanet simulations.

In the northern hemisphere warm season, the cross-equatorial Hadley circulation strengthens when perihelion changes from December to June solstice (right column of Fig. 4.9); this is the opposite sign response as in the aquaplanet simulations.

The warm season circulation changes are largest in the June perihelion case in the beginning of the warm season when the ITCZ is in the northern hemisphere subtropics (as can be indirectly inferred by examining the precipitation changes in Fig. 4.6). As the cross-equatorial circulation is near the angular-momentum conserving limit in the ascending branch, it is instructive to consider the atmospheric circulation's energetics in the presence of an inhomogeneous heat capacity.

The energy balance of the atmosphere and surface is

$$\left\{\frac{\partial \overline{E}}{\partial t}\right\} + \rho_o c_{po} d \frac{\partial \overline{T}_s}{\partial t} = S_{\mathrm{TOA}} - L_{\mathrm{TOA}} - \nabla \cdot \left\{\overline{\mathbf{u}h}\right\} - \nabla \cdot F_o, \tag{4.7}$$

with total atmospheric energy (neglecting kinetic energy) $E = c_v T + gz + Lq$, moist static energy h, net top-of-atmosphere shortwave radiation S_{TOA}, and net top-of-atmosphere longwave radiation L_{TOA}. The mass-weighted integral over the troposphere is indicated by $\{\cdot\}$. If energy storage is negligible, atmosphere-ocean energy flux divergences balance radiation changes: $S_{\mathrm{TOA}} - L_{\mathrm{TOA}} = \nabla \cdot \left\{\overline{\mathbf{u}h}\right\} + \nabla \cdot F_o$. This will be the balance over land surfaces where the surface energy storage is negligible and the ocean energy flux is zero.

When there is spatially inhomogeneous energy storage, the energy balance takes the form

$$S_{\mathrm{TOA}} - L_{\mathrm{TOA}} - \mathcal{A}\, \rho_o c_{po} d \frac{\partial \overline{T}_s}{\partial t} \approx \nabla \cdot \left\{\overline{\mathbf{u}h}\right\} + \nabla \cdot F_o, \tag{4.8}$$

where $\mathcal{A} = [1 - H(\phi - \phi_S) \times H(\phi_N - \phi)]$, with Heaviside step function H, accounts for the inhomogeneous surface energy storage by neglecting that of the continental region; it is assumed in eqn. 4.8 that energy storage in the atmosphere is negligible for simplicity. For perturbations such as insolation changes, this becomes

$$\delta(S_{\mathrm{TOA}} - L_{\mathrm{TOA}}) - [1 - H(\phi - \phi_S) \times H(\phi_N - \phi)] \rho_o c_{po} d \delta \left(\frac{\partial \overline{T}_s}{\partial t}\right) \approx \delta \nabla \cdot \left\{\overline{\mathbf{u}h}\right\}, \tag{4.9}$$

where consistent with the idealized GCM simulations, changes in ocean energy flux divergence have been neglected. We call the term on the left-hand side of eqn. 4.9 the "effective" radiative perturbation δR_{eff}, which includes the inhomogeneous surface

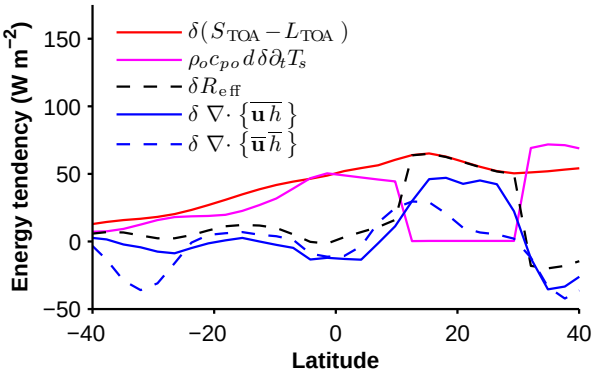

Figure 4.10. June, July, and August (JJA) atmosphere-ocean energy balance difference between heat capacity simulations with June and December perihelion. Not shown: atmospheric energy storage and the budget imbalance.

energy storage term. The central modification of the inhomogeneous heat capacity is then to produce a jump in the effective radiative perturbation at the edge of the continent—where the balance switches from the continental regime with no energy storage in which the atmospheric energy flux divergence must balance the radiative perturbation to the oceanic regime, in which surface energy storage balances essentially all of the radiative perturbation and the atmospheric energy flux divergence do not need to change to balance the top-of-atmosphere energy budget. Knowledge of the effective radiative perturbation does not directly constrain the mean circulation as both the gross moist stability can change (cf. Chapter 3) and the eddy moist static energy flux divergence can change.

Figure 4.10 shows the change in the energy balance of the sum of the atmosphere and surface. The effective net radiation change is positive over the subtropical continent, but is smaller over the adjacent regions with larger heat capacity. The atmospheric moist static energy flux divergence, which must balance the effective net radiation changes, does this by increased mean flow energy flux divergence on the equatorward side of the continent and through increased eddy energy flux divergence on the poleward side of the continent. Figure 4.10 does not show the atmospheric energy storage, which accounts for most of the difference between the atmospheric energy flux divergence and effective radiation perturbation, but does not vary strongly

in latitude. There is also a residual ($\lesssim 15\,\mathrm{W\,m^{-2}}$) at the continent boundary that may be the result of the different discretization used to compute the divergence in the GCM and in the analysis of the simulation results.

Why is it the winter cell that shifts and strengthens (i.e., is the alternative of the summer circulation shifting equatorward and strengthening possible)? The surface moist static energy maximum determines the boundary between the cross-equatorial and summer Hadley circulation (Privé and Plumb 2007a, see the appendix of this chapter for a reproduction of the derivation). Figure 4.11 shows that the moist static energy maximum moves poleward when the perihelion is in June and, consistent with the argument of Privé and Plumb (2007a), the boundary of the monsoonal Hadley circulation nearly coincides with it. We note that the moist static energy distribution is not solely a function of the top-of-atmosphere radiation perturbation. The aquaplanet simulations provide a concrete example: the convergence zone boundaries did not shift when perihelion was varied; this shows that the meridional structure of the insolation changes associated with orbital precession is not sufficient to affect the position of the moist static energy maximum in isolation. Here, the presence of the inhomogeneous surface heat capacity provides meridional structure that shifts the moist static energy maximum northward when the perihelion is in the northern hemisphere summer. Note that the circulation boundary is on average north of the equator and there is a more rapid transition in the simulation with June perihelion (dashed lines in Fig. 4.11).

In Chapter 3, changes in the atmosphere's gross moist stability were important in determining the changes in Hadley circulation strength when perihelion varied. In these simulations, it seems that this is a secondary consideration. The increase in strength of the northern hemisphere warm season cross-equatorial Hadley circulation results from the more rapid transition in the beginning of the season and the overall longer time that the poleward boundary of the cross-equatorial Hadley circulation is in the northern hemisphere (Fig. 4.11).

Why are the Hadley circulation changes confined to the hemisphere of the ascending branch (this occurs in both half years in these simulations and in the northern

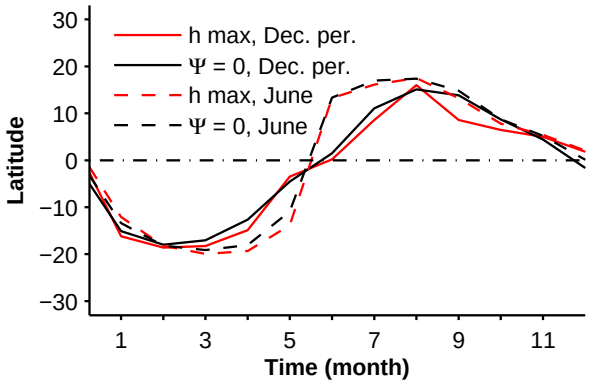

Figure 4.11. Seasonal cycle of the latitude of the maximum near-surface moist static energy ($\sigma = 0.93$, red lines) and the poleward boundary of the cross-equatorial Hadley circulation ($\sigma = 0.67$, black lines) for heat capacity simulations with perihelion in December (solid lines) and June (dashed lines).

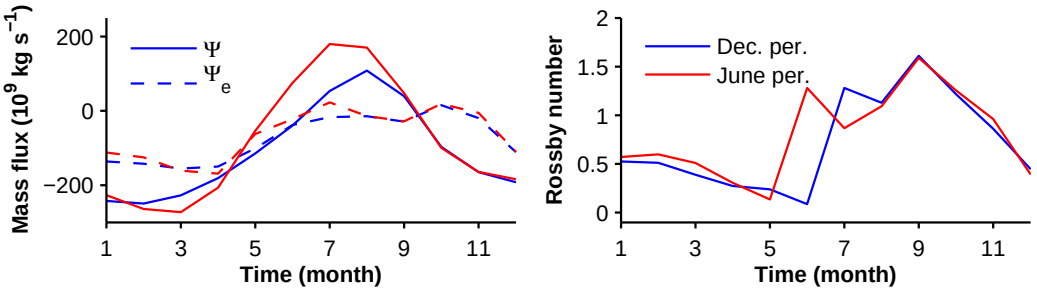

Figure 4.12. Left: seasonal cycle of the streamfunction (solid) and eddy-component of the streamfunction (dashed, see Chapter 3 for definitions) evaluated on the $\sigma = 0.73$ model level at $\phi = 10°$ N for heat capacity simulations with perihelion in June (red) and December (blue). Right: vertically averaged Rossby number $\langle \mathrm{Ro} \rangle$ above the $\sigma = 0.73$ model level at $\phi = 10°$ N; the Rossby number is not plotted for $\Psi < 20 \times 10^9\,\mathrm{kg\,s^{-1}}$ as it is ill-defined for near-zero values.

hemisphere warm season in the simulations with surface hydrology)? This is the result of a previously undiscussed nonlinearity associated with the changing regime of the angular momentum balance. The ascending branch of the cross-equatorial Hadley circulation is close to the angular-momentum conserving limit ($\mathrm{Ro} \sim 1$, right panel of Fig. 4.12). In this regime, the Hadley circulation will respond directly to thermodynamic or energetic changes, such as those associated with changes in the insolation distribution. The descending branch of the cross-equatorial Hadley circulation is typ-

ically of intermediate Rossby number (Ro $\sim$0.5, right panel of Fig. 4.12). In this case, the angular momentum balance is a three-way balance between relative vorticity advection, planetary vorticity advection, and eddy angular momentum flux divergence, so energetic considerations do not directly determine the circulation strength (Schneider 2006; Schneider et al. 2010). Thus, there is an asymmetry between the ascending and descending branch of the Hadley circulation in terms of the momentum balance. Consider a fixed subtropical latitude: the cross-equatorial Hadley circulation in the warm season will change in response to thermodynamic changes; the cross-equatorial Hadley circulation in the cold season is not free to respond directly to thermodynamic changes as it is influenced by eddies. In these simulations, the integrated eddy momentum flux divergence does not change substantially when the phase of perihelion is varied (dashed lines in left panel of Fig. 4.12).

4.3.3 Surface hydrology: surface climate and changes

This section describes the climate response to orbital precession in GCM simulations with the northern hemisphere subtropical continent configuration that includes a limited reservoir for evaporation in addition to an inhomogeneous heat capacity and hemispherically asymmetric Q-flux.[1]

The surface temperature of the control simulation (December perihelion) is substantially warmer in the subtropical continent region when surface hydrology is included (Fig. 4.13). The continent initially has a 1.0 m reservoir of water that dries out because the continent is in a region of net evaporation. For most of the year the bucket depth variable is zero. When the continent has dried out the insolation reaching the surface cannot be balanced by evaporation; surface fluxes of sensible or longwave radiation, which increase less rapidly with temperature than evaporation,

[1]Simulations with surface hydrology and a uniform 20 m mixed layer depth produce an unphysical situation when the perihelion is changed from December to June: when the evaporation reservoir runs out, the surface energy balance changes from a regime dominated by evaporation (balancing the perturbation insolation) to a regime dominated by energy storage. This makes the perturbation effective net radiation gradient negative, which can weaken the circulation and reduce the moisture convergence. When Earth's land surfaces dry out, perturbations to the surface energy budget must be balanced by sensible or longwave surface fluxes and cannot be balanced by surface energy storage.

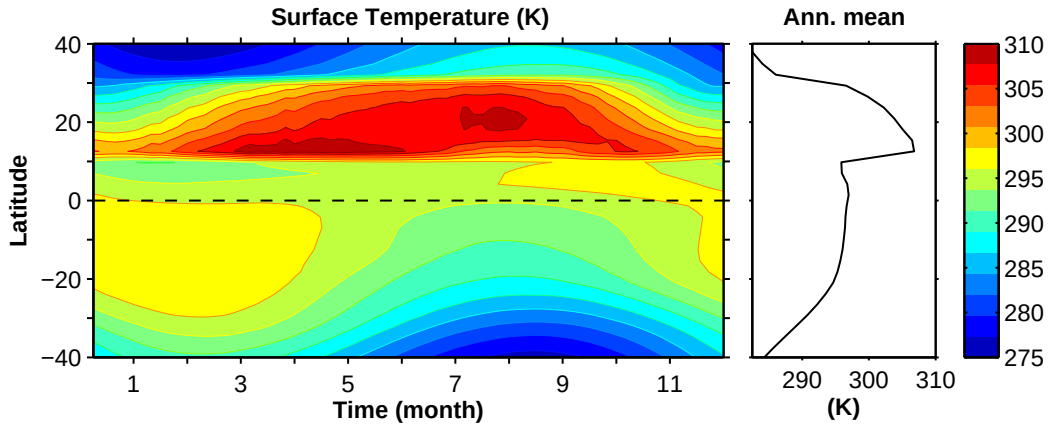

Figure 4.13. Left: Seasonal cycle of surface temperature in surface hydrology simulation with December perihelion. The contour interval is 5 K. Right: Annual-mean surface temperature.

must balance the surface shortwave radiation, and the surface warms. The result is that the maximum surface temperature is on the continent (∼12° N), not at the equator (compare Fig. 4.3 and Fig. 4.13).

The precipitation distribution is biased toward the southern hemisphere when the surface hydrology is included (Fig. 4.14). The ITCZ reaches ∼20° S in southern hemisphere summer, but only to ∼5° N in northern hemisphere summer. The hemispheric asymmetry is larger than in the simulations with heat capacity. The asymmetry in precipitation is associated with the annual-mean Hadley circulation, which is also substantially asymmetric (left panel of Fig. 4.18).

When the perihelion is changed from December to June, the surface temperature change follows the insolation change in the northern part of the continent (north of ∼15°) and over the ocean (Fig. 4.15). There is more sensitivity (warming of ∼10 K) and less phase lag in the continental region than over the ocean as a consequence of the differences in the surface energy balance—lack of evaporative fluxes and different heat capacity. At the southern margin of the continent, the behavior is different: the June perihelion simulation is colder than the December perihelion simulation even when there is more insolation in the northern hemisphere summer (annual-mean cooling of up to 3 K, Fig. 4.15). This is because there is more net precipitation in

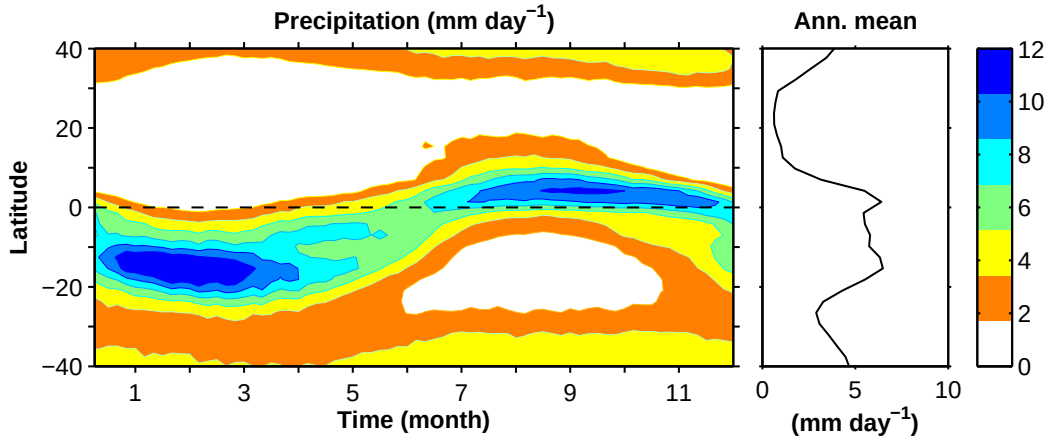

Figure 4.14. Left: Seasonal cycle of precipitation in surface hydrology simulation with December perihelion. The contour interval is 2.0 mm day^{-1}. Right: Annual-mean precipitation.

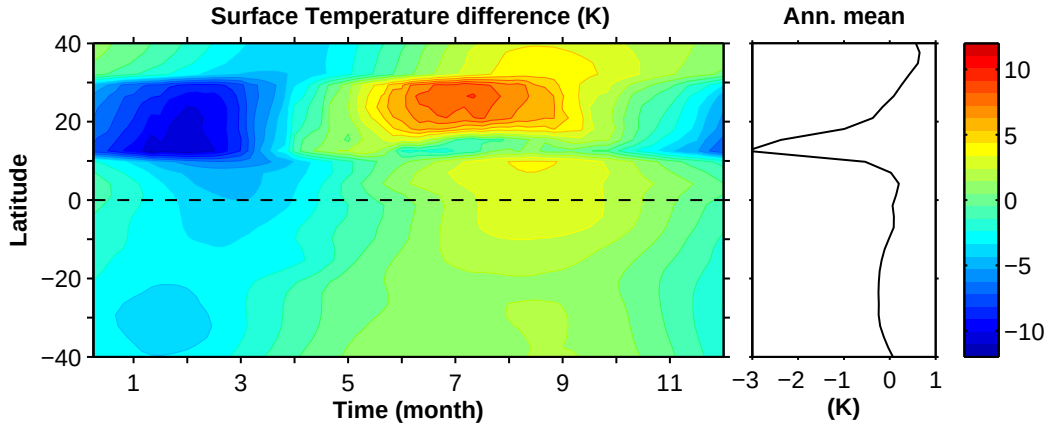

Figure 4.15. Left: Seasonal cycle of surface temperature difference between surface hydrology simulations with perihelion in June and December. The contour interval is 1 K. Right: Annual-mean surface temperature difference.

the simulation with June perihelion ($P - E > 0$) and so the surface energy balance switches from the dry continent regime to one in which evaporation plays a larger role.

Figure 4.16 shows the changes in precipitation between simulations with perihelion in June and December. The seasonal changes are qualitatively similar to the simulation in which only the inhomogeneous heat capacity is taken into account (Fig. 4.6): there is less precipitation near the equator in the first half of the year and there is

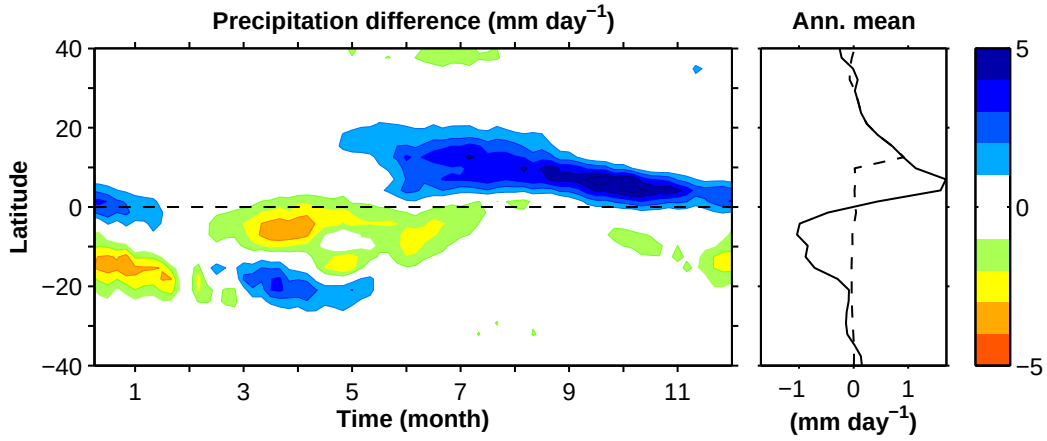

Figure 4.16. Left: Seasonal cycle of precipitation difference between surface hydrology simulations with perihelion in June and December. The contour interval is 1 mm day^{-1}. Right: Annual-mean difference in precipitation (solid) and evaporation (dashed) between surface hydrology simulations with perihelion in June and December.

more precipitation in the northern hemisphere subtropics in summer.

The evaporation in this simulation does have annual mean changes over the southern part of the continent. This is associated with the desert-like regime in which evaporation exactly equals precipitation $E = P$ (i.e., all of the precipitation gets evaporated). In this regime, when a climate change modifies the amount of precipitation, the evaporation will change by the same amount, provided the region stays in the desert, $E = P$ limit. Along the southern edge of the continent, there is an increase in annual-mean net precipitation.

The annual-mean water vapor flux convergence and its decomposition is shown in Figure 4.17. The continent, aside from the southernmost edge, has no change in water vapor flux convergence as it stays in the regime in which evaporation equals precipitation. In other words, there is no annual-mean convergence of water vapor regardless of the phase of perihelion. In this limit, the water vapor budget does not constrain the precipitation changes, and it may be more useful to consider the (dry) thermodynamic or moist static energy budget to understand how precipitation changes.

The thermodynamic change in water vapor flux convergence shows the familiar

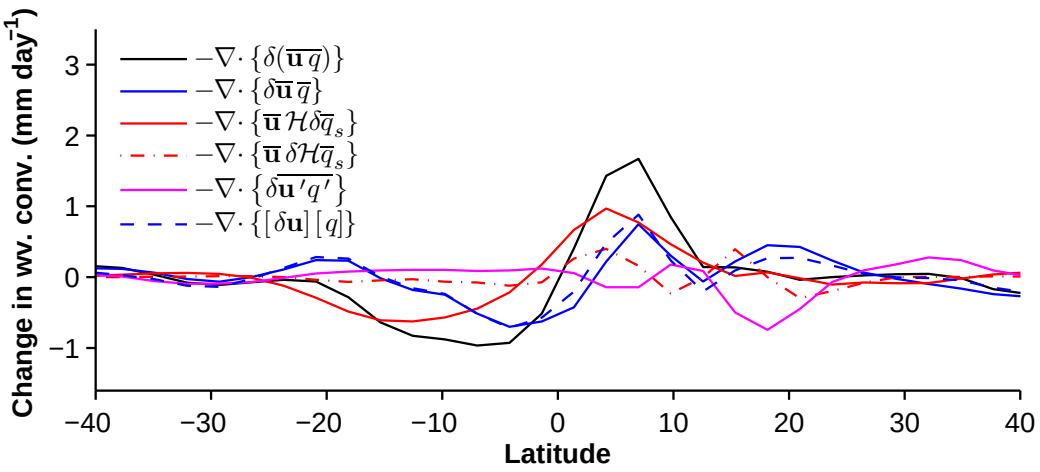

Figure 4.17. Decomposition of annual-mean difference in water vapor flux convergence between surface hydrology simulations with perihelion in June and December.

pattern of hemispheric antisymmetry. The dynamic component of the change is as large as the thermodynamic component and contributes to the pattern of drying in the southern hemisphere and moistening in the northern hemisphere.

The constraint of the land surface hydrology has been discussed previously in the context of orbital precession, though in slightly different terms. Ruddiman (2008) suggests that even if the atmospheric circulation is not rectified (i.e., monsoonal circulations respond linearly to insolation over northern hemisphere subtropical continents so summer convergence and winter divergence both increase when perihelion is in northern hemisphere summer), the water vapor flux divergence is small in winter because it is sufficiently dry, independent of circulation changes. There is some evidence for this in the perpetual-January GCM simulations presented in Kutzbach (1985), which had small changes in net precipitation in northern hemisphere subtropical continental regions as orbital parameters including perihelion were varied. In these simulations, evaporation changed slightly with the sign of the changes following the insolation change, while precipitation changed little; the magnitude of the $P - E$ changes in perpetual January simulations was substantially smaller than in perpetual July simulations.

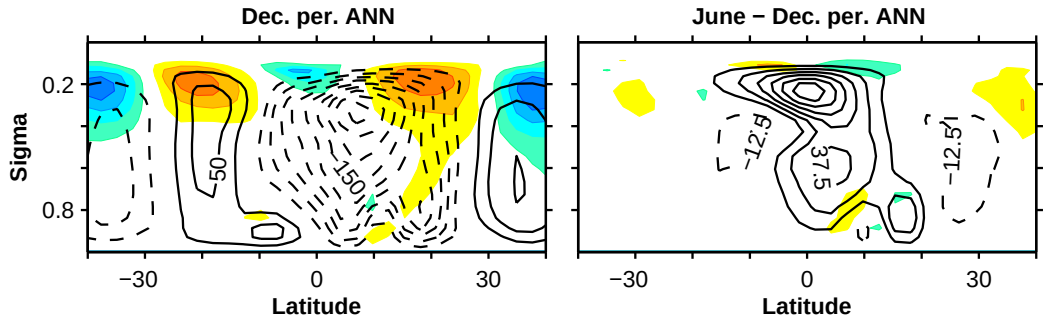

Figure 4.18. Left: Annual-mean Eulerian streamfunction (contours) with contour interval $25 \times 10^9\,\mathrm{kg\,s^{-1}}$ and eddy angular momentum flux divergence (colors) with contour interval $1.2 \times 10^{-5}\,\mathrm{m\,s^{-2}}$ for surface hydrology simulation with perihelion in December. Right: Change in annual-mean Eulerian streamfunction (contours) with contour interval $12.5 \times 10^9\,\mathrm{kg\,s^{-1}}$ and eddy angular momentum flux divergence (colors) with contour interval $0.6 \times 10^{-5}\,\mathrm{m\,s^{-2}}$ between surface hydrology simulations with perihelion in June and December (June − December).

4.3.4 Surface hydrology: Hadley circulation

The annual-mean Hadley circulation is notably asymmetric in simulations with limited surface evaporation reservoirs (left panel of Fig. 4.18) as a result of the substantial radiative cooling in the continental region (both warmer temperature and lower humidity contribute to the large cooling). The annual-mean Hadley circulation weakens in the northern hemisphere when the perihelion is changed from December to June (right panel of Fig. 4.18). The sign of the change is similar to the heat capacity simulations, but the magnitude is greater; the southern hemisphere response is weaker than in the heat-capacity-only simulations.

The northern hemisphere warm season Hadley circulation has a shallow circulation that is likely a consequence of the reversed meridional temperature gradient (Fig. 4.13) and concomitant barotropic or mixed barotropic-baroclinic instability (e.g., Thorncroft and Hoskins 1994). Shallow circulations associated with maxima in surface potential temperature appear to be a generic feature of Earth's climate (Nie et al. 2010).

The annual-mean change in the Hadley circulation is due largely to the changes in the northern hemisphere warm season cross-equatorial Hadley circulation (Fig. 4.19).

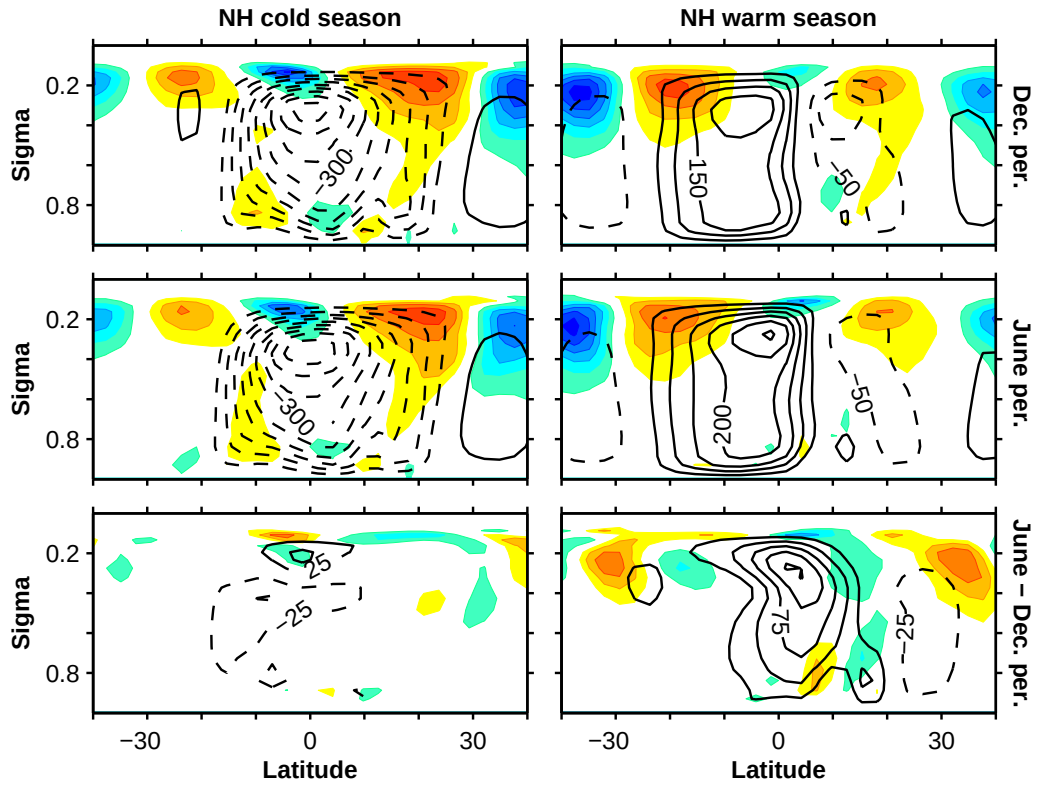

Figure 4.19. Eulerian mean streamfunction (contours) with contour interval $50 \times 10^9\,\mathrm{kg\,s^{-1}}$ and eddy angular momentum flux divergence (colors) with contour interval $1.2 \times 10^{-5}\,\mathrm{m\,s^{-2}}$ for the northern hemisphere cold season (DJFMAM, left column) and northern hemisphere warm season (JJASON, right column) for surface hydrology simulations with December perihelion (top row) and June perihelion (middle row). Difference in Eulerian mean streamfunction (contours) with contour interval $25 \times 10^9\,\mathrm{kg\,s^{-1}}$ and eddy angular momentum flux divergence (colors) with contour interval $0.6 \times 10^{-5}\,\mathrm{m\,s^{-2}}$ between surface hydrology simulations with June and December perihelion (bottom row).

The change in this season is larger than in the heat capacity simulations. We note that the surface hydrology simulation with June perihelion has a stronger monsoonal Hadley circulation and lower land-sea surface temperature contrast compared to the simulation with December perihelion. In other words, the pair of simulations provide a clear counter-example to the idea of monsoons as a sea breeze circulation.

The Hadley circulation changes in response to orbital precession are similar in simulations in which all precipitation over land is assumed to instantly run off, i.e., there is never water available for evaporation. This suggests that the changes in

surface properties due to precession are not essential in determining the changes in the atmospheric circulation, although the region with annual-mean changes in evaporation is not large in these simulations.

The changes in top-of-atmosphere energy balance when perihelion is changed from December to June are similar to the heat capacity simulations: the effective radiation perturbation has a jump at the southern boundary of the continent, and this is balanced by changes in the energy flux divergence by the mean circulation. We do not show the corresponding figure because it is qualitatively similar to Fig. 4.10. It is worth noting that because these are changes in top-of-atmosphere radiation, the response of the atmospheric circulation, in energetic terms, does not depend on the details of the surface. This can be viewed as the result that surface fluxes over land are in equilibrium (e.g., section 7c of Neelin and Zeng (2000) and Neelin (2007)). The two sets of simulations explicitly demonstrate this: one pair has a nearly dry surface and the other has a humid surface, but the top-of-atmosphere energy balance is similar.

Figure 4.20 shows that the near surface moist static energy maximum and boundary of the Hadley circulation also coincide in the land simulations. The details of the agreement depend somewhat on the model levels on which the variables are evaluated. It seems like the changing length of the season in which the poleward boundary of the cross-equatorial Hadley circulation is in the northern hemisphere is a large part of the changes in the annual-mean Hadley circulation.

The decomposition of the streamfunction into eddy-driven component and the vertically-integrated Rossby number at 10° N is noisier and more sensitive to averaging conventions in surface hydrology simulations than in heat capacity simulations (not shown). This is due to the more detailed vertical structure of the eddy momentum fluxes (Fig. 4.19) and to the fact that the streamfunction is near zero at this latitude for a substantial part of the northern hemisphere summer (Fig. 4.20).

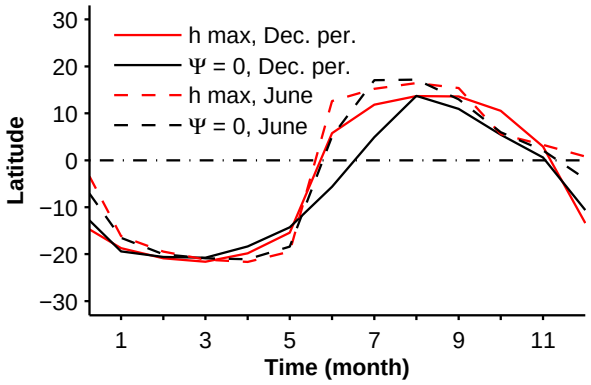

Figure 4.20. Seasonal cycle of the latitude of the near-surface moist static energy ($\sigma = 0.93$, red lines) and the poleward boundary of the cross-equatorial Hadley circulation ($\sigma = 0.67$, black lines) for surface hydrology simulations with perihelion in December (solid lines) and June (dashed lines).

4.4 Conclusions

The mean meridional atmospheric circulation can strengthen in response to increases in insolation due to orbital precession if there is a region of low heat capacity. We understand the Hadley circulation response in terms of the top-of-atmosphere energy balance and the "effective" radiative perturbation, which is small over the ocean and large over land, at the southern continent boundary. That it is the monsoonal Hadley circulation that balances the radiative perturbation can be understood through the estimate for the poleward monsoon boundary of Privé and Plumb (2007a). The poleward circulation boundary coincides with the maximum in surface moist static energy. The surface moist static energy increases with insolation, more rapidly over regions of low heat capacity than large heat capacity. When perihelion is at the northern hemisphere summer solstice, the maximum in surface moist static energy shifts north in the early part of the northern hemisphere summer and the atmospheric circulation follows. The reason that this gives rise to annual-mean Hadley circulation changes appears to be associated with the longer time that the Hadley circulation is in the northern hemisphere.

Consistent with the substantial circulation changes, the dynamic component of

precipitation is not negligible when there is a subtropical continent. The thermodynamic component of net precipitation changes leads to moistening in the northern hemisphere when perihelion changes from December to June. This is likely a robust response, as it only relies on the climatology of the atmospheric circulation having more convergence in summer and temperature and specific humidity increasing in response to additional insolation.

A limited evaporation reservoir can change the sign of the surface temperature response to increased insolation if there is increased precipitation and thus evaporation over a (formerly) dry region.

There are several issues that are outstanding. In particular, a quantitative understanding of the Hadley circulation changes in these simulations remains an outstanding challenge.

Preliminary examination of simulations with a northern hemisphere subtropical continent of finite zonal extent (spanning 180°) has changes that are a mixture of the aquaplanet and zonally-symmetric subtropical continent: the meridional circulation increases in the continent longitudes and decreases in the oceanic longitudes.

Preliminary examination of simulations with continental geometry of finite zonal extent that spans both hemispheres from pole-to-pole suggests that the eastern and western regions of the continent respond differently. The results appear consistent with the dynamics described Rodwell and Hoskins (1996): there is a larger precipitation increase on the eastern edge of the continent than to the west, plausibly because convecting regions shed Rossby waves that propagate to the west and force subsidence there.

Last, an examination of these mechanisms (effective radiative perturbation, surface moist static energy maximum determining the poleward monsoon boundary, and the time-dependence of the Rossby number) in comprehensive models would build confidence in the results presented here.

4.5 Acknowledgments

We thank Sonja Graves for providing modifications to the GCM code.

4.6 Appendix: The relationship between the poleward monsoon boundary and the surface moist static energy maximum of Privé and Plumb

First, thermal wind balance is expressed in specific volume α

$$\frac{\partial u}{\partial p} = \frac{1}{f}\frac{\partial \alpha}{\partial y}. \tag{4.10}$$

Second, one of the Maxwell relations is used to express the meridional specific volume gradient in terms of temperature and moist entropy gradients,

$$\left(\frac{\partial \alpha}{\partial y}\right)_p = \left(\frac{\partial T}{\partial p}\right)_{s^*} \frac{\partial s^*}{\partial y}, \tag{4.11}$$

where s^* is the saturation moist entropy and $(\cdot)^*$ indicates a saturation quantity (Emanuel 1994).

In surface quasi-equilibrium, the surface moist entropy s_b determines that of the free-troposphere: $s^* = s_b$.

Putting together these relationships, the thermal wind balance can be re-expressed in terms of the moist adiabatic lapse rate and the surface moist entropy gradient,

$$\frac{\partial u}{\partial p} = \frac{1}{f}\left(\frac{\partial T}{\partial p}\right)_{s^*} \frac{\partial s_b}{\partial y}. \tag{4.12}$$

The surface moist entropy s_b is closely related to the surface moist static energy h_b: $\delta h_b \approx T_b \delta s_b$.

$$\frac{\partial u}{\partial p} = \frac{1}{f}\left(\frac{\partial T}{\partial p}\right)_{s^*} \frac{1}{T_b}\frac{\partial h_b}{\partial y}. \tag{4.13}$$

If circulation is angular momentum-conserving, the boundary will be in region of

no shear ($\partial_p u \approx 0$), as this is a region in which there is no meridional momentum advection and vertical momentum advection homogenizes the vertical momentum distribution, if the circulation boundary is vertical. The condition on the vertical boundary of the circulation results from transforming between the streamfunction coordinate (the angular momentum of the flow is conserved along streamlines) and pressure coordinates

$$\frac{\partial m}{\partial \Psi} = \frac{\partial m}{\partial p}\frac{\partial p}{\partial \Psi} = 0, \tag{4.14}$$

where $m = (\Omega a \cos\phi + u)\, a\cos\phi$ is the absolute angular momentum.

As the left-hand side of eqn. 4.13 is zero, this implies one either $(\partial_p T)|_{s^*} = 0$ or $\partial_y h_b = 0$. The moist adiabatic lapse rate is not zero, so the poleward boundary of the Hadley circulation occurs where $\partial_y h_b = 0$. Therefore, the maximum in h_b determines the circulation boundary, the region of ascent and precipitation will be equatorward of this.

Chapter 5

Conclusions

Here, the main results of the thesis and the outstanding questions emerging from these results are summarized.

The response of tropical zonal asymmetries to climate changes forced by perturbed longwave radiation was examined in Chapter 2. The zonal surface temperature difference decreased rapidly with warming, which can be accounted for by considering a simplified surface energy balance: the zonally asymmetric component of the surface energy balance is dominated by evaporation and the ocean energy flux divergence. For an invariant ocean energy flux divergence, the invariant evaporation can be converted in a surface temperature difference by making suitable approximations to the bulk-aerodynamic formula for evaporative fluxes. The resulting estimate suggests the surface temperature difference decreases at a rate given by the inverse of the rate of change of the saturation specific humidity with temperature.

In these simulations, the Walker circulation weakened rapidly with warming. Arguments based on changes in the hydrological cycle account for the simulation results provided that they are evaluated locally. In the global mean, precipitation changes are energetically constrained, but global-mean versions of the scaling estimate do not adequately account for Walker circulation changes; they underestimate the changes in Earth-like and colder climate, for example.

There remain outstanding questions about how tropical zonal asymmetries respond to greenhouse gas–type radiation perturbations. In particular, we have not considered the potentially important interactions between the atmospheric and oceanic

circulations or the interaction between the atmospheric circulation and clouds, which can have large radiative impacts locally. Our discussion of the Walker circulation focused on the water vapor balance (which is equivalent to the potential temperature budget), as this has been emphasized in recent literature (Held and Soden 2006; Vecchi and Soden 2007). Another potentially useful avenue to constrain how the Walker circulation changes with climate is the moist static energy budget, which notably does not have a precipitation term in the budget. Appendix C of Chapter 2 sketches the possible implications of the moist static energy budget for the Walker circulation. Another precipitation-free estimate for the Walker circulation is provided by the Lindzen-Nigam model, which assumes the surface winds can be related to the surface temperature. The Lindzen-Nigam model does not capture the GCM-simulated changes in the Walker circulation (Appendix B of Chapter 2), suggesting that further work is required to develop a reduced vertical structure model that captures the interaction between surface-forced convergence and deep circulation (see also, Back and Bretherton 2009; Sobel and Neelin 2006).

Chapter 3 examined the climate response to orbital precession in aquaplanet simulations. The changes in insolation associated with orbital precession change many aspects of the climate seasonally and cause annual-mean changes in tropical precipitation. In aquaplanet simulations, this is the result of thermodynamic changes in the water vapor convergence. Interestingly, these simulations feature weaker monsoonal (cross-equatorial) Hadley circulations when the perihelion occurs at the summer solstice than the winter solstice. This counter-intuitive result can be understood by considering the circulation energetics. Moist angular momentum-conserving Hadley circulation theories constrain the energy fluxes of the circulation, which is the product of the circulation's mass flux and the gross moist stability. For precession variations, the changes in gross moist stability are not negligible and, in fact, dominate over the changes in Hadley circulation mass fluxes.

The Held (2001) estimate for the gross moist stability is useful away from the ascending branch of the Hadley circulation, but the determination of the gross moist stability in ascending regions is an important unresolved issue. Likewise, the pro-

cesses setting the seasonal cycle of the latitude of the convergence zone for circular orbits have not been laid bare. While the surface moist static energy maximum is conceptually useful, the circulation itself partially determines the energy distribution (e.g., see the analogous discussion in dry simulations in Schneider and Bordoni 2008). Understanding the seasonal cycle of the climatological Hadley circulation convergence is important in determining the latitudes where the thermodynamic component has substantial amplitude and would be useful to gain understanding beyond the perturbation estimate that is outlined in Chapter 3

In Chapter 4, we examined changes in the surface climate and general circulation of the tropical atmosphere in simulations with representations of land surface processes in the northern hemisphere subtropics. The cross-equatorial Hadley circulation in northern hemisphere summer does increase when perihelion is changed from December solstice to June solstice, in contrast to aquaplanet simulations. The mechanism by which this change occurs is a combination of i) low thermal inertia of the continent leading to a larger effective radiative perturbation at the southern boundary of the continent and ii) rapid increase in the surface moist static energy at the beginning of the monsoon onset in the continental region with reduced thermal inertia that causes the cross-equatorial Hadley circulation boundary to shift poleward. The lack of energetic changes in the winter due to the lower Rossby number in the descending branch of the cross-equatorial Hadley circulation than in the ascending branch of the cross-equatorial Hadley circulation leads to the preservation of the seasonal change in the annual-mean. The precipitation changes in these simulations are influenced by both thermodynamic and dynamic changes in water vapor flux convergence. Last, when surface hydrology is included, the surface temperature and evaporation can have annual-mean changes in response to orbital precession that result from the availability of water for evaporation in the surface reservoir, which in turn depends on precipitation changes.

The examination of the simulations with representations of land in Chapter 4 leaves outstanding questions about the detailed role of continent geometry and how to develop quantitative estimates for Hadley circulation changes. Also, consideration

of the water vapor budget is not useful in constraining precipitation changes in dry continents that stay in the $E = P$ regime, so an examination of the implications of the thermodynamic budget or moist static energy budget for precipitation may be enlightening.

Chapter A presents a systematic examination of the linear stability of the mean flows of dry atmospheres. The results show that the length scale of the most unstable waves is similar to the Rossby radius and the energy-containing eddy length scale of the corresponding nonlinear simulation. The growth rate of the most unstable waves is similar to the Eady growth rate.

Outstanding questions in the topic of the eddy scales of atmospheric turbulence include how the effect of latent heat release modifies dry theories and what is the minimal closure that adequately captures the meridional propagation, as the eddy flux divergences of the linear waves and weakly nonlinear eddy (O'Gorman and Schneider 2007) have smaller meridional scales than nonlinear simulations.

Chapter B presents simulations of the atmospheric circulation of Earth-like tidally locked aquaplanets and compares them to existing theoretical arguments. In particular, aspects of the atmospheric circulation and thermal structure can be anticipated by considering the non-dimensional parameters the Rossby number and the Froude number, respectively. The atmospheric circulation is important in determining the surface climate. For example, the night-side surface temperatures are far from 0 K in both simulations. Also, the structure of precipitation regions differs between the slowly and rapidly rotating simulations as a consequence of the differences in the atmospheric circulations.

Outstanding questions in the study of tidally locked planets include adequate theoretical explanations for the results of systematic rotation rate variation (see the last two figures in Chapter B) and how including additional physical processes such as the ocean circulation, the radiative effects of clouds, and representations of the cryosphere would change the simulated climates.

Appendix A

Scales of linear baroclinic instability and macroturbulence in dry atmospheres

This chapter is a reproduction of Merlis and Schneider (2009).

A.1 Abstract

Linear stability analyses are performed on a wide range of mean flows simulated with a dry idealized general circulation model. The zonal length scale of the linearly most unstable waves is similar to the Rossby radius. It is also similar to the energy-containing zonal length scale in statistically steady states of corresponding nonlinear simulations. The meridional length scale of the linearly most unstable waves is generally smaller than the energy-containing meridional length scale in the corresponding nonlinear simulations. The growth rate of the most unstable waves increases with increasing Eady growth rate, but the scaling relationship is not linear in general. The available potential energy and barotropic and baroclinic kinetic energies of the linearly most unstable waves scale linearly with each other, with similar partitionings among the energy forms as in the corresponding nonlinear simulations. These results show that the mean flows in the nonlinear simulations are baroclinically unstable, yet there is no substantial inverse cascade of barotropic eddy kinetic energy from the baroclinic generation scale to larger scales, even in strongly unstable flows. Some aspects of the nonlinear simulations, such as partitionings among eddy energies, can be understood on the basis of linear stability analyses; for other aspects, such as

the structure of heat and momentum fluxes, nonlinear modifications of the waves are important.

A.2 Introduction

In Earth's atmosphere, scales of the energy-containing eddies are similar to those of the linearly most unstable baroclinic waves. The energy-containing length scale (spherical wavenumber ∼8) is similar to the zonal length scale of the most unstable waves, and the eddy turnover time (∼3–5 days) is similar to their inverse growth rate (e.g., Shepherd 1987a; Simmons and Hoskins 1976; Valdes and Hoskins 1988). Analysis of observations shows that eddy-mean flow interactions, not nonlinear eddy-eddy interactions, dominate the spectral energy transfers; there is no extended wavenumber range of nonlinear (transient) eddy-eddy interactions that could give rise to an inverse energy cascade and an upscale transfer of eddy energy from the scale of generation by baroclinic instability to significantly larger scales (Shepherd 1987b,a). Theory and simulations with an idealized dry general circulation model (GCM) suggest this agreement of linear wave scales and nonlinear eddy scales does not occur by chance but results because macroturbulence modifies the atmospheric thermal structure such that nonlinear interactions among turbulent eddies are weak (Schneider and Walker 2006). Nonetheless, while the nonlinear eddy-eddy interactions that cause differences between linear wave scales and nonlinear eddy scales may be weak, they are not absent altogether. For example, meridional momentum fluxes associated with linear waves are generally confined to a narrower latitude band than those associated with fully developed nonlinear eddies, indicating that linear waves have smaller meridional scales and/or do not propagate meridionally as effectively as the nonlinear eddies (Gall 1976a,b; Simmons and Hoskins 1976, 1978; Edmon et al. 1980; O'Gorman and Schneider 2007).

As basis for a systematic study of differences between linear waves and fully developed nonlinear eddies, here we present linear stability analyses of a wide range of atmospheric mean flows simulated with an idealized dry GCM. The mean flows

are a subset of those whose fully developed nonlinear dynamics were examined in Walker and Schneider (2006), Schneider and Walker (2006, 2008) (hereafter, SW06 and SW08), allowing us to compare properties of linear waves with theoretical predictions on the one hand and with properties of nonlinear eddies on the other hand. The use of a wide range of simulations enables us to make such comparisons systematically. For example, we are able to compare mean-field estimates for scales of linear waves based on idealized quasigeostrophic models with scales of linear waves on a wide range of complex mean flows in a primitive-equation model, allowing us to determine empirical constants in scaling relations. The systematic comparison of linear waves and nonlinear eddies in dry atmospheres is a necessary prerequisite for further studies in atmospheric macroturbulence that may attempt to develop turbulence closures (e.g., based on weakly nonlinear models) or add neglected physical processes (e.g., latent heat release in phase changes of water). In this paper, we (i) show that the mean flows whose nonlinear dynamics were examined in SW06, SW08, and SM09 are indeed baroclinically unstable, (ii) demonstrate that mean-field estimates such as the Rossby radius and Eady growth rate account for properties of linear waves such as their zonal length scale and growth rate (albeit not always precisely), and (iii) examine limitations of linear stability analysis in accounting for properties of nonlinear eddies.

A.3 Idealized GCM and linear stability analyses

A.3.1 Model description

We performed linear stability analyses of the simulated mean flows described in SW06, SW08, and SM09. The GCM with which the flows are simulated is based on the spectral dynamical core of the Geophysical Fluid Dynamics Laboratory's Flexible Modeling System. It integrates the primitive equations on the sphere, discretized with the spectral transform method in the horizontal (resolution from T42 to T127 for different simulations), and with 30 unevenly spaced sigma coordinate levels in the

vertical. Forcing and dissipation in the nonlinear simulations consist of Newtonian relaxation of temperatures as a representation of radiation, a turbulent boundary layer scheme (roughness length 5 cm) acting in the lowest 2.5 km of the model atmosphere (Smagorinsky et al. 1965), and ∇^8 hyperviscosity acting on vorticity, divergence, and temperature. A quasi-equilibrium dry convection scheme relaxes temperatures to a profile with convective lapse rate $\gamma\Gamma_d$, where Γ_d is the dry-adiabatic lapse rate $\Gamma_d = g/c_p$, whenever a column is statically less stable than a column with the convective lapse rate. If $\gamma < 1$, the convection scheme mimics some of the stabilizing effect that latent heat release has on the thermal structure of the atmosphere (details can be found in appendix B of SW06).

The Newtonian relaxation is toward the radiative equilibrium of a semigray atmosphere (transparent to shortwave radiation and gray to longwave radiation), with a spatially varying timescale. The surface temperature in radiative equilibrium varies with latitude ϕ as (SW06)

$$T_s^e(\phi) = \tilde{T}_s^e + \Delta_h \cos^2\phi. \tag{A.1}$$

The pole-equator surface temperature contrast Δ_h is one of the parameters varied to obtain different mean flows; the polar temperature $\tilde{T}_s^e = 260\,\mathrm{K}$ is constant in all simulations. The vertical structure of the radiative-equilibrium temperature is given by

$$T^e(\phi, p) = T_t^e \left[1 + d_0(\phi)\left(\frac{p}{p_0}\right)^\alpha\right]^{1/4}, \tag{A.2}$$

with constant skin temperature $T_t^e = 200\,\mathrm{K}$ at the top of the atmosphere, reference pressure $p_0 = 1000\,\mathrm{hPa}$, and exponent $\alpha = 3.5$. The optical depth

$$d_0(\phi) = \left[\frac{T_s^e(\phi)}{T_t^e}\right]^4 - 1 \tag{A.3}$$

is chosen so that the radiative-equilibrium temperature makes a continuous transition from the constant skin temperature T_t^e to the surface temperature $T_s^e(\phi)$ (Schneider 2004).

The Newtonian relaxation time τ_r varies with latitude and pressure according to

$$\tau_r^{-1}(\phi, \sigma) = \tau_i^{-1} + (\tau_s^{-1} - \tau_i^{-1}) \ \max\left(0, \frac{\sigma - \sigma_b}{1 - \sigma_b}\right) \cos^8 \phi, \tag{A.4}$$

where $\sigma = p/p_s$ with surface pressure p_s and $\sigma_b = 0.85$ (Schneider 2004). The time constants τ_i and τ_s allow different relaxation times in the interior atmosphere and near the surface in low latitudes.

A.3.2 Series of simulations

Several series of nonlinear, forced-dissipative simulations have been performed with the idealized GCM. Here, we describe the subset of simulations for which we performed linear stability analyses. In one set of simulation series, we set the convective rescaling parameter to values $\gamma = (0.6, 0.7, 0.8, 0.9)$, and, for $\gamma = 0.7$, we set the planet rotation rate Ω and radius a to Earth values Ω_e and a_e and values two and four times larger. In these simulations, the Newtonian relaxation times are $\tau_i = 50\,\text{days}$ in the interior atmosphere and $\tau_s = 7\,\text{days}$ at the surface in low latitudes. In another set of simulation series, we used a spatially constant Newtonian relaxation time ($\tau_s = \tau_i = \tau$) and set it to values $\tau = (12.5, 25, 50, 100, 200)$ days. The hyperviscosity is chosen such that the smallest resolved scale is damped on a timescale of 12 hours in all simulations, except in the series with constant relaxation times, in which the damping timescale is 2.4 hours.

For each setting of γ, a, Ω, and τ, the pole-equator radiative-equilibrium temperature contrast Δ_h is varied over a wide range (Table A.1). The lowest radiative-equilibrium temperature contrasts are omitted for the larger planet radii to keep the lowest value of Δ_h/a, a measure of the baroclinicity of the radiative-equilibrium state, the same for the different planet radii.

For this study, we have omitted some simulations presented in SW06, SW08, and SM09. Those papers include thirteen simulations with lower radiative-equilibrium temperature contrasts Δ_h. The mean flows of at least six of the thirteen are linearly unstable, but because the growth rates are small, the unstable waves may not be

Series	Δ_h (K)
γ = (0.6, 0.7, 0.8, 0.9)	22.5, 30, 45, 60, ..., 180, 210, ..., 300, 360
$2\Omega_e$	22.5, 30, 45, 60, ..., 180, 210, ..., 300, 360
$4\Omega_e$	30, 60, 90, ..., 300, 360
$2a_e$	45, 60, ..., 180, 210, ..., 300, 360
$4a_e$	90, 120, ..., 300, 360
τ = (12.5, 25, 50, 100, 200) days	60, 90, ..., 300, 330, 360

Table A.1. Values of Δ_h for each of the series of simulations for which a linear stability analysis is presented.

well resolved by our linearization method; the remainder may or may not be linearly unstable. Also, a series of simulations with the convection scheme relaxing temperature profiles toward dry adiabats ($\gamma = 1.0$) is omitted because the mean thermal stratifications are statically unstable in low latitudes, which prevents an accurate determination of the most unstable waves. Finally, a series of simulations with lower roughness length has been omitted. In total, we present the results of linear stability analyses for 175 of the 223 mean flows of the nonlinear simulations.

A.3.3 Linear stability analysis

Linear waves are calculated by perturbing one zonal wavenumber at a time, only allowing the spectral coefficients of the perturbed zonal wavenumber to evolve in time, and keeping the amplitude of the growing wave small by rescaling the wave when it reaches a threshold amplitude. For example, the time-tendency of temperature has nonlinear advection terms such as the meridional advection of temperature,

$$\begin{aligned} \frac{\partial T}{\partial t} &= -v\,\frac{\partial T}{\partial y} + ..., \\ &= -\overline{v}\,\frac{\partial \overline{T}}{\partial y} - \overline{v}\,\frac{\partial T'}{\partial y} - v'\,\frac{\partial \overline{T}}{\partial y} - v'\,\frac{\partial T'}{\partial y} + \ldots, \end{aligned} \tag{A.5}$$

which is replaced with

$$\frac{\partial T'}{\partial t} = -\overline{v}\,\frac{\partial T'}{\partial y} - v'\,\frac{\partial \overline{T}}{\partial y} + \ldots, \tag{A.6}$$

where bars indicate zonal means and primes deviations therefrom. (The equations are written here in Cartesian geometry for simplicity, but the GCM has spherical geometry.) The linear stability calculation is integrated for 33 days, and growth rates are determined from the last 6 days of the integration; further details of the initialization procedure, time evolution, and sensitivities to parameters are discussed in appendix B.

The turbulent boundary layer scheme in the nonlinear simulations is replaced with Rayleigh drag for the linear calculations (cf. Hall and Sardeshmukh 1998; Held and Suarez 1994). The Rayleigh drag acts on the horizontal velocities with a coefficient k_R that decreases linearly in the model's sigma coordinate from a maximum of $k_0 = 2\,\mathrm{day}^{-1}$ (i.e., a timescale of half a day) at the surface to zero at $\sigma_b = 0.85$ and above,

$$k_R = k_0 \max\left(0, \frac{\sigma - \sigma_b}{1 - \sigma_b}\right). \tag{A.7}$$

The Rayleigh drag coefficient k_0 is chosen to be approximately equal to the drag coefficient inferred from the nonlinear simulations if one assumes the zonal momentum is in Ekman balance in the extratropical boundary layer; it is the same in all linear calculations.

In the linear analyses, we use the same Newtonian relaxation of temperatures as in the nonlinear simulations. The sensitivity of the linear waves to the diabatic forcing and Rayleigh drag time scale is discussed in appendix B. Because the zonal mean is held fixed, the mechanical and thermal forcing and hyperviscosity in the linear stability calculations act exclusively on the waves.

The convection scheme is not used for our linear stability analysis as convection is a finite-amplitude effect. However, the convection scheme indirectly enters the analysis through its impact on the mean flows of the nonlinear simulations about which we linearize.

For the time- and zonal-mean flows in statistically steady states of the nonlinear simulations, we determined growth rates of linear waves for several zonal wavenumbers (Fig. A.1). Fluxes of heat and momentum associated with the linearly most

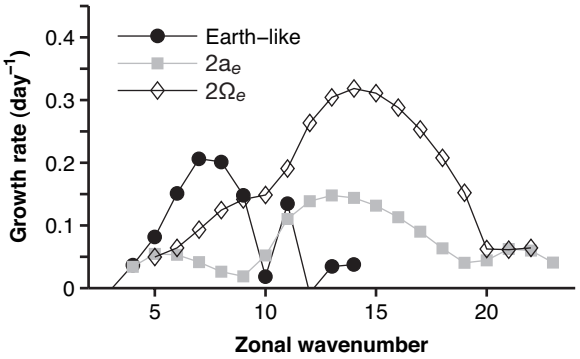

Figure A.1. Growth rate vs wavenumber of an Earth-like mean flow ($\Delta_h = 120\,\mathrm{K}$, $\gamma = 0.7$) and for mean flows with the same radiation and convection parameters but doubled radius or rotation rate.

unstable waves (Fig. A.2a,c) have smaller meridional extent than those associated with fully developed nonlinear eddies (Fig. A.2b,d). These differences in the structure of eddy fluxes occur in all simulations. Also, the eddy momentum flux divergence has a near-surface maximum that is not present in the fully developed nonlinear flow. This is consistent with earlier studies (e.g., Gall 1976a; Simmons and Hoskins 1976). The magnitudes of the potential temperature and momentum fluxes of the linear waves obey the same scaling laws presented in SW08 for nonlinear eddies, but with different constants of proportionality because of larger correlation coefficients between fluctuating flow fields in the linear waves.

A.4 Eddy length scales

The Rossby radius is a mean-field estimate of the length of the linearly most unstable baroclinic wave. We define the Rossby radius as

$$L_R = c_R \frac{N_p \left(\bar{p}_s - \bar{p}_t\right)}{f},$$

where c_R is an empirical order-one constant, $\bar{p}_s$ is the mean surface pressure, $\bar{p}_t$ is the mean tropopause pressure, f is the Coriolis parameter, and $N_p^2 = -(\bar{\rho}_s \bar{\theta}_s)^{-1}\, \overline{\partial_p \theta}^s$

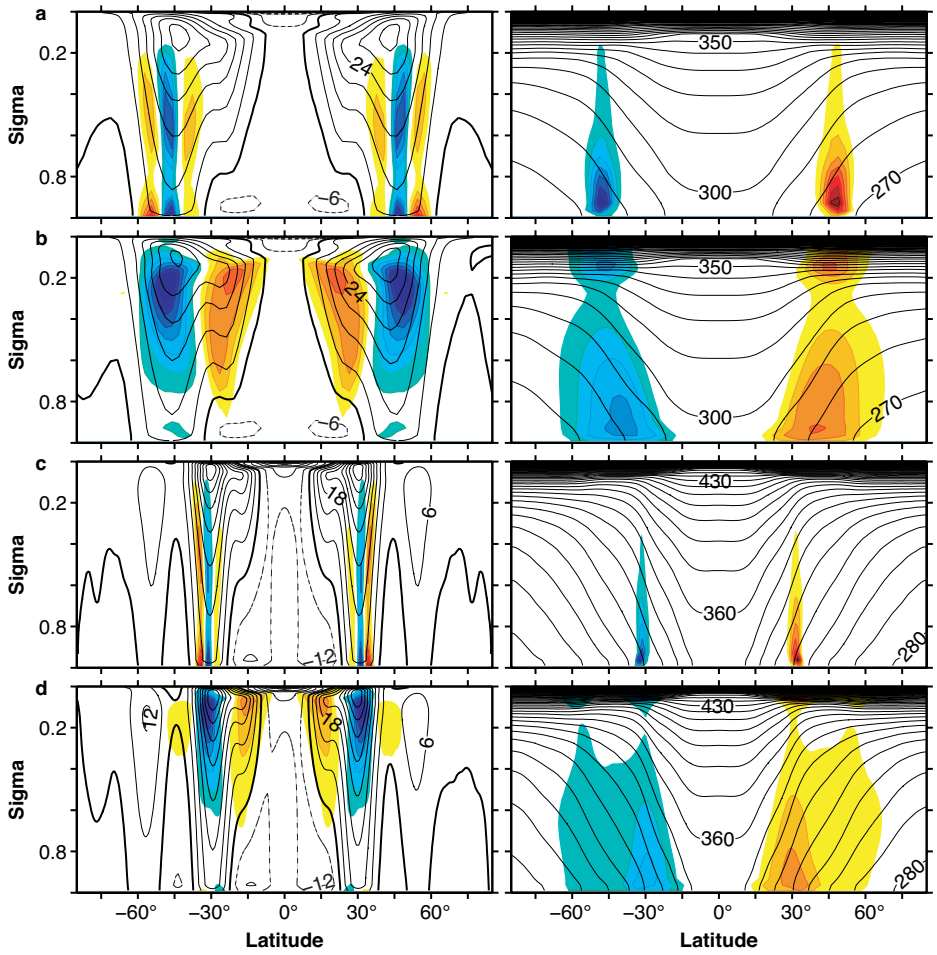

Figure A.2. Left column: Mean zonal wind (contours) and eddy momentum flux divergence (colors). Right column: Mean potential temperature (contours) and eddy potential temperature flux (colors). (a) Eddy fluxes associated with the most unstable wave of a simulation with Earth radius and rotation rate and $\Delta_h = 90\,\mathrm{K}$, $\gamma = 0.7$. (b) Eddy fluxes from the nonlinear simulation corresponding to (a) with contour interval 4.1×10^{-6} m s^{-2} for the eddy momentum flux divergence and 5.4 K m s^{-1} for the potential temperature flux. (c) Eddy fluxes associated with the most unstable wave of a simulation with $\Omega = 4\Omega_e$, $\Delta_h = 180\,\mathrm{K}$, and $\gamma = 0.7$. (d) Eddy fluxes from the nonlinear simulation corresponding to (c) with contour interval 1.6×10^{-5} m s^{-2} for the eddy momentum flux divergence and 11.6 K m s^{-1} for the potential temperature flux. Amplitudes of linear eddy fluxes are arbitrary; however, the color scale is chosen to show 8 contours of eddy momentum flux divergence and of eddy potential temperature flux for linear waves and nonlinear eddies. The slight differences in the mean fields are due to the hemispheric averaging performed prior to the linear stability analyses. (b) and (d) are adapted from Fig. 1 in SW08.

is a static stability measure, evaluated near the surface.[1] Using near-surface averages is empirically appropriate as the linear waves have large amplitude in the lower troposphere (see Fig. A.2).

We express length scales L in terms of zonal wavenumbers $m = a\cos\ \phi/L$. Our focus is on zonal wavenumbers because this is the quantity that we control when performing the linear stability analysis (see appendix B for details). The meridional scale of the most unstable linear waves may decouple from the zonal scale either by filling the domain as in, for example, the Eady problem (e.g., Vallis 2006, p. 274) or by being constrained by the structure of the mean flow. Consequently, the growing linear waves generally are not isotropic, unlike fully developed nonlinear eddies [see Held (1999) for a discussion of these points].

The first row of Fig. A.3 shows that the Rossby radius, with empirical constant $c_R = 0.8$, approximately accounts for the zonal length scale of the linearly most unstable waves. In Fig. A.3, the Rossby radius is evaluated at the latitude of maximum near-surface ($\sigma = 0.84$) eddy flux of potential temperature $\overline{v'\theta'}\cos(\phi)$ (hereafter, "potential temperature flux") in the nonlinear simulations. This maximum generally occurs in the baroclinic zone and jet closest to the equator if there are several jets in each hemisphere. Evaluating the Rossby radius at the latitude of the maximum potential temperature flux of the linear waves gives similar results.

The linearly most unstable waves generally have largest amplitude near the center or somewhat poleward of the baroclinic zone closest to the equator [as in Valdes and Hoskins (1988)]. There are a few simulations with multiple baroclinic zones for which the most unstable waves have largest amplitude in baroclinic zones in higher latitudes. Leaving those aside, the first row of Fig. A.3 demonstrates that, over a wide range of mean flows simulated in a primitive-equation model, the local Rossby radius in the baroclinic zone closest to the equator accounts for the length scale of the linearly most unstable waves. However, this does not imply that the local Rossby radius predicts the linearly most unstable length scale latitude-by-latitude. The initial value problem

[1] This formulation is similar to that in SW06, though we have omitted the supercriticality factor that appeared there. Including the supercriticality factor does not significantly affect Fig. A.3.

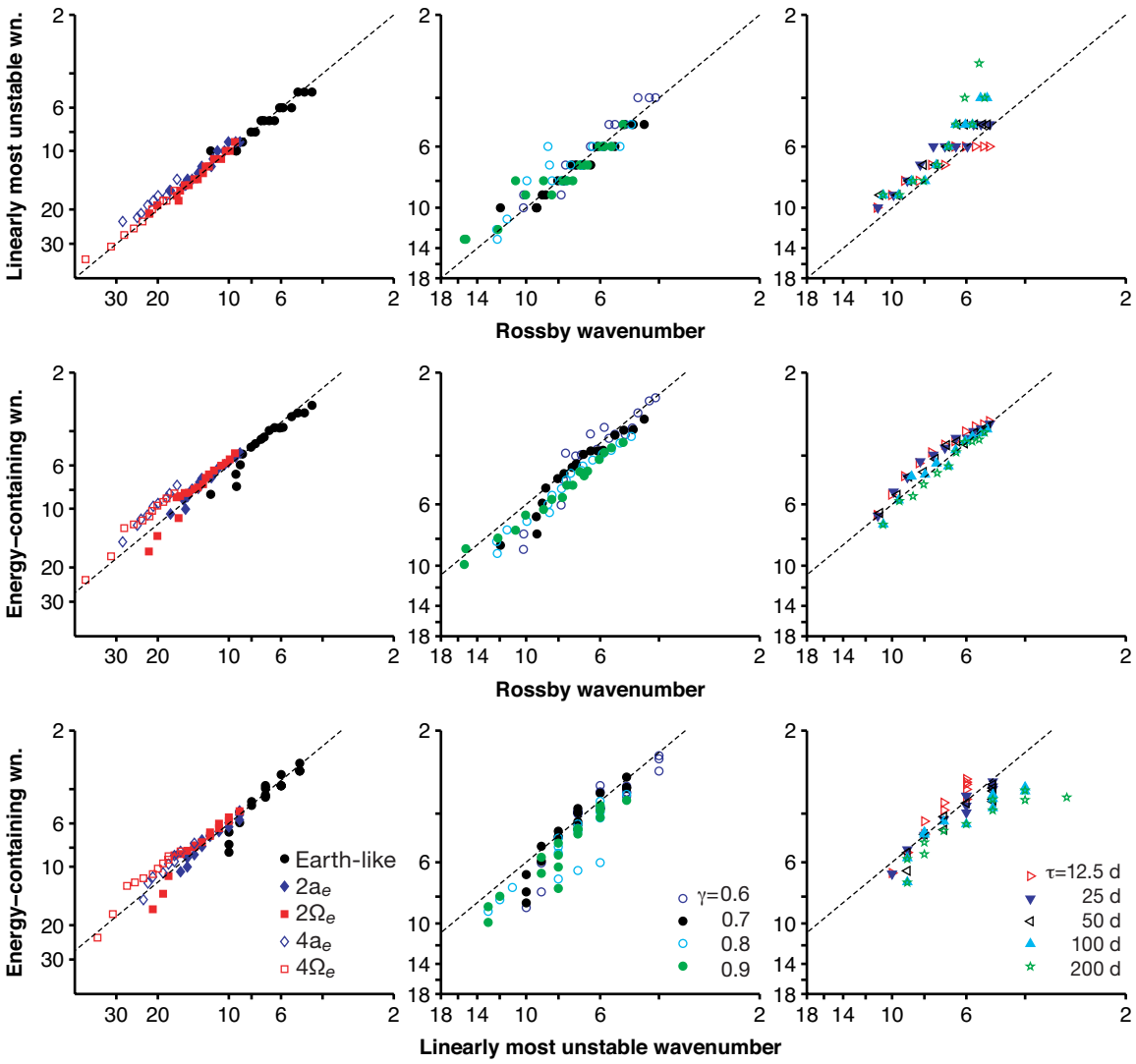

Figure A.3. Top row: Linearly most unstable wavenumber vs Rossby wavenumber with dashed line showing $m_l = m_R$. Middle row: energy-containing wavenumber vs Rossby wavenumber with dashed line showing $m_e = 0.6m_R$. Bottom row: energy-containing wavenumber vs linearly most unstable wavenumber with dashed line showing $m_e = 0.6m_l$. Left column: simulations with varying radius and rotation rate. Middle column: simulations with varying convective lapse rate. Right column: simulations with varying relaxation time scale. The axes are logarithmic.

technique that we use for computing linear waves does not allow us the determine the most unstable waves as a function of latitude.

It was shown in SW06 and SM09 that the energy-containing spherical wavenumber is similar to the Rossby wavenumber over the range of simulations. An exception

occurred when the Rossby wavenumber became smaller than the energy-containing wavenumber at large eddy lengths, which SW06 interpreted as a domain-size limitation for the eddy length. Here, we are comparing *zonal* eddy scales, so we revisit the relationship between the Rossby radius and the energy-containing zonal eddy length scale of the nonlinear simulations.

The second row of Fig. A.3 shows that the energy-containing zonal wavenumber is close to the Rossby wavenumber over the entire range of simulations. The scaling also holds at low wavenumbers (large length scales) where the Rossby wavenumber became smaller than the energy-containing spherical wavenumber in the nonlinear simulations.

The third row of Fig. A.3 shows that the energy-containing wavenumber of the nonlinear simulations, evaluated at the latitude of maximum potential temperature flux in the nonlinear simulations, is similar to the wavenumber of the linearly most unstable wave. The dashed lines in these panels have slopes of 0.6: the most unstable wavenumber is generally larger than the energy-containing wavenumber. In terms of eddy lengths, the length scale of the most unstable wave is about 40% smaller than the typical eddy length of the corresponding nonlinear simulation. Unlike in the analyses of SW06, there are no free parameters in the relation between these length scales, demonstrating unambiguously that the length scale of the most unstable wave and the energy-containing zonal length scale in the nonlinear simulations differ only by an $O(1)$ factor.

One degree of freedom is the latitude at which the energy-containing wavenumber is evaluated. Using the latitude of maximum potential temperature flux for the most unstable linear wave (instead of the nonlinear simulation) gives similar results. However, the difference between the latitude of the linear waves and the nonlinear eddies varies systematically with temperature gradients. This introduces some dependence on the temperature gradient in the relationship between the linearly most unstable wavenumber and the energy-containing wavenumber.

Some have suggested that the conversion from eddy available potential energy to eddy kinetic energy is a more relevant metric for equilibrated eddies than growth rates

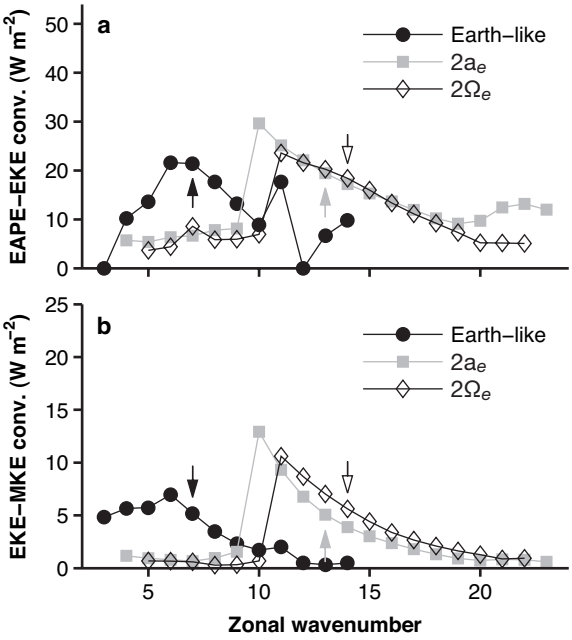

Figure A.4. (a) Conversion of eddy potential energy to eddy kinetic energy vs wavenumber. (b) Conversion of eddy kinetic energy to mean kinetic energy vs wavenumber. These are the same linear waves as in Fig. A.1 with arrows indicating the wavenumber with largest growth rate. The energy conversions are calculated for equal amplitude waves (i.e., the growth rate dependence has been removed).

because waves that convert more available energy to kinetic energy may attain greater amplitudes (e.g., Schneider 1981; Smith 2007). Changing to an energy conversion metric moves the dominant eddy scale to somewhat larger lengths for some of the mean flows (Fig. A.4).[2] The wavenumber of maximum energy conversion is typically 10–20% smaller than the linearly most unstable wavenumber. This shifts the linear wavenumber closer to the nonlinear energy-containing wavenumber, though there is still at least a 20% difference.

The conversion of eddy kinetic energy to mean kinetic energy (a 'sink' of eddy energy) should be considered for analogous reasons: the waves that lose more energy to the mean flow may not achieve as large an amplitude as those that transfer less. Energy conversion vs wavenumber curves have similar shapes for both eddy potential

[2]The energy conversions in Fig. A.4 are calculated using standard definitions (e.g., Lorenz 1955; Peixoto and Oort 1992). The conversion between eddy and mean kinetic energy owing to the vertical eddy flux of meridional momentum ($\overline{\omega' v'} \partial_p \overline{v}$) is omitted, consistent with quasigeostrophic scaling.

to eddy kinetic energy (Fig. A.4a) and eddy to mean kinetic energy (Fig. A.4b). The reason for this commonality is that both curves are controlled by the relative height and meridional scales of the waves. These two terms do not close the energy budget (note the different axis scales in Fig. A.4), as there is small-scale dissipation and, more importantly, the eddy kinetic energy is growing exponentially in time.

The meridional length scales of the linear waves are of the same magnitude as the zonal length scales. Using meridional wavenumbers defined by $n_e - m$ (e.g., Shepherd 1987a), where n_e is the energy-containing spherical wavenumber of the linear waves determined as in SW06 and m is their zonal wavenumber, the meridional wavenumber is usually within a factor of two of the zonal wavenumber. However, the zonal and meridional wavenumbers do not necessarily vary together. In the nonlinear simulations, the meridional wavenumber asymptotes to $\sim$3, while the zonal wavenumber continuously decreases with increasing temperature gradients (Fig. A.3). This supports the interpretation of SW06 that the Rossby wavenumber becomes smaller than the spherical energy-containing wavenumber because the domain-size limits the meridional eddy length scale.

A.5 Eddy time scales

The Eady growth rate,

$$\sigma \sim (f/N)\ \partial_z \bar{u}\ ,$$

is a time scale that emerges in quasigeostrophic theories of baroclinic instability such as the Eady and Charney problems (Lindzen and Farrell 1980; Vallis 2006). An alternative mean-field estimate for eddy time scales is proportional to the square root of mean available potential energy (MAPE), which scales like the Eady growth rate (e.g., O'Gorman and Schneider 2008a). This connects the timescale of linear waves to the eddy kinetic energy in the nonlinear simulations, in which the eddy kinetic energy is similar to (dry) MAPE over a wide range of both moist and dry climates (SW08, O'Gorman and Schneider 2008a).

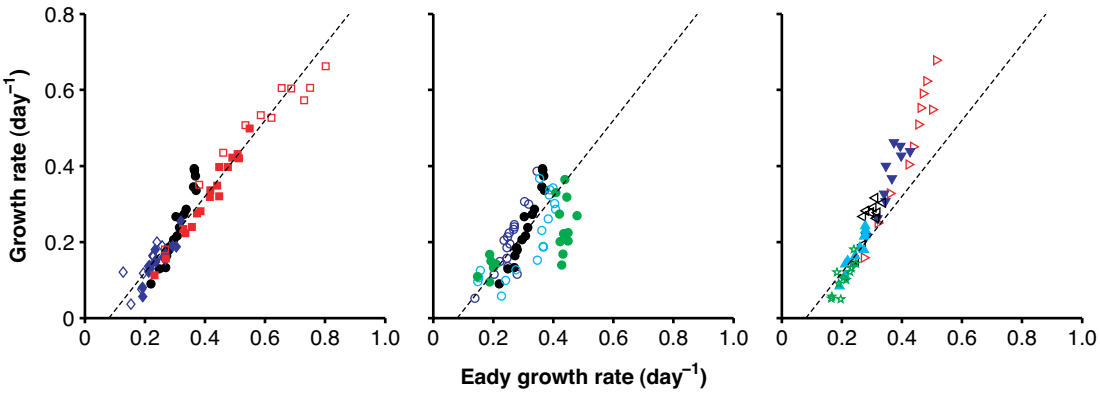

Figure A.5. Linearly most unstable growth rate vs Eady growth rate. The Eady growth rate is scaled by 0.16, a factor determined by least-squares regression of all simulations. The dashed line has intercept -0.08. Plotting symbols as in Fig. A.3.

We compare the Eady growth rate averaged over the latitudes of the most unstable wave (determined by where the potential temperature flux is within 70% of its maximum) and over a near-surface layer (between $\sigma = 0.8$ and 0.7) to the growth rate of the linear waves in Fig. A.5. The series of simulations with varying rotation rate and radius (left panel) and constant relaxation time (right panel) have compact scaling relations. The series of simulations with varying convective lapse rates have significant scatter, though for a given value of γ, there is generally a monotonic relation between the mean-field estimate and the actual growth rate of the most unstable wave. Evaluating the Eady growth rate between $\sigma = 0.7$ and $\sigma = 0.6$ does not significantly change the results in Fig. A.5.

The actual growth rate tends to zero and the mean flows may become baroclinically neutral at low temperature gradients; however, the Eady growth rates remain finite, which causes a non-origin intercept of the regression lines between the actual and Eady growth rates. There are several possibilities why this occurs. First, the relationship between the Eady and actual growth rates may not be linear in the weakly unstable limit, or the actual growth rate depends on boundary layer damping (Fig. A.9), whereas the Eady growth rate does not. Second, our method of calculating linear waves by integrating for a fixed time may fail to capture waves that have small but non-negative growth rates. Third, the GCM's vertical discretization of the prim-

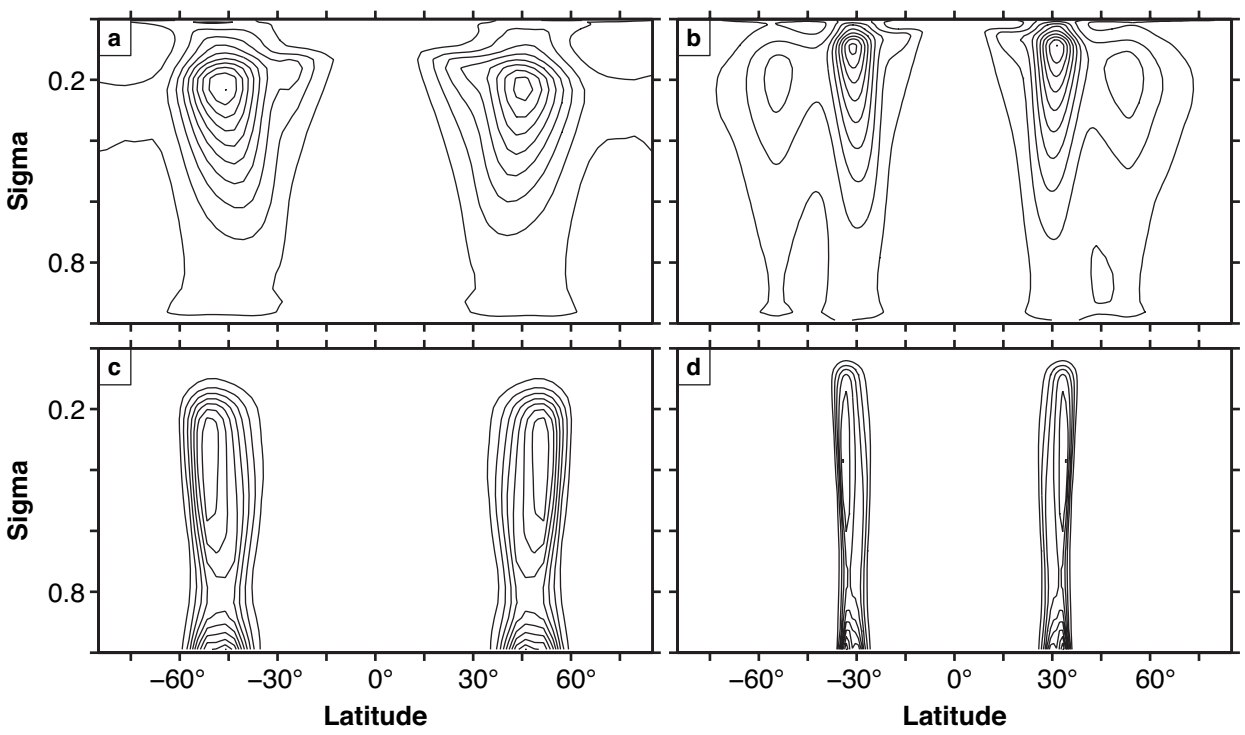

Figure A.6. Eddy kinetic energy of (a and b) nonlinear simulations and (c and d) linearly most unstable wave for the same simulations as in Fig. A.2. The contour interval is 10% of the maximum.

itive equations is equivalent to replacing the continuous dependence on the vertical coordinate with a discrete set of interacting layers. This may introduce a spurious non-zero critical shear for instability, as in, for example, the two-layer model (e.g., Vallis 2006). Fourth, the zonal-mean flow may undergo time variations such that it is linearly unstable at certain times but neutral at others. A final possibility is that non-modal eddy growth is an important mechanism for generating transient eddies in simulations with weak temperature gradients.

A.6 Eddy energies

The eddy kinetic energy (EKE) of the most unstable waves is more meridionally confined than that of the nonlinear eddies (Fig. A.6), as was the case for the eddy fluxes in Fig. A.2. The secondary maximum of EKE near the surface is another difference

between the linear waves and nonlinear eddies. Because the linear calculations include boundary layer damping of the same magnitude as the nonlinear simulations, the near-surface maxima of EKE of the linear waves are not directly the result of missing damping of the waves; rather, they are indicative of nonlinear modifications of the eddies in the nonlinear simulations, as has been noted by earlier investigators (Gall 1976a; Simmons and Hoskins 1976).

The EKE structure of linear waves changes compared to the most unstable wave (Fig. A.6) for waves with different wavenumbers. At higher wavenumbers (shorter wavelengths), the upper tropospheric EKE maximum disappears as the vertical extent of the waves shrinks until they are confined to a shallow layer just above the surface (Held 1978). At lower wavenumbers (longer wavelengths), the structure is generally similar to the most unstable wave, with some meridional broadening and deepening in the vertical. Similar changes occur for eddy potential temperature fluxes and for eddy momentum fluxes.

The partitioning between forms of eddy energies provides a way of determining the degree to which nonlinear interactions are energetically important: in the presence of an inverse cascade of eddy energy, baroclinic EKE is much smaller than the barotropic EKE and eddy available potential energy (EAPE) (Held and Larichev 1996). For the set of simulations examined here, SW08 showed that both barotropic and baroclinic eddy kinetic energies are equipartitioned with the eddy available potential energy (i.e., they all scale linearly with each other). Here, we examine the same partitionings for linear waves in the absence of nonlinear interactions.

For the linearly most unstable waves, Fig. A.7 shows the partitionings between barotropic EKE ($\mathrm{EKE_{bt}}$) and EAPE, on the one hand, and between baroclinic EKE ($\mathrm{EKE_{bc}}$) and EAPE, on the other hand. The corresponding plots for the nonlinear simulations appear in SW08 (their Figs. 5 and 6). As in the nonlinear case, the most unstable waves have equipartitioned eddy energies. The constants of proportionality in the figures here are the same as well ($\mathrm{EAPE/EKE_{bt}} \approx 1$ and $\mathrm{EAPE/EKE_{bc}} \approx 2.25$), suggesting that nonlinear interactions do not significantly modify the energy partitioning of eddies. Some of the deviations from this linear scaling (e.g., the linear

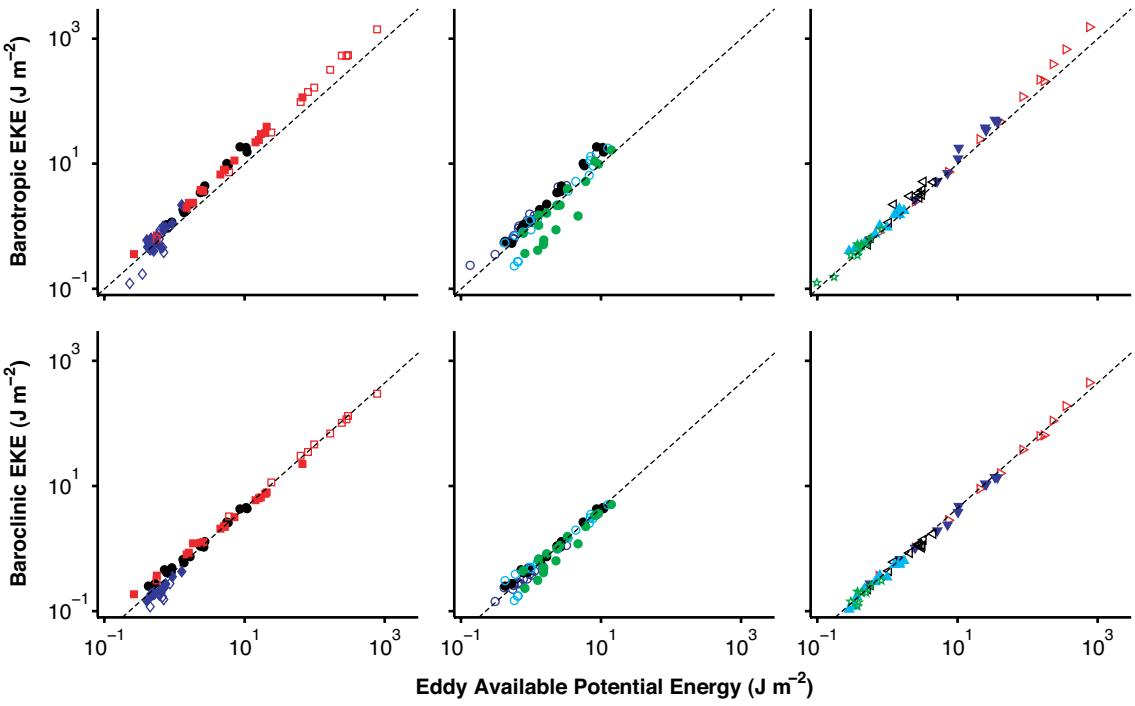

Figure A.7. Top row: Barotropic eddy kinetic energy vs eddy available potential energy for the linearly most unstable wave. Dashed line is $\mathrm{EKE_{bt}} = \mathrm{EAPE}$. Bottom row: Baroclinic eddy kinetic energy vs eddy available potential energy for the linearly most unstable wave. Dashed line is $2.25\ \mathrm{EKE_{bc}} = \mathrm{EAPE}$. Plotting symbols as in Fig. A.3.

waves for $a = 4a_e$ and $\gamma = 0.9$ that have $\mathrm{EAPE/EKE_{bt}} > 1$) are due to mean flows with multiple jets that have linearly most unstable waves with maximum amplitude at higher-latitude jets (e.g., the most unstable waves are not located in the baroclinic zone closest to the equator); this jet dependence of energy partitionings also occurs in nonlinear simulations (O'Gorman and Schneider 2008c, their Fig. 13).

Examining the variations of these relations for linear waves of different wavenumbers (Fig. A.8) shows that there is a range of order-one ratios of eddy energies. These variations are consistent with the different wave structures at different wavelengths described above, so the constants of proportionality are not a general property of linear waves. However, they may be universal for the most unstable waves: the ratios for the most unstable waves (marked by arrows in Fig. A.8) are similar to the ratios for the nonlinear simulations (marked by the dashed line in Fig. A.8).

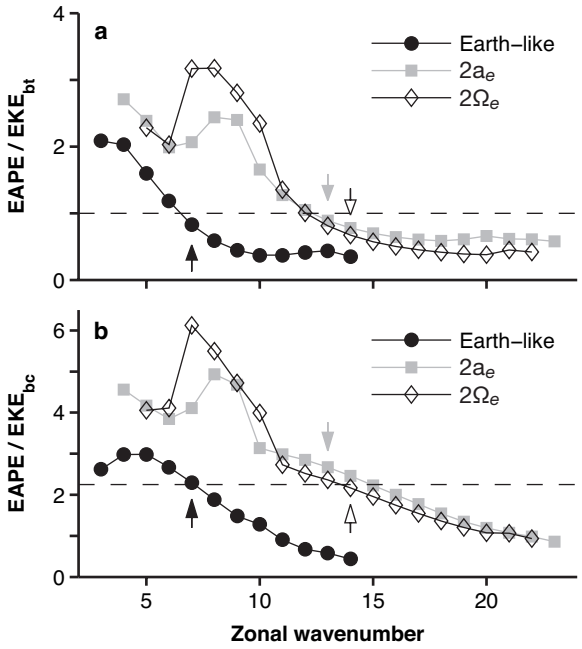

Figure A.8. Ratio of eddy energies for linear waves of different wavenumbers for the same mean flows as in Fig. A.1. (a) Eddy available potential energy over barotropic eddy kinetic energy, with dashed line EAPE = $\mathrm{EKE_{bt}}$ as in top row of Fig. A.7. (b) Eddy available potential energy over baroclinic eddy kinetic energy, with dashed line EAPE = 2.25 $\mathrm{EKE_{bc}}$ as in bottom row of Fig. A.7. Arrows indicate the wavenumber with the largest growth rate.

Thus, the energy partitioning coefficients of the eddies in the nonlinear simulations can approximately be accounted for by those of the linearly most unstable waves. The approximate equality of the energy partitioning coefficients for the linearly most unstable waves and nonlinear eddies demonstrates that nonlinear modifications of eddies are not essential for the energetics of eddies. In particular, they are further evidence that no substantial inverse cascade of eddy energy is occurring in the nonlinear simulations. However, the linear waves do not reveal clear dependences on radius and rotation rate for the ratio of baroclinic eddy kinetic energy to eddy available potential energy, such as were seen in the nonlinear simulations (SW08).

A.7 Conclusions

We have presented the results of linear stability analyses for most of the mean flows of the simulations in SW06, SW08, and SM09, excluding a few simulations with low temperature gradients and small or possibly zero growth rates of baroclinic instability. The analyses demonstrate that the mean flows are generally baroclinically unstable and are not in a state of baroclinic adjustment.

The zonal length scale of the linearly most unstable waves is similar to the Rossby radius. The zonal length scale of the dominant linear waves is close to but somewhat smaller than (between 40% and 20%, depending on ordering conventions of linear waves) the zonal length scale of the energy-containing eddies in the corresponding nonlinear simulations. Their growth rates are similar to the Eady growth rate, but the scaling is not generally linear and may have a dependence on external parameters. The agreement between scales of linear waves and mean-field estimates of these scales demonstrates that the mean-field estimates based on idealized quasigeostrophic models can be used for a wide range of complex flows in a primitive-equation model. The partitionings among eddy available potential energy and barotropic and baroclinic eddy kinetic energies in linear waves are also similar to those in the nonlinear eddies. Confirming the analysis in SW06, these results show that there is no substantial inverse cascade of eddy energy over a range of dry atmospheric circulations that vary from weakly to strongly unstable and include simulations with multiple jets in each hemisphere. However, the differences between linear waves and nonlinear eddies that do exist point to aspects of atmospheric macroturbulence that are modified by (weak) nonlinear eddy-eddy interactions. Particularly notable among those are modifications of the meridional scales of nonlinear eddies and of the structure of second-order quantities such as eddy momentum and heat fluxes—as was shown, for a more limited set of mean flows, by Simmons and Hoskins (1978) and others.

For simple (energy-balance) climate models in which the effects of large-scale eddies are not resolved explicitly but are represented parametrically, the results here, together with those in SW06, SW08, and SM09, imply that linear stability calcula-

tions can give approximations of zonal length scales and partitionings among eddy energies. However, it will be necessary to find a way to represent weak nonlinear eddy-eddy interactions in such models to obtain accurate representations of the structure of second-order quantities such as eddy fluxes.

A.8 Acknowledgments

We thank Chris Walker for performing most of the nonlinear simulations and Simona Bordoni and Paul O'Gorman for helpful comments and discussions. T.M. Merlis is supported by a National Defense Science and Engineering Graduate Fellowship. The linear stability analyses were performed on Caltech's Division of Geological and Planetary Sciences Dell cluster. The program code for the simulations, based on the Flexible Modeling System of the Geophysical Fluid Dynamics Laboratory, as well as the simulation results themselves are available from the authors upon request.

A.9 Appendix A: Determination of Growth Rate

For each of the prognostic variables (vorticity ζ, divergence δ, temperature, and the logarithm of surface pressure), the root-mean-square of the perturbed zonal spectral coefficients averaged over levels ([ ]) and meridional ({}) dimensions is calculated:

$$\Psi_{\text{rms}} = \sqrt{\{[\text{Re}(\hat{\Psi})^2 + \text{Im}(\hat{\Psi})^2]\}}. \tag{A.8}$$

The four prognostic variables are summed with the following weights to account for their different magnitudes:

$$Q = \frac{\zeta_{\text{rms}}}{\zeta_0} + \frac{\delta_{\text{rms}}}{\delta_0} + \frac{T_{\text{rms}}}{T_0} + \frac{(\log p_s)_{\text{rms}}}{\log p_0}, \tag{A.9}$$

with $\zeta_0 = 10^{-5}\,\text{s}^{-1}$, $\delta_0 = 10^{-5}\,\text{s}^{-1}$, $T_0 = 1\,\text{K}$, and $\log p_0 = 300\,\text{Pa}$.

The growth rate is then

$$r = \frac{1}{\Delta t} \log \left(\frac{Q(t)}{Q(t - \Delta t)} \right), \tag{A.10}$$

where $\Delta t = 1$ day (using 2 days or 0.5 days gives similar results). Other ways of determining the growth rate (e.g., Simmons and Hoskins 1976; Hall and Sardeshmukh 1998) give similar results. The daily growth rate is averaged over the last 6 days of the linear stability calculation.

We found some linear waves had oscillatory growth rates. This typically occurred for short wavelengths (large wavenumbers), and as a result, generally these had growth rates well below those of the most unstable waves. In a handful of cases, the maximum growth rate attained over the course of the oscillation would be larger than the (steady) growth rate of the most unstable wave. For this reason, we use the growth rate averaged over 6 days instead of the growth rate averaged over 1 day. This choice changes the most unstable wavenumber in less than 5% of the mean flows we analyzed, so none of the results or conclusions depend on it. It is unclear what causes the oscillatory growth rates. However, after sufficient time (~ 200 days in some cases), the oscillations decay and leave a steady growth rate.

A.10 Appendix B: Details of the Linear GCM

We linearize the GFDL spectral dynamical core about the time, zonal, and hemispheric mean of the last (100, 25, 10) days of the horizontal resolution (T42, T85, T127) simulations in SW06, SW08, and SM09. The dynamical core of the GCM is modified in two ways to ensure linearity. Following Simmons and Hoskins (1976), only the spectral coefficients of the perturbed zonal wavenumber are advanced forward in time, and the growing wave is kept at small amplitude by re-scaling. The re-scaling is performed when the maximum surface pressure deviation grows to 10 Pa, at which point it is reduced to 1 Pa; many alternative re-scaling criteria are possible and give similar results. The baroclinic wave is initialized by perturbing the odd meridional

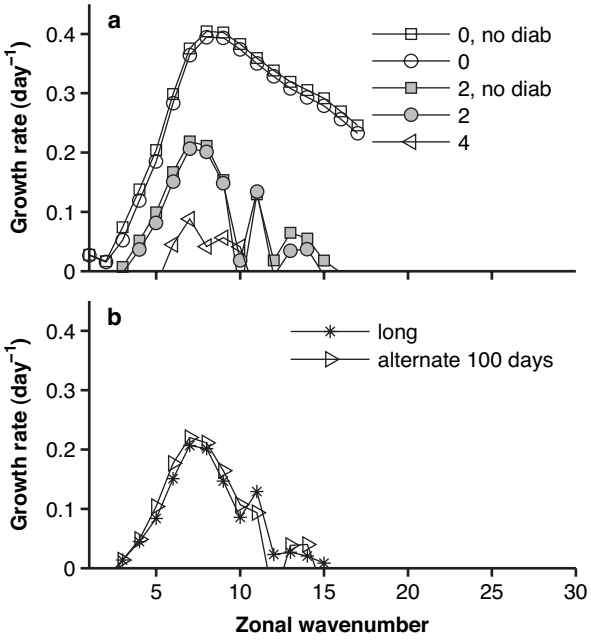

Figure A.9. (a) Sensitivity of growth rates to Rayleigh drag and Newtonian relaxation. Numbers in legend refer to damping coefficient in units day^{-1} (e.g., 0 day^{-1} has no boundary layer damping), and 'no diab' has a much larger Newtonian relaxation timescale. (b) 'long' linear stability analysis, which was integrated for 58 instead of 33 days, and a linear stability analysis of a different 100-day average mean flow of the same nonlinear simulation.

spectral coefficients of vorticity between wavenumbers 3 and 39 equally at all model levels, which ensures hemispheric symmetry. Time is discretized using a second-order leapfrog method, so the perturbation is added to both initial time-steps. The initial perturbation is not geostrophically balanced, but the model is integrated for sufficient time to ensure geostrophic adjustment has occurred by the time quantities are measured. The linear model is run for 33 days, at which point waves with typical growth rates have doubled in amplitude at least three times. Because the model is run for a fixed number of days independent of growth rate, more slowly growing waves may not be as accurately computed; however, experiments run for 58 days show little difference in structure or growth rate ('long' in Fig. A.9).

To determine how sensitive the linear waves are to the mechanical and diabatic forcing, we performed additional experiments with the Earth-like mean flow

(Fig. A.2a), in which we increased and decreased the boundary layer damping timescale and greatly reduced the diabatic forcing by increasing the relaxation timescale to 1.2×10^4 days uniformly in latitude and pressure. The sensitivity to boundary layer Rayleigh drag and Newtonian cooling is similar to that in Valdes and Hoskins (1988): mechanical damping in the boundary-layer neutralizes high-wavenumber instability, and there is little sensitivity to thermal forcing, consistent with Newtonian relaxation time scales generally being long compared with eddy time scales (Fig. A.9). We have also reduced the diabatic forcing for a linear stability calculation with the shortest relaxation time in the corresponding nonlinear simulations ($\tau = 12.5$ days); there was little sensitivity even in this strongly forced case.

We have performed additional nonlinear simulations in which the turbulent boundary layer scheme of the GCM was replaced with Rayleigh drag and have performed stability analyses of the resulting mean flows. In this case, where both the thermal and mechanical damping of the nonlinear and linear cases are identical, the mean flows are also generally baroclinically unstable. In linear stability analyses with small Rayleigh drag throughout the atmospheric column, as in Hall and Sardeshmukh (1998), the instability likewise is not neutralized, and the most unstable wavenumber is not significantly affected by the added drag.

A.11 Appendix C: Definitions of Eddy Scales

A.11.1 Energy-containing scale

The energy-containing wavenumber is estimated using a -2 moment of the zonal spectrum of eddy meridional kinetic energy,

$$m_e^2 = \frac{\sum_m E_m}{\sum_m m^{-2} E_m}, \tag{A.11}$$

evaluated at the latitude of maximum eddy potential temperature flux. This choice gives wavenumbers that are close to the maximum of the spectrum.

An alternative definition that is commonly used,

$$m_e = \frac{\sum_m m\ E_m}{\sum_m E_m}, \tag{A.12}$$

gives energy-containing wavenumbers that are larger than the maximum of the spectrum or the -2 moment because the spectrum of eddy meridional kinetic energy is asymmetric [see Frierson et al. (2006, their Fig. 14a) for a representative example]. This definition would lead to somewhat closer agreement with the linearly most unstable wavenumber ($m_e \sim 0.8 m_l$).

A.11.2 Rossby radius

The Rossby radius is computed using near-surface quantities:

$$L_R = c_R \frac{N_p \left(\bar{p}_s - \bar{p}_t\right)}{f}\,.$$

The zonal Rossby wavenumber is $m_R = a\cos(\phi_{\rm ref})/L_R$, where $\phi_{\rm ref}$ is the latitude of maximum eddy potential temperature flux as in the definition of energy-containing wavenumber. The constant $c_R = 0.8$ is chosen so that the Rossby wavenumbers are close to the wavenumbers of the most unstable waves. Including a supercriticality factor as in SW08 or in SW06 does not change Fig. A.3 significantly.

Appendix B

Atmospheric dynamics of Earth-like tidally locked aquaplanets

This chapter is a reproduction of Merlis and Schneider (2010).

B.1 Abstract

We present simulations of atmospheres of Earth-like aquaplanets that are tidally locked to their star, that is, planets whose orbital period is equal to the rotation period about their spin axis, so that one side always faces the star and the other side is always dark. Such simulations are of interest in the study of tidally locked terrestrial exoplanets and as illustrations of how planetary rotation and the insolation distribution shape climate. As extreme cases illustrating the effects of slow and rapid rotation, we consider planets with rotation periods equal to one current Earth year and one current Earth day. The dynamics responsible for the surface climate (e.g., winds, temperature, precipitation) and the general circulation of the atmosphere are discussed in light of existing theories of atmospheric circulations. For example, as expected from the increasing importance of Coriolis accelerations relative to inertial accelerations as the rotation rate increases, the winds are approximately isotropic and divergent at leading order in the slowly rotating atmosphere but are predominantly zonal and rotational in the rapidly rotating atmosphere. Free-atmospheric horizontal temperature variations in the slowly rotating atmosphere are generally weaker than in the rapidly rotating atmosphere. Interestingly, the surface temperature on the

night side of the planets does not fall below ∼240 K in either the rapidly or slowly rotating atmosphere; that is, heat transport from the day side to the night side of the planets efficiently reduces temperature contrasts in either case. Rotational waves and eddies shape the distribution of winds, temperature, and precipitation in the rapidly rotating atmosphere; in the slowly rotating atmosphere, these distributions are controlled by simpler divergent circulations. Both the slowly and rapidly rotating atmospheres exhibit equatorial superrotation. Systematic variation of the planetary rotation rate shows that the equatorial superrotation varies non-monotonically with rotation rate, whereas the surface temperature contrast between the day side and the night side does not vary strongly with changes in rotation rate.

B.2 Introduction

Planets generally evolve toward a state in which they become tidally locked to their star. Torques the star exerts on tidal bulges on a planet lead to an exchange between the spin angular momentum of the planetary rotation and orbital angular momentum of the planet's revolution around the star, such that the rotation period around the spin axis gradually approaches the orbital period of the planet (Hubbard 1984). (The spin angular momentum of the star may also participate in this angular momentum exchange.) This process reaches its tidally locked end state when the rotation period is equal to the orbital period, so that one side of the planet always faces the star and the other side is always dark. The time it takes to reach this end state may exceed the lifetime of the planetary system, so it may never be reached (this is the case for the Sun-Earth system). But planets that are close to their star can reach a tidally locked state more quickly. Such close planets in other solar systems are easier to detect than planets farther away from their star, and exoplanets that are believed to be tidally locked have indeed been detected in recent years (e.g., Charbonneau et al. 2000). Here we investigate the atmospheric dynamics of Earth-like tidally locked aquaplanets through simulations with a three-dimensional general circulation model (GCM). Our purpose is pedagogic: we contrast rapidly and slowly rotating tidally

locked Earth-like planets with each other and with Earth itself to illustrate the extent to which atmospheric dynamics depend on the insolation distribution and planetary rotation rate.

There are two areas of existing research on the atmospheric dynamics of tidally locked planets. First, there are several studies motivated by "hot Jupiters"—large, close-in planets that have been observed transiting a star (see Showman et al. (2010) for a review). Second, there are studies of Earth-like exoplanets closely orbiting a relatively cool star—planets that have not yet been but may be detected soon, for example, by NASA's recently launched *Kepler* space telescope or by ground-based telescopes (as demonstrated by the recent discoveries of Charbonneau et al. (2009)). Joshi et al. (1997) investigated the large-scale circulation of such Earth-like planets and explored how their climate depends on the mass of the atmosphere. And Joshi (2003) documented their hydrological cycle using an Earth climate model.

The studies by Joshi et al. provide a description of Earth-like tidally locked atmospheric circulations and how they depend on some parameters, such as the atmospheric mass. But some questions remain, among them: (i) How does the planet's rotation rate affect the circulation and climate? (ii) What controls the precipitation distribution (location of convergence zones)? (iii) What mechanisms generate large-scale features of the circulation, such as jets? (iv) What determines the atmospheric stratification?

We address these questions by simulating tidally locked Earth-like aquaplanets. We focus on simulations with rotation periods equal to one current Earth year and one current Earth day as two illustrative cases: The slowly rotating case corresponds roughly to the tidally locked end state Earth would reach if the Sun were not changing, that is, if the solar constant $S_0 = 1367$ Wm^{-2} remained fixed. The rapidly rotating case corresponds to a terrestrial planet sufficiently close to a cool host star, so that the orbital period is one Earth day but the average insolation reaching the planet still is $S_0 = 1367$ Wm^{-2}, as presently on Earth. Additionally, we explore more systematically how some characteristics—such as equatorial superrotation—depend on the planetary rotation rate.

B.3 General circulation model

We use an idealized atmosphere GCM with an active hydrological cycle and an aquaplanet (slab ocean) lower boundary condition. The slab ocean has the heat capacity of 5 m of water and has no explicit horizontal transports but is implicitly assumed to transport water from regions of net precipitation to regions of net evaporation, so that the local water supply is unlimited. The GCM is a modified version of the model described in O'Gorman and Schneider (2008b), which is similar to the model described in Frierson et al. (2006). Briefly, the GCM is a three-dimensional primitive-equation model of an ideal-gas atmosphere. It uses the spectral transform method in the horizontal, with resolution T85, and finite differences in $\sigma = p/p_s$ coordinates (pressure p and surface pressure p_s) in the vertical, with 30 unequally spaced levels; the time step is 200 s. Subgrid-scale dissipation is represented by an exponential cut-off filter (Smith et al. 2002), which acts on spherical wavenumbers greater than 40, with a damping timescale of 1 h on the smallest resolved scale. Most features of the simulated flows are similar at T42 resolution or with different subgrid-scale filters; exceptions are noted below.

The GCM has a surface with uniform albedo (0.38) and uniform roughness lengths for momentum fluxes (5×10^{-3} m) and for latent and sensible heat fluxes (10^{-5} m). It has a gray radiation scheme and a quasi-equilibrium moist convection scheme that relaxes convectively unstable atmospheric columns to a moist pseudo-adiabat with constant (70%) relative humidity (Frierson 2007). Only the vapor-liquid phase transition is taken into account, and the latent heat of vaporization is taken to be constant. No liquid water is retained in the atmosphere, so any precipitation that forms immediately falls to the surface. Radiative effects of clouds are not taken into account, except insofar as the surface albedo and radiative parameters are chosen to mimic some of the global-mean effects of clouds on Earth's radiative budgets.

Other model details can be found in O'Gorman and Schneider (2008b). However, the radiation scheme differs from that in O'Gorman and Schneider (2008b) and is described in what follows.

B.3.1 Tidally locked insolation

The top-of-atmosphere insolation is held fixed at the instantaneous value for a spherical planet (e.g., Hartmann 1994),

$$S_{\mathrm{TOA}} = S_0 \times \max\big(0, \cos(\phi)\cos(\lambda - \lambda_0)\big), \tag{B.1}$$

where ϕ is latitude and λ is longitude, with subsolar longitude $\lambda_0 = 270^\circ$ and solar constant $S_0 = 1367\ \mathrm{Wm}^{-2}$. There is no diurnal cycle of insolation. That is, we assume zero eccentricity of the orbit and zero obliquity of the spin axis.

Absorption of solar radiation in the atmosphere is represented by attenuation of the downward flux of radiation with an optical depth that varies quadratically with pressure, so that

$$S(p) = S_{\mathrm{TOA}} \exp\left[-\left(\frac{p}{p_0}\right)^2\right], \tag{B.2}$$

with $p_0 = 10^5\,\mathrm{Pa}$.

B.3.2 Longwave optical depth

O'Gorman and Schneider (2008b) used a gray radiation scheme with a longwave optical depth that was uniform in longitude and a prescribed function of latitude, thereby ignoring any longwave water vapor feedback. This is not adequate for tidally locked simulations in which the water vapor concentration varies strongly with longitude. Therefore, we use a longwave optical depth that varies with the local water vapor concentration (cf. Thuburn and Craig 2000), providing a crude representation of longwave water vapor feedback.

As in Frierson et al. (2006), the longwave optical depth τ has a term linear in pressure p, representing well-mixed absorbers like CO_2, and a term quartic in pressure, representing water vapor, an absorber with a scale height that is one-quarter of the pressure scale height,

$$\tau = \tau_0 \left(\frac{p}{p_0}\right)^4 + \tau_1 \left(\frac{p}{p_0}\right). \tag{B.3}$$

Here, $\tau_1 = 1.2$ and $p_0 = 10^5\,\mathrm{Pa}$ are constants. The optical thickness τ_0 is a function of the model's instantaneous column water vapor concentration,

$$\tau_0 = \frac{1}{p_1}\int_0^{p_s} r\,dp, \tag{B.4}$$

with water vapor mixing ratio r and an empirical constant $p_1 = 98\,\mathrm{Pa}$ to keep τ_0 order one for conditions typical of Earth.

We have also run simulations in which the absorptivity of the absorber representing water vapor depended locally on the specific humidity on each model level. The details of the radiation scheme such as the constants chosen and the exact dependence of the optical depth on the water vapor concentration affected quantitative aspects of the simulations (e.g., the precise surface temperatures obtained), but not the large-scale dynamics on which we focus. With or without a vertically-local dependence of absorptivity on the water vapor concentration, the simulated surface climate is similar to those presented in Joshi (2003), who used a more complete representation of radiation including radiative effects of clouds. This gives us confidence that the qualitative results presented here do not depend on the details of the radiation scheme.

B.3.3 Simulations

We conducted a rapidly rotating simulation with planetary rotation rate equal to that of present-day Earth, $\Omega = \Omega_E = 7.292 \times 10^{-5}\ \mathrm{s}^{-1}$, and a slowly rotating simulation with planetary rotation rate approximately equal to one present-day Earth year, $\Omega = \Omega_E/365$. The results we present are averages over the last 500 days of 4000-day simulations (with 1 day = 86400 s, irrespective of the planetary rotation rate). During the first 3000 days of the simulation, we adjusted the subgrid-scale dissipation parameters to the values stated above to ensure there was no energy build-up at the smallest resolved scales. The slowly rotating simulation is presented in section B.4, and the rapidly rotating simulation is presented in section B.5.

Additionally, we conducted simulations with intermediate rotation rates, to explore how equatorial superrotation and the day-side to night-side surface temperature

contrast depend on the rotation rate. The last 500 days of 2000-day simulations are presented in section B.6.

B.4 Slowly rotating simulation

The Rossby number $\mathrm{Ro} = U/(fL)$, with horizontal velocity scale U, Coriolis parameter f, and length scale L, is a measure of the importance of inertial accelerations ($\sim U^2/L$) relative to Coriolis accelerations ($\sim fU$) in the horizontal momentum equations. In rapidly rotating atmospheres, including Earth's, the Rossby number in the extratropics is small, and the dominant balance is geostrophic, that is, between pressure gradient forces and Coriolis forces. In slowly rotating atmospheres, the Rossby number may not be small. If $\mathrm{Ro} = O(1)$, inertial and Coriolis accelerations both are important, as in the deep tropics of Earth's atmosphere. If $\mathrm{Ro} \gg 1$, Coriolis accelerations and effects of planetary rotation become unimportant. In that case, there is no distinguished direction in the horizontal momentum equations, so the horizontal flow is expected to be isotropic, that is, the zonal velocity scale U and meridional velocity scale V are of the same order. This is the dynamical regime of our slowly rotating simulation.

In this dynamical regime, the magnitude of horizontal temperature variations can be estimated through scale analysis of the horizontal momentum equations (Charney 1963). In the free atmosphere, where frictional forces can be neglected, inertial accelerations scale advectively, like $\sim U^2/L$, and are balanced by accelerations owing to pressure gradients, which scale like $\delta p/(\rho L)$, where δp is the scale of horizontal pressure variations and ρ is density. The density and vertical pressure variations are related by the hydrostatic relation, $p/H \sim \rho g$, where $H = RT/g$ is the pressure scale height (specific gas constant R and temperature T). If one combines the scalings from the horizontal momentum and hydrostatic equations, horizontal variations in pressure, density, and (potential) temperature (using the ideal gas law) scale like

$$\frac{\delta p}{p} \sim \frac{\delta \rho}{\rho} \sim \frac{\delta \theta}{\theta} \sim \frac{U^2}{gH} \equiv \mathrm{Fr}, \tag{B.5}$$

where $\mathrm{Fr} = U^2/(gH)$ is the Froude number. For a terrestrial planet with $H \approx 7\,\mathrm{km}$ and $g = 9.8\,\mathrm{m\,s^{-2}}$, the Froude number is $\mathrm{Fr} \lesssim 10^{-2}$ for velocities $U \lesssim 25\,\mathrm{m\,s^{-1}}$. So free-atmospheric horizontal temperature and pressure variations are expected to be small insofar as velocities are not too strong (e.g., if their magnitude is limited by shear instabilities). This is the case in the tropics of Earth's atmosphere, and these expectations are also borne out in the slowly rotating simulation.

B.4.1 Surface temperature and outgoing longwave radiation

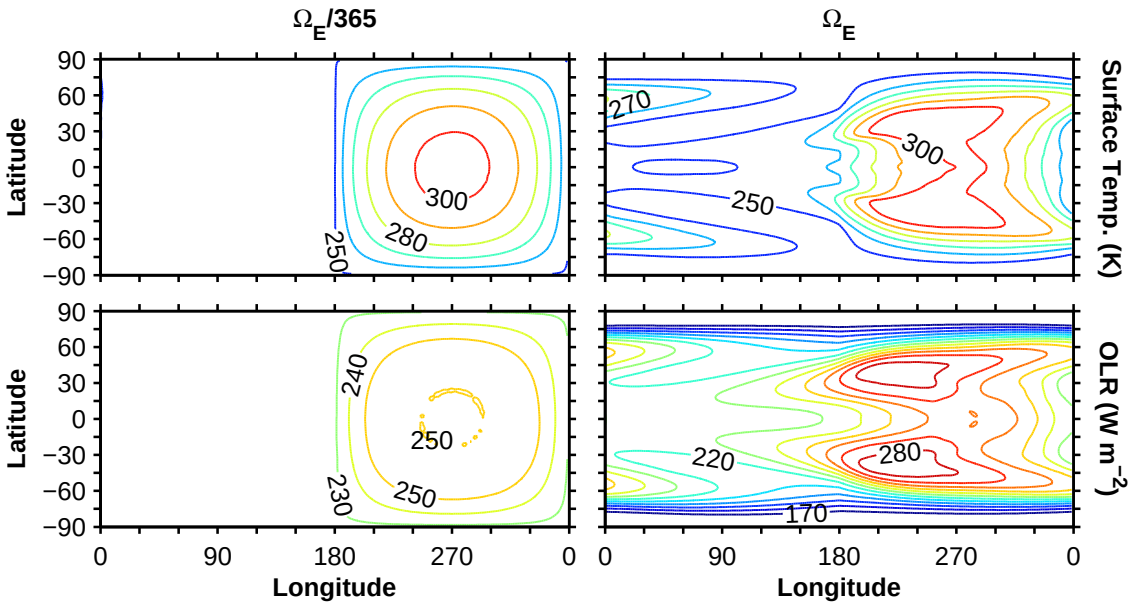

Figure B.1. Top row: surface temperature (K) in simulations with $\Omega_E/365$ (left) and Ω_E (right). The contour interval is 10 K. Bottom row: outgoing longwave radiation, OLR, ($\mathrm{W\,m^{-2}}$) in simulations with $\Omega_E/365$ (left) and Ω_E (right). The contour interval is $10\,\mathrm{W\,m^{-2}}$.

In the slowly rotating simulation, the surface temperature mimics the insolation distribution on the day side of the planet, decreasing monotonically and isotropically away from the subsolar point; the night side of the planet has a nearly uniform surface temperature (Fig. B.1). Though the surface temperature resembles the insolation distribution, the influence of atmospheric dynamics is clearly evident in that the night side of the planet is considerably warmer than the radiative-convective equilibrium temperature of 0 K.

For exoplanets, the outgoing longwave radiation (OLR) is more easily measurable than the surface temperature. In the slowly rotating simulation, the relative magnitude of the OLR contrast between the day side and night side of the planet is muted compared with that of the surface temperature contrast (Fig. B.1) because free-tropospheric temperature gradients are weaker than surface temperature gradients (as will be discussed further in section B.4d).

B.4.2 Hydrological cycle

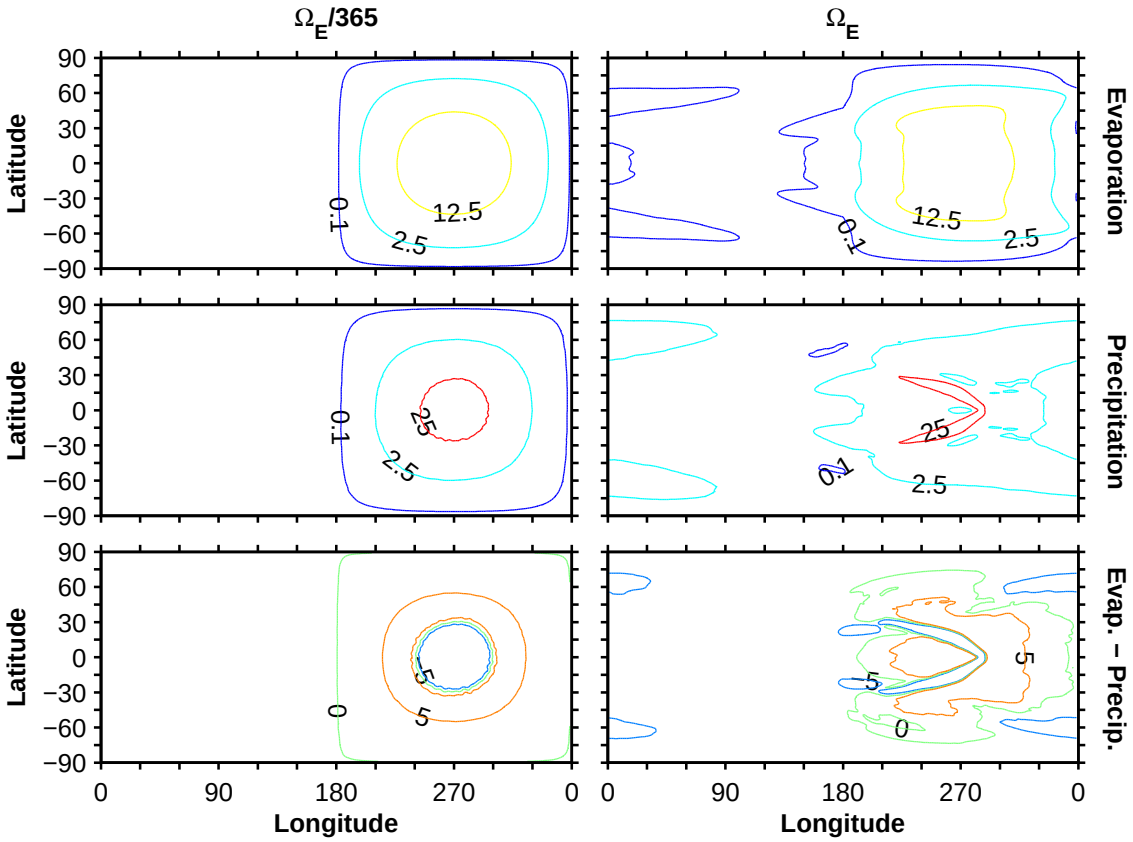

Figure B.2. Evaporation (top row, mm day^{-1}), precipitation (middle row, mm day^{-1}), and evaporation minus precipitation (bottom row, mm day^{-1})) in simulations with $\Omega_E/365$ (left) and Ω_E (right). Contours are shown at $0.1, 2.5$, and $12.5\,\mathrm{mm\,day^{-1}}$ for evaporation, $0.1, 2.5$, and $25.0\,\mathrm{mm\,day^{-1}}$ for precipitation, and $-5.0, 0$, and $5.0\,\mathrm{mm\,day^{-1}}$ for evaporation minus precipitation.

Surface evaporation rates likewise mimic the insolation distribution (Fig. B.2), as would be expected from a surface energy budget in which the dominant balance

is between heating by shortwave radiation and cooling by evaporation. This is the dominant balance over oceans on Earth (e.g., Trenberth et al. 2009), and in general on sufficiently warm Earth-like aquaplanets (Pierrehumbert 2002; O'Gorman and Schneider 2008b). The dominance of evaporation in the surface energy budget in sufficiently warm climates can be understood by considering how the Bowen ratio, the ratio of sensible to latent surface fluxes, depends on temperature. For surface fluxes given by bulk aerodynamic formulas, the Bowen ratio B depends on the surface temperature T_s, the near-surface air temperature T_a, and the near-surface relative humidity $\mathcal{H}$,

$$B \sim \frac{c_p(T_s - T_a)}{L\big(q^*(T_s) - \mathcal{H}q^*(T_a)\big)}, \tag{B.6}$$

where q^* is the saturation specific humidity, c_p is the specific heat of air at constant pressure, and L is the latent heat of vaporization. Figure B.3 shows the Bowen ratio as a function of surface temperature, assuming a fixed surface–air temperature difference and fixed relative humidity. We have fixed these to values that are representative of the GCM simulations for simplicity, but the surface–air temperature difference and relative humidity are not fixed in the GCM. For surface temperatures greater than $\sim$290 K, latent heat fluxes are a factor of $\gtrsim 4$ larger than sensible heat fluxes, as at Earth's surface (Trenberth et al. 2009). Similar arguments apply for net longwave radiative fluxes at the surface, which become small as the longwave optical thickness of the atmosphere and with it surface temperatures increase; see Pierrehumbert (2010) for a more complete discussion of the surface energy budget.

The precipitation rates likewise mimic the insolation distribution (Fig. B.2). There is a convergence zone with large precipitation rates ($\geq 40\,\mathrm{mm\,day^{-1}}$) around the subsolar point. Precipitation rates exceed evaporation rates within $\sim 15^\circ$ of the subsolar point. Outside that region on the day side, evaporation rates exceed precipitation rates (Fig. B.2), which would lead to the generation of deserts there if the surface water supply were limited. The atmospheric circulation that gives rise to the moisture transport toward the subsolar point is discussed next.

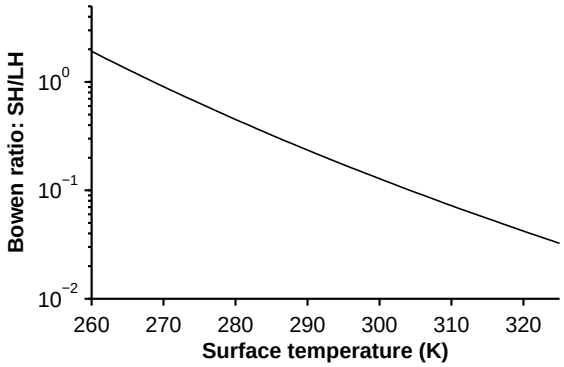

Figure B.3. Bowen ratio vs. surface temperature assuming a 3-K surface–air temperature difference, 70% relative humidity, and surface and surface air pressure of 10^5 Pa, using the same simplified saturation vapor pressure formula as in the GCM.

B.4.3 General circulation of the atmosphere

The winds are approximately isotropic and divergent at leading order. They form a thermally direct overturning circulation, with lower-level convergence near the subsolar point, upper-level divergence above it, and weaker flow in between (Fig. B.4). As in the simulations of Joshi et al. (1997), the meridional surface flow crosses the poles. Moist convection in the vicinity of the subsolar point results in strong mean ascent in the mid-troposphere there; elsewhere there is weak subsidence associated with radiative cooling (Fig. B.5). Consistent with the predominance of divergent and approximately isotropic flow, the Rossby number is large even in the extratropics ($\mathrm{Ro} \gtrsim 10$).

The zonal-mean zonal wind and streamfunction are shown in Fig. B.6. The zonal-mean zonal wind is a weak residual of the opposing contributions from different longitudes (Fig. B.4). In the upper troposphere near the equator, there are weak westerly (superrotating) zonal winds, as well as the eddy angular momentum flux convergence that, according to Hide's theorem, is necessary to sustain them (e.g., Hide 1969; Schneider 1977; Held and Hou 1980; Schneider 2006).

The Eulerian mean mass streamfunction consists of a Hadley cell in each hemisphere, which is a factor $\sim$3 stronger than Earth's and extends essentially to the pole. These Hadley cells are thermodynamically direct circulations: the poleward flow to

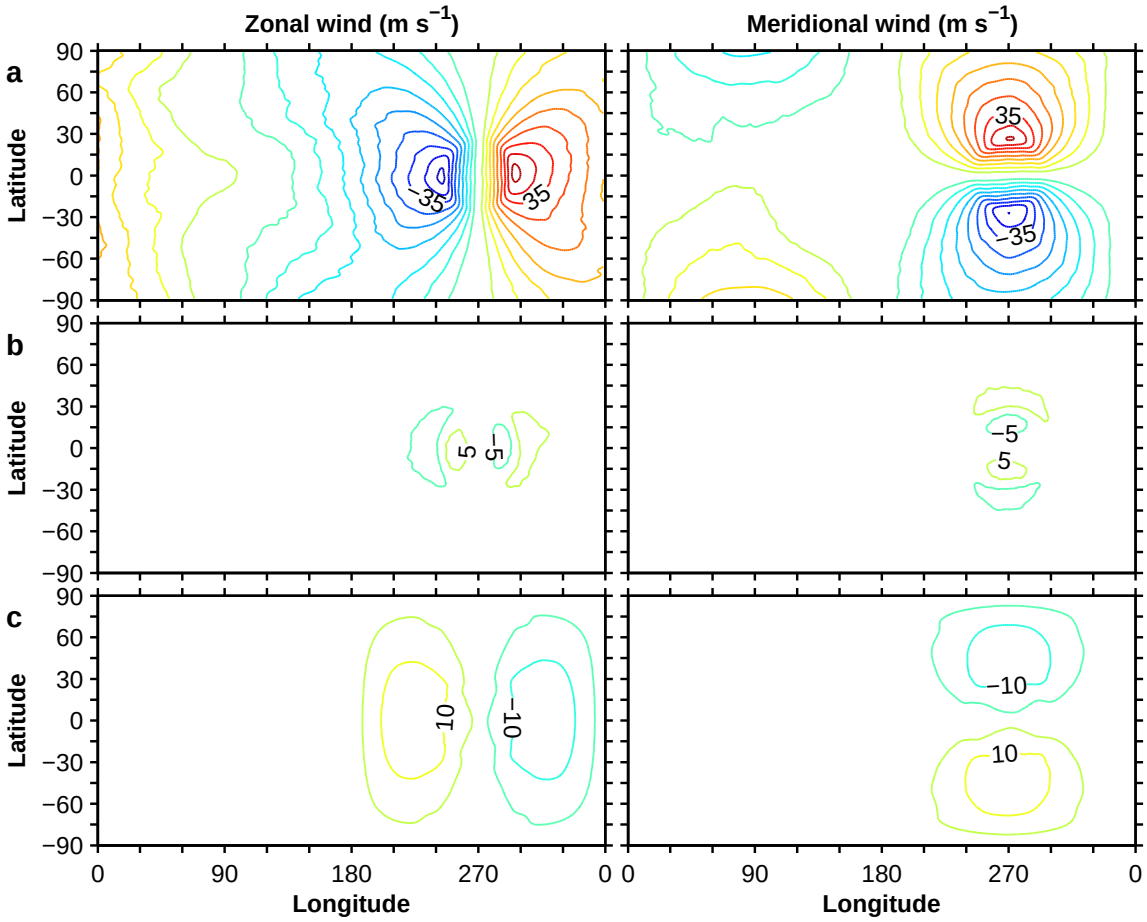

Figure B.4. Zonal wind (left) and meridional wind (right) in $\Omega_E/365$ simulation on the $\sigma = 0.28$ (a), 0.54 (b), and 1.0 (c) surfaces. The contour interval is $5\,\mathrm{m\,s^{-1}}$, and the zero contour is not shown.

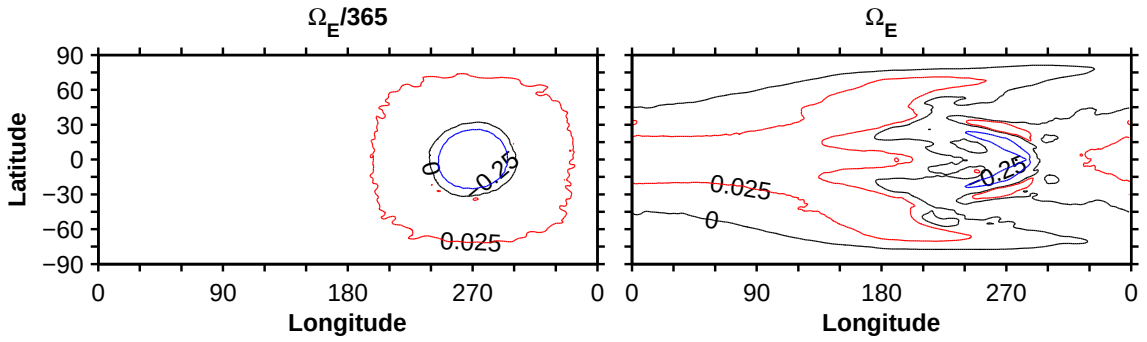

Figure B.5. Pressure velocity ($\omega = Dp/Dt$) on the $\sigma = 0.54$ surface in simulations with $\Omega_E/365$ (left) and Ω_E (right). Contours are shown at -0.25 (blue), 0 (black), and 0.025 (red) $\mathrm{Pa\,s^{-1}}$.

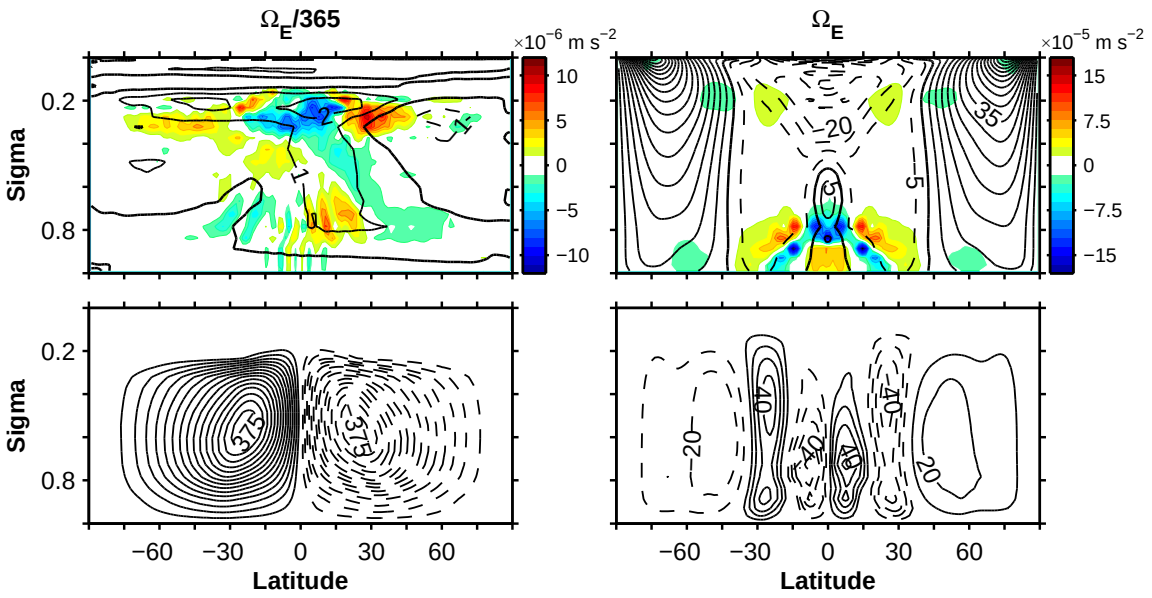

Figure B.6. Circulation in simulations with $\Omega_E/365$ (left panels) and Ω_E (right panels). Top row: zonal-mean zonal wind (lines, contour interval $1\,\mathrm{m\,s^{-1}}$ for Ω_E and $5\,\mathrm{m\,s^{-1}}$ for $\Omega_E/365$) and divergence of the horizontal component of eddy (transient and stationary) angular momentum fluxes (colors, contour interval $1.0 \times 10^{-6}\,\mathrm{m\,s^{-2}}$ for $\Omega_E/365$ and $1.5 \times 10^{-5}\,\mathrm{m\,s^{-2}}$ for Ω_E). Bottom row: Eulerian mean mass flux streamfunction (contour interval $25 \times 10^9\,\mathrm{kg\,s^{-1}}$ for $\Omega_E/365$ and $10 \times 10^9\,\mathrm{kg\,s^{-1}}$ for Ω_E).

higher latitudes has larger moist static energy ($h = c_pT + gz + Lq$) than the near-surface return flow. The classic theory of Hadley cells with nearly inviscid, angular momentum-conserving upper branches predicts that the Hadley cell extent increases as the rotation rate decreases (Schneider 1977; Held and Hou 1980). However, the results of this theory do not strictly apply here because several assumptions on which it is based are violated. For example, the surface wind is not weak relative to the upper-tropospheric winds (Fig. B.4), and the zonal wind is not in (geostrophic or gradient-wind) balance with meridional geopotential gradients (i.e., the meridional wind is not negligible in the meridional momentum equation). Nonetheless, it is to be expected that Hadley cells in slowly rotating atmospheres span hemispheres (Williams 1988).

The instantaneous, upper-tropospheric zonal wind is shown in Fig. B.7, and a corresponding animation is available at `http://www.gps.caltech.edu/~tapio/`

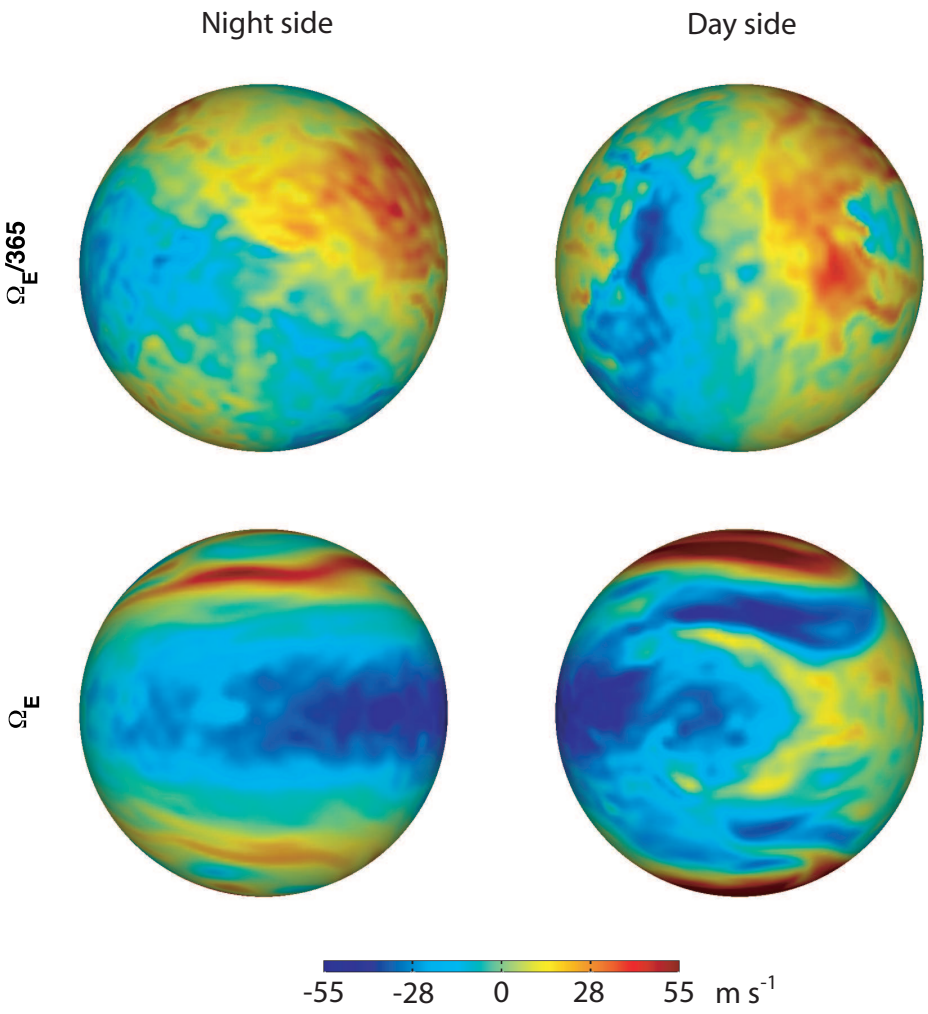

Figure B.7. Instantaneous zonal wind on $\sigma = 0.28$ surface in the statistically steady state (on day 3900) of the two simulations. Animations are available at `http://www.gps.caltech.edu/~tapio/animations/tidally_locked_slow.mov` and `http://www.gps.caltech.edu/~tapio/animations/tidally_locked_fast.mov` .

`animations/tidally_locked_slow.mov`. Although the flow statistics in the simulations are hemispherically symmetric (because the forcing and boundary conditions are), the instantaneous wind exhibits north-south asymmetries on large scales and ubiquitous variability on smaller scales. The large-scale variability has long timescales (∼80 days), and the zonal-mean zonal wind is sensitive to the length of the time averaging: for timescales as long as the 500 days over which we averaged, the averages still exhibit hemispheric asymmetries (Fig. B.6).

The vertically integrated eddy kinetic energy is 8.4×10^5 J m^{-2} in the global

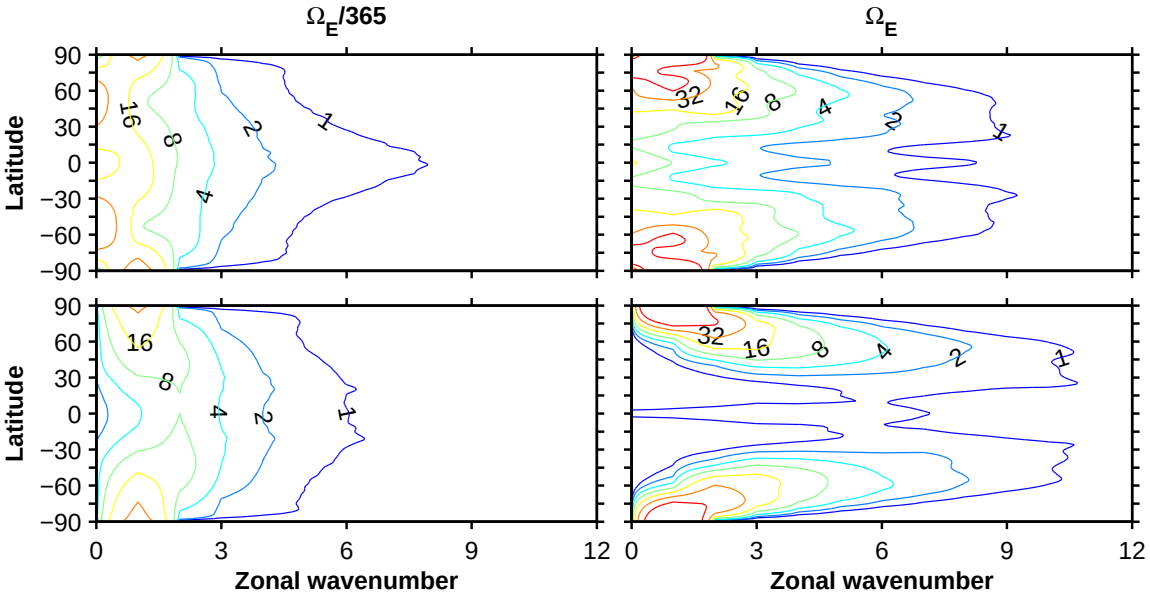

Figure B.8. Spectrum of the mass-weighted, vertically averaged transient velocity variance for zonal (top row) and meridional (bottom row) wind components in the simulations with $\Omega_E/365$ (left) and Ω_E (right). Contours are shown at $2^0, 2^1, ..., 2^6$ m^2 s^{-2}.

mean. The instantaneous velocity fields exhibit substantial variability on relatively small scales (e.g., Fig. B.7), and the kinetic energy spectrum decays only weakly from spherical wavenumber ∼20 toward the roll-off near the grid scale owing to the subgrid-scale filter. However, the peak in velocity variance is at the largest scales (Fig. B.8)—as suggested by the hemispherically asymmetric large-scale variability seen in Fig. B.7 and in the animation.

B.4.4 Atmospheric stratification and energy transports

Consistent with the scaling arguments presented above, horizontal variations in temperature are small in the free troposphere (above the ∼750 hPa level, Fig. B.9). This is reminiscent of Earth's tropics, where temperature variations are small because Coriolis accelerations are weak compared with inertial accelerations (e.g., Charney 1963; Sobel et al. 2001). Here, Coriolis accelerations are weak at all latitudes, and free-tropospheric horizontal temperature variations are small everywhere.

The thermal stratification on the day side in the simulation is moist adiabatic

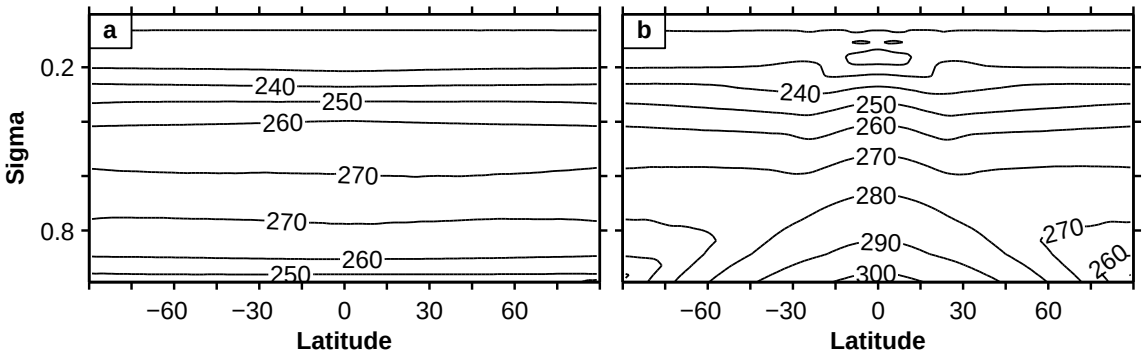

Figure B.9. Temperature section of antisolar longitudes (a) and subsolar longitudes (b) of $\Omega_E/365$ simulation. Averages are taken over 10° of longitude. The contour interval is 10 K.

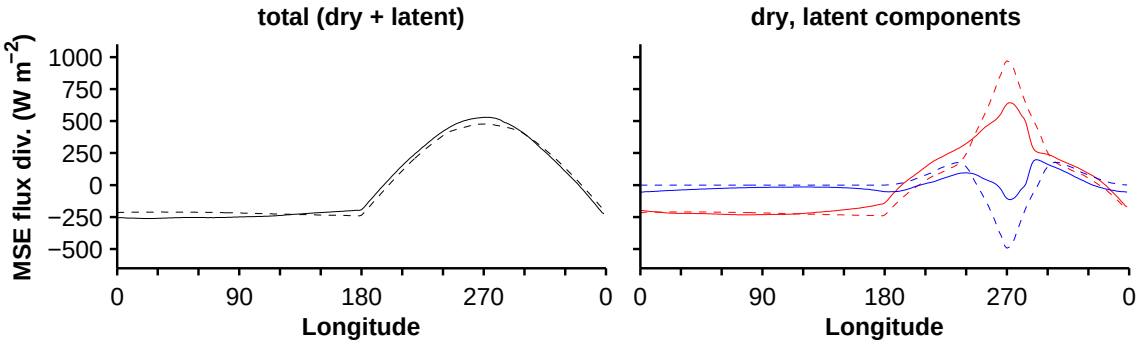

Figure B.10. Left: Vertical and meridional integral of the divergence of the zonal moist static energy flux, uh. Right: Dry static energy (red) and latent energy (blue) components of moist static energy flux divergence. Dashed lines for $\Omega_E/365$ simulation and solid lines for Ω_E simulation.

in the free troposphere within ∼30° of the subsolar point. Farther away from the intense moist convection around the subsolar point, including on the night side of the planet, there are low-level temperature inversions (Fig. B.9b), as in the simulations in Joshi et al. (1997). These regions have small optical thickness because of the low water vapor concentrations and therefore have strong radiative cooling to space from near the surface. The inversions arise because horizontal temperature gradients are constrained to be weak in the free troposphere, whereas near-surface air cools strongly radiatively, so that cool surface air underlies warm free-troposphere air.

The vertical and meridional integral of the zonal moist static energy flux divergence as a function of longitude is shown in Fig. B.10 (dashed curves). Energy

diverges on the day side and converges on the night side of the planet, reducing temperature contrasts. Near the subsolar point, there is substantial cancellation between the latent energy and dry static energy components of the moist static energy flux divergence as there is, for example, in Earth's Hadley circulation. As can be inferred from the minimal water vapor flux divergence on the night side (Fig. B.2), the moist static energy flux divergence there is dominated by the dry static energy ($c_pT + gz$) component ($\gtrsim 99\%$ of the total).

B.5 Rapidly rotating simulation

In rapidly rotating atmospheres, the Rossby number in the extratropics is small, and geostrophic balance is the dominant balance in the horizontal momentum equations. In the zonal mean, zonal pressure gradients vanish, but meridional pressure gradients do not, so if the dominant momentum balance is geostrophic, winds are anisotropic with $\bar{U} > \bar{V}$, where $\overline{(\cdot)}$ denotes a zonal mean. Variations in the planetary vorticity with latitude, β, are central to vorticity mixing arguments (e.g., Rhines 1994; Held 2000), which can account for the generation of atmospheric zonal jets: When a Rossby wave packet stirs the atmosphere in a region bounded by a polar cap, high-vorticity fluid moves equatorward and low-vorticity fluid moves poleward. This reduces the vorticity in the polar cap. By Stokes' Theorem, the reduced vorticity in the polar cap means that the zonal wind at the latitude of the bounding cap decreases; if angular momentum is conserved, the zonal wind outside the polar cap increases. Irreversible vorticity mixing (wave-breaking or dissipation) is necessary to maintain the angular momentum fluxes in the time mean. Thus, the larger planetary vorticity gradients of the rapidly rotating planet allow zonal jets to form provided there is a source of wave activity that leads to vorticity stirring.

We return to the analysis of Charney (1963) to estimate temperature variations in the free atmosphere. For rapidly rotating planets, geostrophic balance holds in the horizontal momentum equations: $\delta p/(\rho L) \sim fU$. Combining the scaling from the momentum equation with the hydrostatic relation, the pressure, density, and

(potential) temperature variations scale like the ratio of the Froude number to the Rossby number,

$$\frac{\delta p}{p} \sim \frac{\delta \rho}{\rho} \sim \frac{\delta \theta}{\theta} \sim \frac{fUL}{gH} = \frac{\mathrm{Fr}}{\mathrm{Ro}}. \tag{B.7}$$

Where the Rossby number is small (in the extratropics), the temperature variations will be a factor of order inverse Rossby number ($\mathrm{Ro}^{-1} \sim 10$) larger than in the slowly rotating simulation for similar values of U, g, and H. Thus, we expect larger horizontal temperature and pressure variations away from the equator in the rapidly rotating simulation.

B.5.1 Surface temperature and outgoing longwave radiation

In the rapidly rotating simulation, the surface temperature on the day side of the planet is maximal off of the equator and does not bear a close resemblance to the insolation distribution; the night side of the planet has relatively warm regions in western high latitudes (Fig. B.1). Compared to the slowly rotating simulation, the surface temperature is more substantially modified by the atmospheric circulation; however, the temperature contrasts between the day and night side are similar.

The outgoing longwave radiation of the rapidly rotating simulation has substantial variations (Fig. B.1). Some of the structures in the surface temperature are echoed in the OLR distribution. Compared to the slowly rotating simulation, OLR variations have smaller spatial scales and occupy a wider range of values.

B.5.2 Hydrological cycle

Surface evaporation rates mimic the insolation distribution (Fig. B.2). This is one of the most similar fields between the slowly and rapidly rotating simulations, as expected from the gross similarity in surface temperature and the smallness of the Bowen ratio at these temperatures (Fig. B.3). This might not be the case if the model included the radiative effects of clouds since the amount of shortwave radiation reaching the surface would be shaped by variations in cloud albedo, which, in turn, depend on the atmospheric circulation.

Precipitation rates are large in a crescent-shaped region on the day side of the planet; the night side of the planet generally has small but nonzero precipitation rates (Fig. B.2). The evaporation minus precipitation field has substantial structure: there are large amplitude changes from the convergence zones ($P > E$) to nearby areas of significant net drying ($E > P$). Comparing the slowly and rapidly rotating simulations shows that precipitation and $E - P$ on the night side of the planet are sensitive to the atmospheric circulation.

An interesting aspect of the climate is that the precipitation maximum (near $\sim$15° latitude) is not co-located with the off-equatorial surface temperature maximum (near $\sim$40° latitude). The simulation provides an example of precipitation and deep convection that are not locally thermodynamically controlled: the precipitation is not maximum where the surface temperature is maximum; the column static stability (e.g., Fig. B.13), and therefore the convective available potential energy, are not markedly different between the maxima in precipitation and temperature. However, if the surface climate is examined latitude-by-latitude instead of examining the global maxima, the region of large precipitation is close to the maximum surface temperature (as well as surface temperature curvature) at a given latitude. The structure of the surface winds, discussed next, and the associated moisture convergence are key for determining where precipitation is large. Sobel (2007) provides a review of these two classes of theories for tropical precipitation (thermodynamic control vs. momentum control) and the somewhat inconclusive evidence of which class of theory better accounts for Earth observations.

The global precipitation is $\sim$10% larger in the rapidly rotating simulation than in the slowly rotating simulation. This suggests that radiative-convective equilibrium cannot completely describe the strength of the hydrological cycle.

B.5.3 General circulation of the atmosphere

In the rapidly rotating simulation, the atmospheric circulation has several prominent features: there are westerly jets in high ($\sim$65°) latitudes, the mid-tropospheric zonal

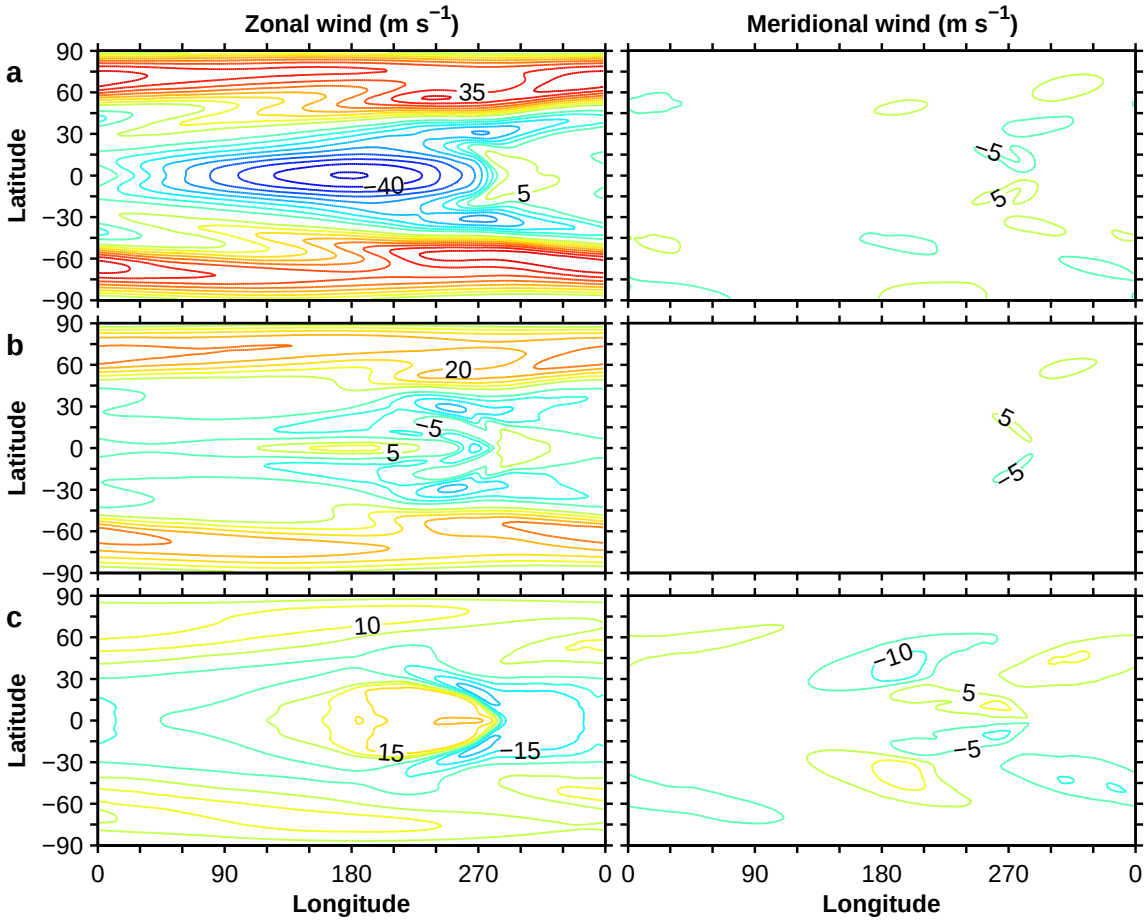

Figure B.11. Zonal wind (left) and meridional wind (right) of Ω_E simulation on the $\sigma = 0.28$ (a), 0.54 (b), and 1.0 (c) surfaces. The contour interval is $5\,\mathrm{m\,s^{-1}}$, and the zero contour is not shown.

wind exhibits equatorial superrotation, and the surface winds converge in a crescent-shaped region near the subsolar point (Fig. B.11). The equatorial superrotation and westerly jets are evident in the zonal-mean zonal wind (Fig. B.6).

The existence of the high-latitude jets can be understood from the temperature field and eddy angular momentum flux convergence (Figs. B.13 and B.6). There are large meridional temperature gradients, which give rise to zonal wind shear by thermal wind balance and provide available potential energy for baroclinic eddies that transport angular momentum into the jets. In the vertical average, the eddy angular momentum transport into an atmospheric column is balanced by surface stress (provided the Rossby number is small), so surface westerlies appear underneath

high-latitude regions of angular momentum flux convergence.

The equatorial superrotation is a consequence of angular momentum flux convergence (Fig. B.6). Saravanan (1993) and Suarez and Duffy (1992) describe the emergence of superrotation generated by large-scale, zonally asymmetric heating anomalies in the tropics. As in their idealized models, the zonal asymmetry in the low-latitude heating (in our simulation, provided by insolation) generates a stationary Rossby wave. Consistent with a stationary wave source, in the rapidly rotating simulation, the horizontal eddy angular momentum flux convergence in low latitudes is dominated by the stationary eddy component. This aspect of the simulation is sensitive to horizontal resolution and the subgrid-scale filter. With higher resolution or weaker filtering, the superrotation generally extends higher into the troposphere and has a larger maximum value.

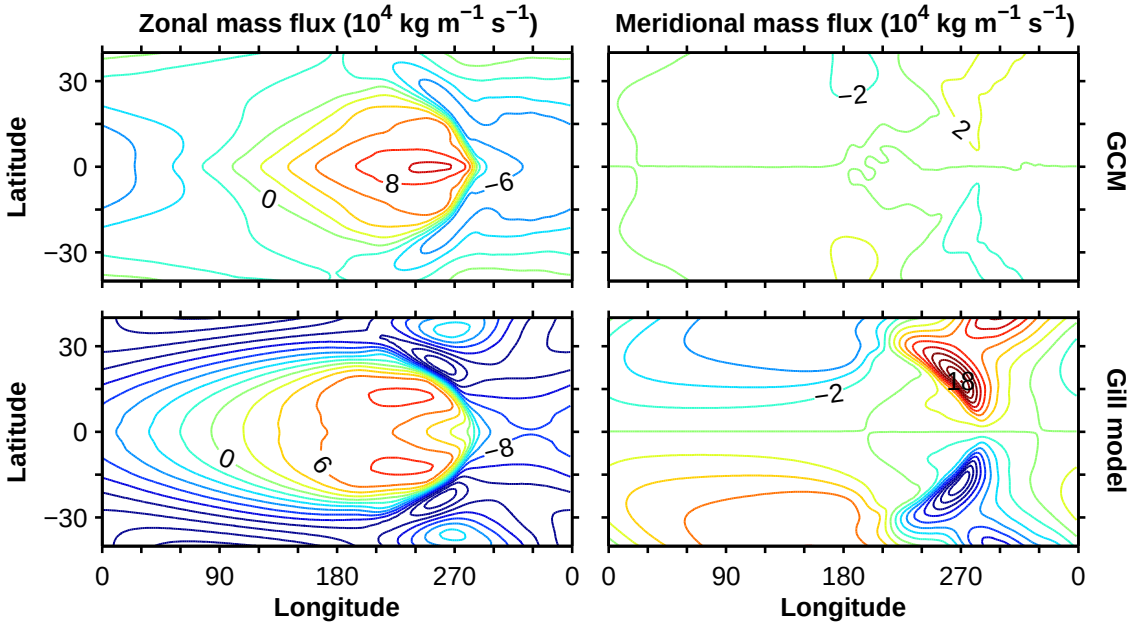

Figure B.12. Zonal (left column) and meridional (right column) near-surface mass fluxes for the GCM (top row, averaged between the surface and $\sigma = 0.73$ model level) and the Gill model forced by the GCM's precipitation (bottom row, see Appendix for Gill model equations and parameters). The contour interval is $2 \times 10^4\,\mathrm{kg\,m^{-1}\,s^{-1}}$.

There is a crescent-shaped region where the surface zonal wind is converging. This is where the precipitation (Fig. B.2) and upward vertical velocity (Fig. B.5)

are largest. The horizontal scale of the convergence zone is similar to the equatorial Rossby radius, $(c/\beta)^{1/2}$, where β is the gradient of planetary vorticity and c is the gravity wave speed. If moisture effects are neglected, the gravity wave speed is estimated using a characteristic tropospheric value for the Brunt-Väisälä frequency on the day side of the planet, the equatorial Rossby radius corresponds to $\sim 10^\circ$ latitude, which is of the same order as the scale of the convergence zone. The surface zonal wind can be qualitatively understood as the equatorially-trapped wave response to stationary heating: equatorial Kelvin waves propagate to the east of the heating and generate easterlies; equatorial Rossby waves propagate to the west of the heating and generate westerlies (Gill 1980).

The shape of the zero zonal wind line and its horizontal scale are similar to those of the Gill (1980) model, which describes the response of damped, linear shallow-water waves to a prescribed heat/mass source. For the prescribed heat source in the original Gill model, the crescent-shape zero zonal wind line extends over ~ 2 Rossby radii and, as in the GCM simulation, is displaced to the east of the heating maximum on the equator.

A complicating factor in the analogy between the GCM's low-latitude surface winds and those of the Gill model is that the heating is prescribed in the Gill model, while it interacts with the flow in the GCM. As previously mentioned, the precipitation is strongly shaped by the winds. To see if the analogy between the winds in the GCM and in the Gill model breaks down because of the more complex structure of the latent heating, we force a variant of the Gill model with the GCM's precipitation field following the formulation of Neelin (1988) (see Appendix for details). The results of this calculation are compared with the GCM output in Fig. B.12. The direction, large-scale structure, and, in the case of the zonal component, magnitude of the mass fluxes are similar between the GCM and precipitation-forced Gill model, though it is clear that there are quantitative differences. Better quantitative agreement particularly in the meridional component could be achieved by using anisotropic damping (different damping coefficients in the zonal and meridional direction) in the Gill model, as is common in studies of Earth's atmosphere (e.g., Stevens et al. 2002).

In contrast to the zonal wind, which has larger magnitude, the meridional wind is diverging at the surface and converging aloft near the subsolar point (right panel of Fig. B.11a,c). As discussed by Gill (1980), the reasons for this lie in the vorticity balance: for a Sverdrup vorticity balance, the vortex stretching caused by the overall convergence near the surface near the equator must be balanced by poleward motion, toward higher planetary vorticity, and vice versa at higher levels; hence, the meridional wind is poleward near the surface and equatorward aloft.

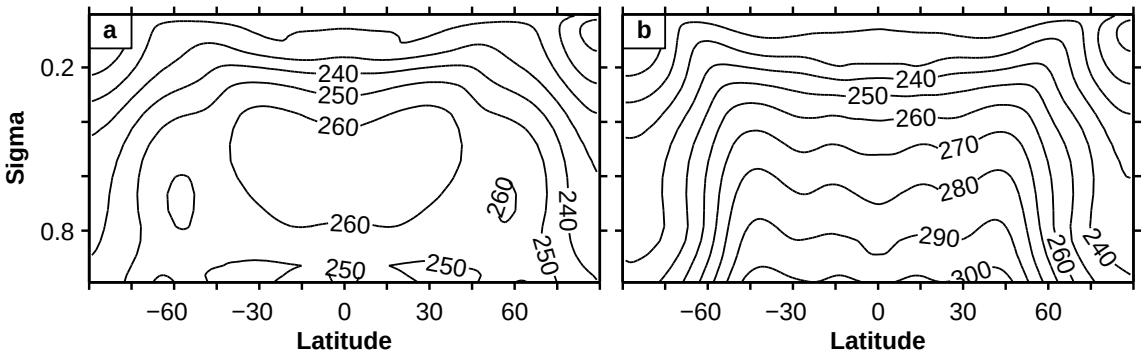

Figure B.13. Temperature section of antisolar longitudes (a) and subsolar longitudes (b) in Ω_E simulation. Averages are taken over 10° of longitude. The contour interval is 10 K.

The Eulerian mean mass streamfunction (Fig. B.6) has the opposite sense as Earth's Hadley cells: in the zonal mean, there is descent at the equator, poleward flow near the surface, ascent near 15°, and equatorward flow near the surface and in the mid-troposphere. If the dominant balance in the zonal momentum equation is between Coriolis acceleration and eddy angular momentum flux divergence, $-f\bar{v} \sim -\partial_y \overline{u'v'}$ (i.e., small local Rossby number as defined in Walker and Schneider (2006)), then the angular momentum flux convergence that establishes the superrotating zonal wind also leads to equatorward mean meridional wind in the free troposphere, as in Earth's Ferrel cells (e.g., Held 2000). This can lead to a dynamical feedback that enhances superrotation (Schneider and Liu 2009): as superrotation emerges, the mean meridional circulation can change direction with a concomitant change in the direction of mean-flow angular momentum fluxes (changing from exporting angular momentum from the deep tropics to importing it), which enhances the superrotation.

The instantaneous, upper tropospheric zonal wind in the rapidly rotating simulation is shown in Fig. B.7, and a corresponding animation is available at `http://www.gps.caltech.edu/~tapio/animations/tidally_locked_fast.mov`. The large-scale features of the general circulation such as the high-latitude jets and divergent zonal wind in the tropical upper troposphere are clear in the instantaneous winds. The eddies in the animation generally have larger spatial scales and longer timescales than in the corresponding slowly rotating animation.

The vertically and globally integrated eddy kinetic energy is 1.0×10^6 J m^{-2}. This is about 20% larger than in the slowly rotating case. The eddy kinetic energy spectrum has a typical n^{-3} shape in spherical wavenumber n, up to the smallest resolved wavenumber. But the integrated eddy kinetic energy hides an important difference in synoptic variability between the rapidly and slowly rotating simulations: in the extratropics, for zonal wavenumbers between ∼3–6, the rapidly rotating simulation has a factor of 2–3 times more velocity variance (Fig. B.8) than the slowly rotating simulation.

B.5.4 Atmospheric stratification and energy transports

The tropospheric temperature distribution on the day side of the planet (Fig. B.13) resembles the surface temperature distribution: the temperature field has a local maximum near ∼40° latitude and is relatively uniform up to high latitudes (up to ∼50°). In the free troposphere on the day side, the lapse rates are close to the moist adiabatic lapse rate, computed using the local temperature and pressure, over a region roughly within the 300 K contour of the surface temperature. Note that 300 K does not have a particular physical significance, e.g., as a deep convection threshold—we are simply using it to describe a feature of the simulation. There is a local minimum of temperature on the equator which may be related to the downward vertical velocity there (Fig. B.5). In low latitudes, there is a near-surface inversion on the night side of the rapidly rotating simulation that, as in the slowly rotating simulation, is the result of weak temperature gradients in the free troposphere and the substantial radiative

cooling owing to the small optical thickness of the atmosphere.

As in the slowly rotating simulation, the moist static energy flux diverges on the day side and converges on night side of the planet (solid curves in Fig. B.10); there is substantial cancellation between the dry static energy flux and the latent energy flux divergence near the subsolar point. Though the hydrological cycle is more active on the night side of the rapidly rotating simulation than in the slowly rotating simulation, the dry static energy component still dominates ($\gtrsim$80% of total) the moist static energy advection on the night side of the planet.

The two simulations are more similar in this respect than might have been anticipated given the differences in their flow characteristics, although there are regional differences that are obscured by averaging over latitude. The broad similarities can be understood by considering the moist static energy budget. In the time mean, denoted by $[\cdot]$, neglecting kinetic energy fluxes and diffusive processes within the atmosphere, the mass-weighted vertical integral $\langle\cdot\rangle$ of the moist static energy flux divergence is balanced by surface energy fluxes F_s and radiative tendencies Q_rad,

$$\nabla\cdot\langle[\mathbf{u}h]\rangle = [F_\mathrm{s}] + [Q_\mathrm{rad}]. \tag{B.8}$$

As a result of the gross similarity of the two simulations in evaporation and low-latitude stratification (in part due to the smaller dynamical role that rotation plays near the equator), and hence the gross similarity in radiative cooling, the divergence of the moist static energy flux is also similar, at least in low latitudes and in the meridional mean. Locally in the extratropics, however, considering the sources and sinks of moist static energy does not provide a useful constraint because the stratification is dynamically determined and not moist adiabatic (e.g., Schneider and O'Gorman 2008), and there can be geostrophically balanced temperature gradients in rapidly rotating atmospheres. As a consequence, the radiative cooling, through dynamical influences on temperature, is determined by the flow, so the moist static energy flux divergence will generally depend on the rotation rate. Indeed, the warm regions on the night side of the rapidly rotating simulation have larger moist static energy flux

divergence than the corresponding regions in the slowly rotating simulation.

B.6 Systematic variation of rotation rate

B.6.1 Equatorial superrotation

In the rapidly rotating simulation, the mid-tropospheric zonal-mean zonal winds near the equator are weakly superrotating. In the slowly rotating simulation, they are also superrotating, but even more weakly so. Given that equatorial superrotation generally occurs even with zonally symmetric heating when planetary rotation rates are sufficiently low ($\Omega \lesssim \Omega_E/4$ for the otherwise Earth-like planets in Walker and Schneider (2006)), one may suspect that the zonal-mean zonal winds are more strongly superrotating at intermediate planetary rotation rates.

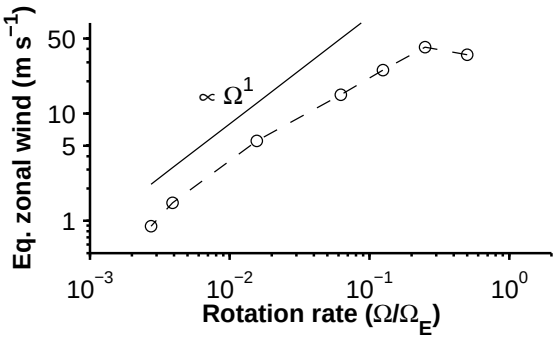

Figure B.14. Barotropic equatorial zonal-mean zonal wind vs. rotation rate averaged within 3° of latitude of the equator. Solid line shows power law with exponent +1. For $\Omega = \Omega_E$, the zonal wind is $-7.1\,\mathrm{m\,s^{-1}}$ and hence is not shown.

Figure B.14 shows the barotropic (mass-weighted vertical average) equatorial zonal-mean zonal wind as the rotation rate is varied. Simulated rotation rate values are $\Omega = (1,\, 1/2,\, 1/4,\, 1/8,\, 1/16,\, 1/64,\, 1/256,\, 1/365)\,\Omega_E$. The strength of the equatorial superrotation indeed is maximal for intermediate rotation rates ($\Omega \approx \Omega_E/4$).

The increase with rotation rate in the strength of equatorial superrotation for low values of Ω can be qualitatively understood from the angular momentum balance and the way eddies enter it. The angular momentum balance near the equator is generally dominated by the angular momentum flux convergence by stationary eddies and

by the zonal-mean flow; angular momentum fluxes associated with transient eddies are weaker. The stationary eddy angular momentum flux convergence increases with rotation rate, with a somewhat weaker than linear dependence on rotation rate; it has a maximum at intermediate rotation rates ($\Omega \approx \Omega_E/4$). This is a consequence, in part, of the increase in vortex stretching and vorticity advection by the divergent flow with increasing rotation rate: The stationary Rossby waves giving rise to the angular momentum flux are generated by vortex stretching in divergent flow or by vorticity advection by the divergent flow, which is generated at upper levels by the heating around the subsolar point (Sardeshmukh and Hoskins 1988). The eddy angular momentum flux convergence is equal to the rate at which Rossby wave activity is generated (e.g., Schneider and Liu 2009).

To understand the full behavior of the superrotation over the range of rotation rates, one must also understand the angular momentum flux divergence by the zonal-mean flow; however, these changes are not simple as the strength of the Hadley circulation depends on rotation rate and the character of the angular momentum balance changes with rotation rate—the local Rossby number decreases as rotation rate increases. Such changes in the Hadley circulation likely play a role in the decrease in the strength of equatorial superrotation as the rotation rate increases beyond $\sim\Omega_E/4$. Additionally, changes in the vertical shear contribute to changes in the strength of equatorial superrotation; in the slowly rotating limit, the shear is no longer related to the temperature field by gradient wind balance.

We have also performed simulations with zonally symmetric insolation that are otherwise identical to those in Fig. B.14. While there is equatorial superrotation, it is substantially weaker: $\sim 5\,\mathrm{m\,s^{-1}}$ compared to $\sim 25\,\mathrm{m\,s^{-1}}$ at intermediate rotation rates. This suggests qualitative differences in the atmospheric circulation when there is zonally symmetric forcing compared to zonally asymmetric forcing and provides an additional demonstration of the central role stationary eddies play in the superrotation of the tidally locked simulations.

B.6.2 Day-side to night-side temperature contrast

Figure B.15 shows the day-side to night-side surface temperature contrast in the simulations with different rotation rates. As suggested by the slowly and rapidly rotating simulations examined in detail above, the surface temperature contrast is does not vary strongly with changes in rotation rate: it is $\sim$50 K over the range of simulations, with variations of about $\pm$20 K depending on the rotation rate. The variations suggest that quantitative estimates of surface temperature differences must account for circulation changes.

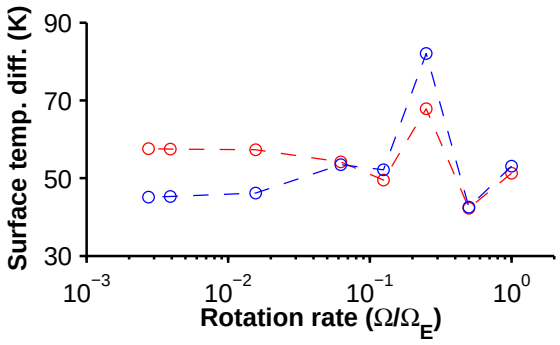

Figure B.15. Surface temperature contrast between the day side and the night side vs. rotation rate. Averages are taken over 10° of longitude centered at the substellar and antistellar points and between −30° and 30° of latitude (red) and between 30° and 60° of latitude (blue).

B.7 Conclusions

We have examined the dynamics of tidally locked, Earth-like planets. The dynamical regime of the atmosphere depends on the planet rotation rate, as anticipated from scaling arguments. The simulations demonstrate the importance of the atmospheric circulation in determining the surface climate. For example, the difference between the precipitation distributions in the slowly and rapidly rotating simulations clearly shows the dependence of the hydrological cycle on the circulation of the atmosphere. Interestingly, some aspects of the simulated climate are not sensitive to the planet's rotation rate. In particular, the temperature contrast between the day and night side

and evaporation rates are similar between the slowly and rapidly rotating simulations.

The general circulation of the slowly rotating atmosphere features global-scale, thermodynamically-direct, divergent circulations with ascending motion at the sub-solar point and descending motion elsewhere. In contrast, the general circulation of the rapidly rotating atmosphere features extratropical jets that owe their existence to rotational (Rossby) waves, and tropical surface winds that are the result of stationary equatorial (Rossby and Kelvin) waves. The isotropy of the winds in the slowly rotating regime and the anisotropy of the winds in the rapidly rotating regime are expected from the dominant balance of the horizontal momentum equations. Expectations for the free-atmospheric pressure and temperature gradients based on scale analysis were realized in the simulations of the different circulations regimes: temperature gradients are weak where Coriolis accelerations are weak (in low latitudes of the rapidly rotating atmosphere and globally in the slowly rotating atmosphere) and larger where Coriolis accelerations are dynamically important (in the extratropics of the rapidly rotating atmosphere).

The series of simulations with varying rotation rates demonstrates that the degree of equatorial superrotation varies non-monotonically. A full explanation for the dependence of equatorial superrotation on the rotation rate remains an open question. In contrast, the surface temperature contrast between the day side and the night side is approximately 50 K over the range of rotation rates.

While many aspects of the simulations can be explained by general circulation theories for Earth and Earth-like atmospheres, there remain quantitative questions that require more systematic experimentation than we have attempted here. For example, the dependence of the surface climate on the solar constant may be different from simulations with Earth-like insolation because of the differences in stratification.

B.8 Acknowledgments

Timothy Merlis was supported by a National Defense Science and Engineering Graduate fellowship and a National Science Foundation Graduate Research fellowship. We

thank Dorian Abbot and Sonja Graves for providing modifications to the GCM code and Simona Bordoni, Ian Eisenman, Andy Ingersoll, Yohai Kaspi, and two anonymous reviewers for comments on the manuscript. The simulations were performed on Caltech's Division of Geological and Planetary Sciences Dell cluster. The program code for the simulations, based on the Flexible Modeling System of the Geophysical Fluid Dynamics Laboratory, and the simulation results themselves are available from the authors upon request.

B.9 Appendix: Gill model forced by precipitation

We use the formulation for a Gill model forced by precipitation (Neelin 1988), as opposed to the standard mass sink. The model equations are

$$-f\tilde{v} = -\partial_x\tilde{\phi} - \epsilon_m\tilde{u}; \tag{B.9}$$

$$f\tilde{u} = -\partial_y\tilde{\phi} - \epsilon_m\tilde{v}; \tag{B.10}$$

$$c^2(\partial_x\tilde{u} + \partial_y\tilde{v}) = -aP - \epsilon_T\tilde{\phi}, \tag{B.11}$$

where $a = LR/c_p$ is the combination of the latent heat of vaporization, gas constant, and heat capacity at constant pressure that results from converting the precipitation rate to a temperature tendency in the thermodynamic equation and approximating Newtonian cooling by geopotential damping, ϵ_m is the Rayleigh drag coefficient of the momentum equations, ϵ_T is the damping coefficient for the geopotential, other variables have their standard meanings (e.g., P is precipitation), and $\tilde{(\cdot)} = \int_{p_b}^{p_s} (\cdot)\, dp/g$ is the mass-weighted vertical integral over the boundary layer (p_b is the pressure at the top of the boundary layer). We use fairly standard values for the constants (Table B.1). The qualitative aspects of the solutions that we discuss are not sensitive to these choices.

Constant	Value
c	50 m s^{-1}
β	2.22 $\times 10^{-11}$ m^{-1} s^{-1}
ϵ_m	$(1 \text{ day})^{-1}$
ϵ_T	$(20 \text{ day})^{-1}$
a	7.14 $\times 10^5$ J kg^{-1}

Table B.1: Gill model constants and their values.

The three equations can be combined into a single equation for $\tilde{v}$:

$$[-\epsilon_T(\epsilon_m^2 + \beta^2 y^2)/c^2 + \epsilon_m(\partial_{xx} + \partial_{yy}) + \beta\ \partial_x]\tilde{v} = -(\epsilon_m \partial_y - \beta y\ \partial_x)\ aP/c^2, \tag{B.12}$$

where β-plane geometry ($f = \beta y$) has been assumed. The boundary value problem for $\tilde{v}$ is discretized by Fourier transforming in the x-direction and finite differencing in the y-direction. It is solved using the GCM's climatological precipitation field (Fig. B.2) on the right-hand side.

Bibliography

Adler, R. F., et al., 2003: The version-2 Global Precipitation Climatology Project (GPCP) monthly precipitation analysis (1979–present). *J. Hydrometeor.*, **4**, 1147–1167.

Anderson, J. L., V. Balaji, A. J. Broccoli, et al., 2004: The new GFDL global atmosphere and land model AM2-LM2: Evaluation with prescribed SST simulations. *J. Climate*, **17**, 4641–4673.

Arakawa, A. and W. H. Schubert, 1974: Interaction of a cumulus cloud ensemble with the large-scale environment. Part I. *J. Atmos. Sci.*, **31**, 674–701.

Back, L. E. and C. S. Bretherton, 2006: Geographic variability in the export of moist static energy and vertical motion profiles in the tropical Pacific. *Geophys. Res. Lett.*, **33**, L17 810.

Back, L. E. and C. S. Bretherton, 2009: On the relationship between SST gradients, boundary layer winds, and convergence over the tropical oceans. *J. Climate*, **22**, 4182–4196.

Berger, A. L., 1978: Long-term variations of daily insolation and Quaternary climatic changes. *J. Atmos. Sci.*, **35**, 2362–2367.

Betts, A. K., 1986: A new convective adjustment scheme. Part I: Observational and theoretical basis. *Quart. J. Roy. Meteor. Soc.*, **112**, 677–691.

Betts, A. K., 1998: Climate-convection feedbacks: Some further issues. *Climatic Change*, **39**, 35–38.

Betts, A. K. and M. J. Miller, 1986: A new convective adjustment scheme. Part II: Single column tests using GATE wave, BOMEX, ATEX and arctic air-mass data sets. *Quart. J. Roy. Meteor. Soc.*, **112**, 693–709.

Betts, A. K. and W. L. Ridgway, 1989: Climatic equilibrium of the atmospheric convective boundary layer over a tropical ocean. *J. Atmos. Sci.*, **46**, 2621–2641.

Bordoni, S., 2007: On the role of eddies in monsoonal circulations: Observations and theory. Ph.D. thesis, University of California, 195 pp., Los Angeles, CA.

Bordoni, S. and T. Schneider, 2008: Monsoons as eddy-mediated regime transitions of the tropical overturning circulation. *Nature Geosci.*, **1**, 515–519.

Charbonneau, D., T. M. Brown, D. W. Latham, and M. Mayor, 2000: Detection of planetary transits across a Sun-like star. *Astrophys. J.*, **529**, L45–L48.

Charbonneau, D., et al., 2009: A super-Earth transiting a nearby low-mass star. *Nature*, **462**, 891–894.

Charney, J. G., 1963: A note on large-scale motions in the Tropics. *J. Atmos. Sci.*, **20**, 607–609.

Chou, C., J. D. Neelin, and H. Su, 2001: Ocean-atmosphere-land feedbacks in an idealized monsoon. *Quart. J. Roy. Meteor. Soc.*, **127**, 1869–1892.

Clement, A. C., A. Hall, and A. J. Broccoli, 2004: The importance of precessional signals in the tropical climate. *Clim. Dyn.*, **22**, 327–341.

Clement, A. C., R. Seager, M. A. Cane, and S. E. Zebiak, 1996: An ocean dynamical thermostat. *J. Climate*, **9**, 2190–2196.

Couhert, A., T. Schneider, J. Li, D. E. Waliser, and A. M. Tompkins, 2010: The maintenance of the relative humidity of the subtropical free troposphere. *J. Climate*, **23**, 390–403.

Cutler, K. B., et al., 2003: Rapid sea-level fall and deep-ocean temperature change since the last interglacial period. *Earth Planet. Sci. Lett.*, **206**, 253–271.

Dayem, K., D. S. Battisti, G. H. Roe, and P. Molnar, 2010: Lessons learned from the modern monsoon applied to the interpretation of paleoclimate records. *Earth Planet. Sci. Lett.*, **295**, 219–230.

deMenocal, P., J. Ortiz, T. Guilderson, J. Adkins, M. Sarnthein, L. Baker, and M. Yarusinsky, 2000: Abrupt onset and termination of the African Humid Period: rapid climate responses to gradual insolation forcing. *Quat. Sci. Rev.*, **19**, 347–361.

DiNezio, P. N., A. C. Clement, G. A. Vecchi, B. J. Soden, B. P. Kirtman, and S. K. Lee, 2009: Climate response of the equatorial Pacific to global warming. *J. Climate*, **22**, 4873–4892.

Dirmeyer, P. A., 1998: Land-sea geometry and its effect on monsoon circulations. *J. Geophys. Res.*, **103**, 11 555–11 572.

Edmon, H. J., B. J. Hoskins, and M. E. McIntyre, 1980: Eliassen-Palm cross sections for the troposphere. *J. Atmos. Sci.*, **37**, 2600–2616.

Emanuel, K., 2007: Quasi-equilibrium dynamics of the tropical atmosphere. *The Global Circulation of the Atmosphere*, T. Schneider and A. H. Sobel, Eds., Princeton University Press, Princeton, NJ, 186–218.

Emanuel, K. A., 1994: *Atmospheric Convection*. Oxford University Press, New York, 580 pp.

Fedorov, A. V., P. S. Dekens, M. McCarthy, A. C. Ravelo, P. B. DeMenocal, M. Barreiro, R. C. Pacanowski, and S. G. Philander, 2006: The Pliocene paradox (mechanisms for a permanent El Niño). *Science*, **312**, 1485–1489.

Frierson, D. M. W., 2007: The dynamics of idealized convection schemes and their effect on the zonally averaged tropical circulation. *J. Atmos. Sci.*, **64**, 1959–1976.

Frierson, D. M. W., I. M. Held, and P. Zurita-Gotor, 2006: A gray-radiation aquaplanet moist GCM. Part I: Static stability and eddy scale. *J. Atmos. Sci.*, **63**, 2548–2566.

Gall, R., 1976a: A comparison of linear baroclinic instability theory with the eddy statistics of a general circulation model. **33**, 349–373.

Gall, R., 1976b: Structural changes of growing baroclinic waves. **33**, 374–390.

Gill, A. E., 1980: Some simple solutions for heat-induced tropical circulation. *Quart. J. Roy. Meteor. Soc.*, **106**, 447–462.

Hall, N. and P. Sardeshmukh, 1998: Is the time-mean northern hemisphere flow baroclinically unstable? **55**, 41–56.

Hartmann, D., 1994: *Global Physical Climatology*. Academic Press, 411 pp.

Hartmann, D. L. and K. Larson, 2002: An important constraint on tropical cloud-climate feedback. *Geophys. Res. Lett.*, **29**, 1951, doi:10.1029/2002GL015835.

Held, I. M., 1978: The vertical scale of an unstable baroclinic wave and its importance for eddy heat flux parameterizations. *J. Atmos. Sci.*, **35**, 572–576.

Held, I. M., 1982: Climate models and the astronomical theory of the ice ages. *Icarus*, **50**, 449–461.

Held, I. M., 1999: The macroturbulence of the troposphere. *Tellus*, **51A-B**, 59–70.

Held, I. M., 2000: The general circulation of the atmosphere. *Proc. Program in Geophysical Fluid Dynamics*, Woods Hole, MA, Woods Hole Oceanographic Institution, URL `https://darchive.mblwhoilibrary.org/handle/1912/15`.

Held, I. M., 2001: The partitioning of the poleward energy transport between the tropical ocean and atmosphere. *J. Atmos. Sci.*, **58**, 943–948.

Held, I. M. and B. J. Hoskins, 1985: Large-scale eddies and the general circulation of the troposphere. *Advances in Geophysics*, S. Manabe, Ed., Academic Press, Vol. 28A, 3–31.

Held, I. M. and A. Y. Hou, 1980: Nonlinear axially symmetric circulations in a nearly inviscid atmosphere. *J. Atmos. Sci.*, **37**, 515–533.

Held, I. M. and V. D. Larichev, 1996: A scaling theory for horizontally homogeneous, baroclinically unstable flow on a beta-plane. *J. Atmos. Sci.*, **53**, 946–952.

Held, I. M. and B. J. Soden, 2006: Robust responses of the hydrological cycle to global warming. *J. Climate*, **19**, 5686–5699.

Held, I. M. and M. J. Suarez, 1994: A proposal for the intercomparison of the dynamical cores of atmospheric general circulation models. *Bull. Amer. Meteor. Soc.*, **75**, 1825–1830.

Held, I. M., M. Winton, K. Takahashi, T. Delworth, F. Zeng, and G. K. Vallis, 2010: Probing the fast and slow components of global warming by returning abruptly to preindustrial forcing. *J. Climate*, **23**, 2418–2427.

Herweijer, C., R. Seager, M. Winton, and A. Clement, 2005: Why ocean heat transport warms the global mean climate. *Tellus*, **57A**, 662–675.

Hide, R., 1969: Dynamics of the atmospheres of the major planets with an appendix on the viscous boundary layer at the rigid bounding surface of an electrically-conducting rotating fluid in the presence of a magnetic field. *J. Atmos. Sci.*, **26**, 841–853.

Hubbard, W. B., 1984: *Planetary Interiors*. Van Nostrand Reinhold Co., 334 pp.

Huybers, P., 2006: Early Pleistocene glacial cycles and the integrated summer insolation forcing. *Science*, **313**, 508–511.

Huybers, P. and P. Molnar, 2007: Tropical cooling and the onset of North American glaciation. *Clim. Past*, **3**, 549–557.

Iribarne, J. V. and W. L. Godson, 1981: *Atmospheric Thermodynamics*. 2nd ed., Geophysics and Astrophysics Monographs, D. Reidel, Dordrecht, Holland, 259 pp.

Jackson, C. S. and A. J. Broccoli, 2003: Orbital forcing of Arctic climate: mechanisms of climate response and implications for continental glaciation. *Clim. Dyn.*, **21**, 539–557.

Joshi, M., 2003: Climate model studies of synchronously rotating planets. *Astrobiology*, **3**, 415–427.

Joshi, M. M., R. M. Haberle, and R. T. Reynolds, 1997: Simulations of the atmospheres of synchronously rotating terrestrial planets orbiting M Dwarfs: Conditions for atmospheric collapse and the implications for habitability. *Icarus*, **129**, 450–465.

Kållberg, P., A. Simmons, S. Uppala, and M. Fuentes, 2004: The ERA-40 archive. Tech. rep., European Centre for Medium-Range Weather Forecasts, 31 pp., Reading, United Kingdom. URL `www.ecmwf.int/publications`.

Kang, S. M., D. M. W. Frierson, and I. M. Held, 2009: The tropical response to extratropical thermal forcing in an idealized GCM: The importance of radiative feedbacks and convective parameterization. *J. Atmos. Sci.*, **66**, 2812–2827.

Kang, S. M. and I. M. Held, 2011: Tropical precipitation, SSTs and the surface energy budget: a zonally symmetric perspective. *Clim. Dyn.*, 1–8, doi:10.1007/s00382-011-1048-7.

Kang, S. M., I. M. Held, D. M. W. Frierson, and M. Zhao, 2008: The response of the ITCZ to extratropical thermal forcing: Idealized slab-ocean experiments with a GCM. *J. Climate*, **21**, 3521–3532.

Khon, V. C., W. Park, M. Latif, I. I. Mokhov, and B. Schneider, 2010: Response of the hydrological cycle to orbital and greenhouse gas forcing. *Geophys. Res. Lett.*, **37**, L19 705, doi:10.1029/2010GL044377.

Klinger, B. A. and J. Marotzke, 2000: Meridional heat transport by the subtropical cell. *J. Phys. Oceanogr.*, **30**, 696–705.

Knutson, T. R. and S. Manabe, 1995: Time-mean response over the tropical Pacific to increased CO_2 in a coupled ocean-atmosphere model. *J. Climate*, **8**, 2181–2199.

Kutzbach, J., 1981: Monsoon climate of the early Holocene: climate experiment with the earth's orbital parameters for 9000 years ago. *Science*, **214**, 59–61.

Kutzbach, J. E., 1985: Milankovitch forcing of fluctuations in the level of tropical lakes from 18 to 0 kyr BP. *Nature*, **317**, 130–134.

Legrande, A. N. and G. A. Schmidt, 2009: Sources of Holocene variability of oxygen isotopes in paleoclimate archives. *Clim. Past*, **5**, 441–455.

Levine, X. J. and T. Schneider, 2011: Response of the Hadley circulation to climate change in an aquaplanet GCM coupled to a simple representation of ocean heat transport. *J. Atmos. Sci.*, **68**, 769–783.

Li, J.-L. F., et al., 2008: Comparisons of satellites liquid water estimates to ECMWF and GMAO analyses, 20th century IPCC AR4 climate simulations, and GCM simulations. *Geophys. Res. Lett.*, **35**, L19 710.

Lindzen, R. S. and B. Farrell, 1980: A simple approximate result for the maximum growth rate of baroclinic instabilities. *J. Atmos. Sci.*, **37**, 1648–1654.

Lindzen, R. S. and A. Y. Hou, 1988: Hadley circulations for zonally averaged heating centered off the equator. *J. Atmos. Sci.*, **45**, 2416–2427.

Lindzen, R. S. and S. Nigam, 1987: On the role of sea surface temperature gradients in forcing low-level winds and convergence in the Tropics. *J. Atmos. Sci.*, **44**, 2418–2436.

Lindzen, R. S. and W. Pan, 1994: A note on orbital control of equator-pole heat fluxes. *Clim. Dyn.*, **10**, 49–57.

Lintner, B. R. and J. C. H. Chiang, 2005: Reorganization of tropical climate during El Niño: A weak temperature gradient approach. *J. Climate*, **18**, 5312–5329.

Lorenz, E. N., 1955: Available potential energy and the maintenance of the general circulation. *Tellus*, **7**, 157–167.

Meehl, G. A., et al., 2007: Global climate projections. *Climate Change 2007: The Physical Science Basis. Contribution of Working Group I to the Fourth Assessment Report of the Intergovernmental Panel on Climate Change*, S. Solomon, D. Qin, M. Manning, Z. Chen, M. Marquis, K. Averyt, M. Tignor, and H. Miller, Eds., Cambridge Univ. Press, Cambridge, UK, and New York, NY, USA, 747–845.

Merlis, T. M. and T. Schneider, 2009: Scales of linear baroclinic instability and macroturbulence in dry atmospheres. *J. Atmos. Sci.*, **66**, 1821–1833.

Merlis, T. M. and T. Schneider, 2010: Atmospheric dynamics of Earth-like tidally locked aquaplanets. *J. Adv. Earth Model. Syst.*, **2**, Art. #13, 17 pp.

Merlis, T. M. and T. Schneider, 2011: Changes in zonal surface temperature gradients and Walker circulations in a wide range of climates. *J. Climate*, in press.

Neelin, J. D., 1988: A simple model for surface stress and low-level flow in the tropical atmosphere driven by prescribed heating. *Quart. J. Roy. Meteor. Soc.*, **114**, 747–770.

Neelin, J. D., 1989: On the intepretation of the Gill model. *J. Atmos. Sci.*, **46**, 2466–2468.

Neelin, J. D., 1997: Implications of convective quasi-equilibrium for the large-scale flow. *The Physics and Parameterization of Moist Atmospheric Convection*, R. K. Smith, Ed., Kluwer Academic Publishers, Netherlands, 413–446.

Neelin, J. D., 2007: Moist dynamics of tropical convection zones in monsoons, teleconnections, and global warming. *The Global Circulation of the Atmosphere*, T. Schnei-

der and A. H. Sobel, Eds., Princeton University Press, Princeton, NJ, chap. 10, 267–301.

Neelin, J. D. and N. Zeng, 2000: A quasi-equilibrium tropical circulation model—formulation. *J. Atmos. Sci.*, **57**, 1741–1766.

Nie, J., W. R. Boos, and Z. Kuang, 2010: Observational evaluation of a convective quasi-equilibrium view of monsoons. *J. Climate*, **23**, 4416–4428.

O'Gorman, P. A. and C. J. Muller, 2010: How closely do changes in surface and column water vapor follow Clausius–Clapeyron scaling in climate change simulations? *Environ. Res. Lett.*, **5**, 025 207.

O'Gorman, P. A. and T. Schneider, 2007: Recovery of atmospheric flow statistics in a general circulation model without nonlinear eddy–eddy interactions. *Geophys. Res. Lett.*, **34**, L22 801.

O'Gorman, P. A. and T. Schneider, 2008a: Energy of midlatitude transient eddies in idealized simulations of changed climates. *J. Climate*, **21**, 5797–5806.

O'Gorman, P. A. and T. Schneider, 2008b: The hydrological cycle over a wide range of climates simulated with an idealized GCM. *J. Climate*, **21**, 3815–3832.

O'Gorman, P. A. and T. Schneider, 2008c: Weather-layer dynamics of baroclinic eddies and multiple jets in an idealized general circulation model. *J. Atmos. Sci.*, **65**, 524–535.

Pausata, F. S. R., D. S. Battisti, K. H. Nisancioglu, and C. M. Bitz, 2011: Chinese stalagmite δ^{18} O controlled by changes in the Indian monsoon during a simulated Heinrich event. *Nature Geosci.*, **4**, 474–480.

Peixoto, J. P. and A. H. Oort, 1992: *Physics of Climate*. American Institute of Physics, 555 pp.

Peters, M. E. and C. S. Bretherton, 2005: A simplified model of the Walker circulation with an interactive ocean mixed layer and cloud-radiative feedbacks. *J. Climate*, **18**, 4216–4234.

Peters, M. E., Z. Kuang, and C. C. Walker, 2008: Analysis of atmospheric energy transport in ERA-40 and implications for simple models of the mean tropical circulation. *J. Climate*, **21**, 5229–5241.

Pierrehumbert, R. T., 2002: The hydrologic cycle in deep-time climate problems. *Nature*, **419**, 191–198.

Pierrehumbert, R. T., 2010: *Principles of Planetary Climate*. Cambridge University Press, 688 pp.

Plumb, R. A. and A. Y. Hou, 1992: The response of a zonally symmetric atmosphere to subtropical thermal forcing: Threshold behavior. *J. Atmos. Sci.*, **49**, 1790–1799.

Privé, N. C. and R. A. Plumb, 2007a: Monsoon dynamics with interactive forcing. Part I: Axisymmetric studies. *J. Atmos. Sci.*, **64**, 1417–1430.

Privé, N. C. and R. A. Plumb, 2007b: Monsoon dynamics with interactive forcing. Part II: Impact of eddies and asymmetric geometries. *J. Atmos. Sci.*, **64**, 1431–1442.

Raymo, M. E. and K. Nisancioglu, 2003: The 41 kyr world: Milankovitch's other unsolved mystery. *Paleoceanography*, **18**, doi:10.1029/2002PA000791.

Rhines, P. B., 1994: Jets. *Chaos*, **4**, 313–339.

Rodwell, M. J. and B. J. Hoskins, 1996: Monsoons and the dynamics of deserts. *Quart. J. Roy. Meteor. Soc.*, **122**, 1385–1404.

Ruddiman, W. F., 2008: *Earth's Climate: Past and Future*. 2nd ed., W. H. Freeman and Company, 388 pp.

Rupper, S. and G. Roe, 2008: Glacier changes and regional climate: A mass and energy balance approach. *J. Climate*, **21**, 5384–5401.

Saravanan, R., 1993: Equatorial superrotation and maintenance of the general circulation in two-level models. *J. Atmos. Sci.*, **50 (9)**, 1211–1227.

Sardeshmukh, P. D. and B. J. Hoskins, 1988: The generation of global rotational flow by steady idealized tropical divergence. *J. Atmos. Sci.*, **45**, 1228–1251.

Schmidt, G. A., D. T. Shindell, and S. Harder, 2004: A note on the relationship between ice core methane concentrations and insolation. *Geophys. Res. Lett.*, **31**, L23 206.

Schneider, E. K., 1977: Axially symmetric steady-state models of the basic state for instability and climate studies. Part II. Nonlinear calculations. *J. Atmos. Sci.*, **34**, 280–296.

Schneider, E. K., 1981: On the amplitudes reached by baroclinically unstable disturbances. *J. Atmos. Sci.*, **38**, 2142–2149.

Schneider, T., 2004: The tropopause and the thermal stratification in the extratropics of a dry atmosphere. *J. Atmos. Sci.*, **61**, 1317–1340.

Schneider, T., 2006: The general circulation of the atmosphere. *Ann. Rev. Earth Planet. Sci.*, **34**, 655–688.

Schneider, T. and S. Bordoni, 2008: Eddy-mediated regime transitions in the seasonal cycle of a Hadley circulation and implications for monsoon dynamics. *J. Atmos. Sci.*, **65**, 915–934.

Schneider, T. and J. J. Liu, 2009: Formation of jets and equatorial superrotation on Jupiter. *J. Atmos. Sci.*, **66**, 579–601.

Schneider, T. and P. A. O'Gorman, 2008: Moist convection and the thermal stratification of the extratropical troposphere. *J. Atmos. Sci.*, **65**, 3571–3583.

Schneider, T., P. A. O'Gorman, and X. J. Levine, 2010: Water vapor and the dynamics of climate changes. *Rev. Geophys.*, **48**, RG3001, doi:10.1029/2009RG000302.

Schneider, T. and C. C. Walker, 2006: Self-organization of atmospheric macroturbulence into critical states of weak nonlinear eddy–eddy interactions. *J. Atmos. Sci.*, **63**, 1569–1586.

Schneider, T. and C. C. Walker, 2008: Scaling laws and regime transitions of macroturbulence in dry atmospheres. *J. Atmos. Sci.*, **65**, 2153–2173.

Shepherd, T. G., 1987a: Rossby waves and two-dimensional turbulence in a large-scale zonal jet. *J. Fluid Mech.*, **183**, 467–509.

Shepherd, T. G., 1987b: A spectral view of nonlinear fluxes and stationary-transient interaction in the atmosphere. *J. Atmos. Sci.*, **44**, 1166–1178.

Showman, A. P., J. Y.-K. Cho, and K. Menou, 2010: Atmospheric circulation of extrasolar planets. *Exoplanets*, S. Seager, Ed., University of Arizona Press, Tucson, AZ.

Simmons, A. J. and B. J. Hoskins, 1976: Baroclinic instability on the sphere: Normal modes of the primitive and quasigeostrophic equations. *J. Atmos. Sci.*, **33**, 1454–1477.

Simmons, A. J. and B. J. Hoskins, 1978: The life cycles of some nonlinear baroclinic waves. *J. Atmos. Sci.*, **35**, 414–432.

Smagorinsky, J., S. Manabe, and J. L. Holloway, Jr., 1965: Numerical results from a nine-level general circulation model of the atmosphere. *Mon. Wea. Rev.*, **93**, 727–768.

Smith, K., 2007: The geography of linear baroclinic instability in earths oceans. *Journal of Marine Research*, **65**, 655–683.

Smith, K. S., G. Boccaletti, C. C. Henning, I. N. Marinov, C. Y. Tam, I. M. Held, and G. K. Vallis, 2002: Turbulent diffusion in the geostrophic inverse energy cascade. *J. Fluid Mech.*, **469**, 13–48.

Sobel, A. H., 2002: Water vapor as an active scalar in tropical atmospheric dynamics. *Chaos*, **12**, 451–459.

Sobel, A. H., 2003: On the coexistence of an evaporation minimum and precipitation maximum in the warm pool. *J. Climate*, **16**, 1003–1009.

Sobel, A. H., 2007: Simple models of ensemble-averaged tropical precipitation and surface wind, given the sea surface temperature. *The Global Circulation of the Atmosphere*, T. Schneider and A. H. Sobel, Eds., Princeton University Press, Princeton, NJ, chap. 8, 219–251.

Sobel, A. H., I. M. Held, and C. S. Bretherton, 2002: The ENSO signal in tropical tropospheric temperature. *J. Climate*, **15**, 2702–2706.

Sobel, A. H., E. D. Maloney, G. Bellon, and D. M. Frierson, 2010: Surface fluxes and tropical intraseasonal variability: a reassessment. *J. Adv. Earth Model. Syst.*, **2**, Art. #2, 27 pp.

Sobel, A. H. and J. D. Neelin, 2006: The boundary layer contribution to intertropical convergence zones in the quasi-equilibrium tropical circulation model framework. *Theor. Comput. Fluid Dyn.*, **20**, 323–350.

Sobel, A. H., J. Nilsson, and L. M. Polvani, 2001: The weak temperature gradient approximation and balanced tropical moisture waves. *J. Atmos. Sci.*, **58**, 3650–3665.

Stevens, B., J. Duan, J. C. McWilliams, M. Münnich, and J. D. Neelin, 2002: Entrainment, Rayleigh friction, and boundary layer winds over the tropical Pacific. *J. Climate*, **15**, 30–44.

Suarez, M. J. and D. G. Duffy, 1992: Terrestrial superrotation: A bifurcation of the general circulation. *J. Atmos. Sci.*, **49**, 1541–1554.

Thorncroft, C. D. and B. J. Hoskins, 1994: An idealized study of African easterly waves. I: A linear view. *Quart. J. Roy. Meteor. Soc.*, **120**, 953–982.

Thuburn, J. and G. C. Craig, 2000: Stratospheric influence on tropopause height: The radiative constraint. *J. Atmos. Sci.*, **57**, 17–28.

Trenberth, K. E., J. M. Caron, and D. P. Stepaniak, 2001: The atmospheric energy budget and implications for surface fluxes and ocean heat transports. *Clim. Dyn.*, **17**, 259–276.

Trenberth, K. E., J. T. Fasullo, and J. Kiehl, 2009: Earth's global energy budget. *Bull. Amer. Meteor. Soc.*, **90**, 311–323.

Valdes, P. J. and B. J. Hoskins, 1988: Baroclinic instability of the zonally averaged flow with boundary layer damping. *J. Atmos. Sci.*, **45**, 1584–1593.

Vallis, G. K., 2006: *Atmospheric and Oceanic Fluid Dynamics: Fundamentals and Large-Scale Circulation*. Cambridge University Press, Cambridge, UK, 771 pp.

Vecchi, G. A., A. Clement, and B. J. Soden, 2008: Examining the tropical Pacific's response to global warming. *Eos Trans. AGU*, **89**, 81–83.

Vecchi, G. A. and B. J. Soden, 2007: Global warming and the weakening of the tropical circulation. *J. Climate*, **20**, 4316–4340.

Vecchi, G. A., B. J. Soden, A. T. Wittenberg, I. M. Held, A. Leetmaa, and M. J. Harrison, 2006: Weakening of tropical Pacific atmospheric circulation due to anthropogenic forcing. *Nature*, **441**, 73–76.

Walker, C. C. and T. Schneider, 2005: Response of idealized Hadley circulations to seasonally varying heating. *Geophys. Res. Lett.*, **32**, L06 813, doi:10.1029/2004GL022304.

Walker, C. C. and T. Schneider, 2006: Eddy influences on Hadley circulations: Simulations with an idealized GCM. *J. Atmos. Sci.*, **63**, 3333–3350.

Wang, X., A. S. Auler, R. L. Edwards, H. Cheng, E. Ito, and M. Solheid, 2006: Interhemispheric anti-phasing of rainfall during the last glacial period. *Quat. Sci. Rev.*, **25**, 3391–3403.

Wang, X., A. S. Auler, R. L. Edwards, H. Cheng, E. Ito, Y. Wang, X. Kong, and M. Solheid, 2007: Millennial-scale precipitation changes in southern Brazil over the past 90,000 years. *Geophys. Res. Lett.*, **34**, L23 701.

Wang, Y., H. Cheng, R. L. Edwards, et al., 2008: Millennial-and orbital-scale changes in the East Asian monsoon over the past 224,000 years. *Nature*, **451**, 1090–1093.

Webster, P. J. and J. Fasullo, 2003: Monsoon: dynamical theory. *Encyclopedia of Atmospheric Sciences*, 1370–1386.

Williams, G. P., 1988: The dynamical range of global circulations — I. *Climate Dyn.*, **2**, 205–260.

Wunsch, C., 2009: A perpetually running ENSO in the Pliocene? *J. Climate*, **22**, 3506–3510.

Xie, S.-P., C. Deser, G. A. Vecchi, J. Ma, H. Teng, and A. T. Wittenberg, 2010: Global warming pattern formation: Sea surface temperature and rainfall. *J. Climate*, **23**, 966–986.

Xu, K.-M. and K. A. Emanuel, 1989: Is the tropical atmosphere conditionally unstable? *Mon. Wea. Rev.*, **117**, 1471–1479.